Contributions to the understanding of the hierarchical structure and dynamics of spider dragline silk

Daniel Sapede

UNIVERSITE JOSEPH FOURIER-GRENOBLE I
U.F.R. DE PHYSIQUE

EUROPEAN SYNCHROTRON RADIATION FACILITY (ESRF)
INSTITUT LAUE-LANGEVIN (ILL)

Doctorat

Discipline : Physique

Présenté et soutenu publiquement par

Daniel SAPEDE

Contributions à la compréhension de la structure et de la dynamique hiérarchiques du fil de traîne de l'araignée

Thèse dirigée par :

Tilo SEYDEL

Christian RIEKEL

soutenue le :

2 février 2006

COMPOSITION DU JURY :

M. BEE	Université Joseph Fourier, Grenoble	Président
J. DOUCET	Université Paris-Sud, Orsay	Rapporteur
M. MÜLLER	Christian-Albrechts-Universität, Kiel	Rapporteur
C. DICKO	University of Oxford	Examinateur
T. SEYDEL	ILL, Grenoble	Directeur de thèse

ACKNOWLEDGMENTS

This work was possible thanks to the help of many people to whom I am extremely grateful. Especially, my supervisors **Christian Riekel** and **Tilo Seydel** both offered a lot of their time and energy to guide me along the experiments, the analysis and the writing steps. As importantly, they showed a productive tolerance during the difficult moments and they were there to help me overcoming these periods. They taught me countless things and I hope they are as proud as I am of the success of the project.

Fritz Vollrath and his team at the Zoology Department of the University of Oxford provided the essential and toughly collected samples. They motivated greatly this project and I am glad we had fruitful discussions.

I greatly appreciated the opportunity to work on a collaborative project involving the ESRF and the ILL. This was rendered possible thanks to the interest and the involvement of **Sine Larsen**, **Helmut Schober** and **Christian Vettier**.

Trevor Forsyth and **Marek Koza** played an important role and were deeply involved in the project, both their intuition and knowledge being extremely profitable for planning experiments and for the data analysis.

Many experiments were conducted during this project and were successful because of the excellent work of local contacts, instrument responsibles, engineers and technicians. Thus I acknowledge all the ID13 ESRF beamline staff (**Manfred Burghammer**, **Richard Davies**, **Lionel Lardière**, **Dmitriy Popov**, ...) and the staff of the instruments that were used at the ILL (**Bernhard Frick**, **Matthias Elender**, **Giovana Fragneto**, **Isabelle Grillo**, **Ralf Schweins**, ...). I enjoyed a lot the experimental work at the ESRF and the ILL thanks to all these people who not only are proficient but also render the ambience pleasant during long experiments.

I appreciated all the people I shared an office with at one time or another, and who made everyday life so convivial: **Sébastien Vial**, **Henrik Lemke**, **Alexander Hermes**, **Anne Martel**. Meetings, discussions and coffee breaks with the ESRF and ILL PhD students were great moments. I also acknowledge **Stephan Roth**, **David Flot** and **Aurelien Gourrier** for their advises and support.

Finally, I am very grateful to Prof. **Jean Doucet** (Université Paris-Sud) and Prof. **Martin Müller** (University of Kiel) for accepting to report on this manuscript and to Prof. **Marc Bée** (Université Joseph Fourier) and Dr. **Cedric Dicko** (University of Oxford) for participating in this Jury and for comments on the thesis.

CONTENT

Abbreviations

A	Alanine (aminoacid)
BS	backscattering
EISF	elastic incoherent structure factor
ESRF	European Synchrotron Radiation Facility
FWHM	full-width at half maximum
FEW	fixed-energy window
G	Glycine (aminoacid)
GPa	GigaPascal
ILL	Institut Max von Laue - Paul Langevin
INS	inelastic neutron scattering
kDa	kilo Dalton
H/D ratio	Hydrogen/Deuterium ratio
KB mirror	Kirkpatrick-Baez mirror (double focusing X-ray mirror system)
MA	Major ampullate
MJ	MegaJoule
QNS	quasielastic neutron scattering
RH	relative humidity
RS *(in french parts)*	rayonnement synchrotron
SANS	small-angle neutron scattering
SAXS	small-angle X-ray scattering
SR	synchrotron radiation
Sp	Spidroin protein (MASp: Major ampullate spidroin)
Sp1/Sp2	Spidroin 1/ Spidroin 2 proteins
TOF	Time-of-flight
WANS	wide-angle neutron scattering
WAXS	wide-angle X-ray scattering

Outline

Une traduction en français de cette introduction et du plan de ce mémoire est donnée à la fin de ce chapitre.

Outline

Spider dragline silk is a fascinating material, a biopolymer with outstanding mechanical properties, often refereed as "stronger than steel". Not only strong, it has also a high extensibility, and its toughness equals that of the best commercial nylon filaments, themselves benchmark of modern polymer fibre technology. In contrast to polymers based on petrochemicals, silks are easily and totally recyclable and biodegradable. The silk production capabilities of the spider also have many advantages: a cheap protein in water solvent being spun at ambient temperature and pressure. It therefore shows great promise for applications, and mass-production of such a material would be of great impact. Spider silk also outperforms the closely related silkworm silk. Mass breeding as for *Bombyx mori* silkworms is, however, not possible for spiders. Artificial spider silk production is therefore a principal goal for biomimetics research. This requires, however, a better understanding of the material as the molecular structure that leads to the functional properties of the silk, and the mechanism by which nature assembles this structure, are far from being understood.

The goal of this thesis is thus to provide additional information concerning the molecular structure and mobility of spider dragline silk using scattering methods. In addition, the important role of adsorbed water shall be further investigated. The microbeam X-ray scattering technique using synchrotron radiation has in recent years considerably contributed to refining of structural models and to an understanding of spider silk. By contrast, complementary neutron scattering experiments has never before been performed on spider silk. This is although the sensitivity of neutrons for light atoms -in particular hydrogen- and the easy access to information on molecular mobility suggested the possibility of obtaining novel information. Fortunately, the Grenoble research campus hosts next to the synchrotron radiation source of the ESRF also the neutron source of the ILL, which gave a major impetus to the current thesis. It is, however, well known that neutron fluxes are by orders of magnitude lower than SR-fluxes and that thus much larger sample quantities are required in neutron scattering. The feasibility of neutron scattering experiments on spider silk could nevertheless be established for the first time in this work providing access to unique information, hitherto

inaccessible. Sufficient quantities of well aligned spider silk samples and adequate sample environments - that have in part been newly developed during this thesis - were essential for successful neutron scattering experiments.

The organisation of this report is the following. The first chapter is a general presentation of spider dragline silk, illustrating the state-of-the-art on the relation structure-function. The scattering techniques are presented in the second chapter, together with the presentation of the materials, instruments and experiments performed during the project. The three next chapters deal with the presentation of results and discussions for the molecular scale (chapter 3), supramolecular scale (chapter 4) and dynamics (chapter 5). The last chapter is devoted to the conclusion and outlook.

Contour

Le fil de traîne d'araignée est un matériau fascinant, un biopolymère aux propriétés mécaniques exceptionnelles, souvent cité comme "plus résistant que l'acier". Il n'est pas uniquement résistant à la traction, mais présente aussi une importante extensibilité, et sa ténacité égale celle des meilleures fibres commerciales de nylon, elles-mêmes références dans le domaine de la technologie des fibres de polymères modernes. Contrairement aux polymères fabriqués à partir de produits pétrochimiques, les soies sont facilement et totalement recyclables et biodégradables. La capacité de production de soie par l'araignée présente par ailleurs de nombreux avantages : une protéine peu onéreuse, dissoute dans de l'eau en guise de solvant et filée dans des conditions de température et de pression ambiantes. Cela augure donc de belles promesses d'applications, et la production de masse d'un tel matériau aurait un impact important. La soie d'araignée surpasse aussi celle, étroitement liée, du ver à soie. Un élevage en masse similaire à celui des vers à soie *Bombyx Mori* n'est néanmoins pas possible pour les araignées. La production de soie d'araignée artificielle est donc un enjeu majeur pour les recherches s'inspirant du vivant. Cela nécessite cependant une meilleure compréhension du matériau, étant donné que la structure moléculaire qui conduit aux propriétés fonctionnelles de la soie, et les mécanismes par lesquelles la nature assemble cette structure, sont loin d'être compris.

Ainsi l'objectif de cette thèse est de fournir des informations supplémentaires sur la structure et la mobilité moléculaire du fil de traîne de l'araignée à l'aide de techniques de diffusion. De

plus, le rôle important de l'eau absorbée par la soie sera étudié plus en détails. La technique de diffusion d'un microfaisceau de rayons X utilisant le rayonnement synchrotron a, au cours des dernières années, considérablement contribué à l'affinement des modèles structuraux et à la compréhension de la soie d'araignée. En revanche, des expériences complémentaires de diffusion des neutrons n'ont jamais été conduites sur la soie d'araignée. Ceci bien que la sensibilité des neutrons pour les éléments légers -en particulier l'hydrogène- et les facilités d'obtention d'informations sur la mobilité moléculaire suggèrent la possibilité d'obtenir des informations originales. Heureusement, le campus de recherche de Grenoble accueille, à proximité de l'installation de rayonnement synchrotron de l'ESRF, la source de neutrons de l'ILL, ce qui a donné une impulsion majeure à la présente thèse. Il est cependant bien connu que les flux de neutrons sont de plusieurs ordres de grandeur inférieurs aux flux SR et qu'ainsi, des quantités bien plus importantes d'échantillon sont nécessaires en diffusion neutronique. La faisabilité d'expériences de diffusion des neutrons put néanmoins être établie pour la première fois au cours de ce projet, permettant d'accéder à des informations uniques autrement inaccessibles. Les quantités suffisantes d'échantillons de soie d'araignée correctement orientés ainsi que les environnements d'échantillon appropriés -qui ont été en partie développés au cours de cette thèse- furent primordiaux pour le succès des expériences de diffusion neutronique.

Ce rapport est organisé de la façon suivante. Le premier chapitre est une présentation générale du fil de traîne de l'araignée, expliquant l'état de l'art sur la relation structure - fonction. Les techniques de diffusion sont présentées dans le second chapitre, accompagnées de la présentation du matériel, des instruments et des expériences accomplies au cours du projet. Les trois chapitres suivants traitent de la présentation des résultats et discussions à l'échelle moléculaire (chapitre 3), à l'échelle supramoléculaire (chapitre 4) et de la dynamique (chapitre 5). Le dernier chapitre est consacré à la conclusion et aux perspectives.

INTRODUCTION

Certaines araignées tisseuses de toiles sont à même de produire jusqu'à sept types de soies, chacune ayant différentes propriétés et applications. Parmi elles, le fil de traîne est utilisé d'une part comme composant structural de la toile, et d'autre part comme une ligne de sécurité que l'araignée traîne toujours derrière elle. Ce fil est particulièrement étudié car il possède des qualités prometteuses en vue d'applications : résistant à la traction, extensible, tenace, mais aussi biodégradable et produit dans des conditions ambiantes de températures et de pression, avec de l'eau pour seul solvant. Ses propriétés mécaniques sont par ailleurs très sensibles au contenu en eau de la soie : hydratée, la soie devient plus viscoélastique et extensible, et lorsqu'elle est détrempée, un phénomène dit de supercontraction a lieu, consistant en une réduction de 40 à 50% de sa taille. A noter que la fonction potentielle de cette propriété n'a pas été à ce jour découverte. Il est question dans cette étude du fil de traîne de la seule araignée "Nephila Edulis", les espèces de néphiles étant relativement faciles à élever en laboratoire.

La microstructure du biopolymère est en partie connue. La soie est constituée de deux protéines, appelées Sp1 et Sp2, de poids moléculaires respectifs de 60 et 54 kDa, dont les séquences ont été déterminées. Les deux séquences présentent des motifs répétés, une région riche en résidus d'alanine succédant à une région riche en résidus de glycine. La soie est un polymère semi-cristallin, dont les cristallites résultent d'un repliement en feuillets bêta. Il est supposé que ces feuillets bêta sont obtenus par le repliement sur eux-mêmes des motifs d'alanine. Il existe différents types de modèles fonctionnels permettant de reproduire par simulation numérique les propriétés mécaniques de la soie. Les modèles dits hiérarchiques permettent en particulier de relier ces propriétés mécaniques à la microstructure de la soie. Leur efficacité dépend d'une bonne compréhension et d'une bonne connaissance des propriétés structurales et dynamiques. L'effet de l'eau à l'échelle des macromolécules ou encore la nature des domaines à l'échelle du nanomètre sont par exemple mal connues. Les techniques de diffusion des neutrons sont en ce sens d'un intérêt particulier. En effet, les neutrons interagissant fortement avec les noyaux d'hydrogène et la diffusion neutronique est sensible aux changements de structure et de dynamiques microscopiques impliqués par le degré d'humidification.

Overview on spiders and silk production

The first spiders probably appeared during the Devonian period, about 400 million years ago[1]. Spiders are presently classified into the main groups *Mesothelae, Mygalomorphae* and *Araneomorphae*[2]. The *Araneomorphae* are referred to as "true spiders" with 32000 species in 2700 genera or 90 families. The Araneida family of orb-weaving spiders has an enormous diversity of about 2600 species. Orb weaving spiders produce up to seven types of silks, covering a wide range of properties and applications[3, 4] (Figure 1).

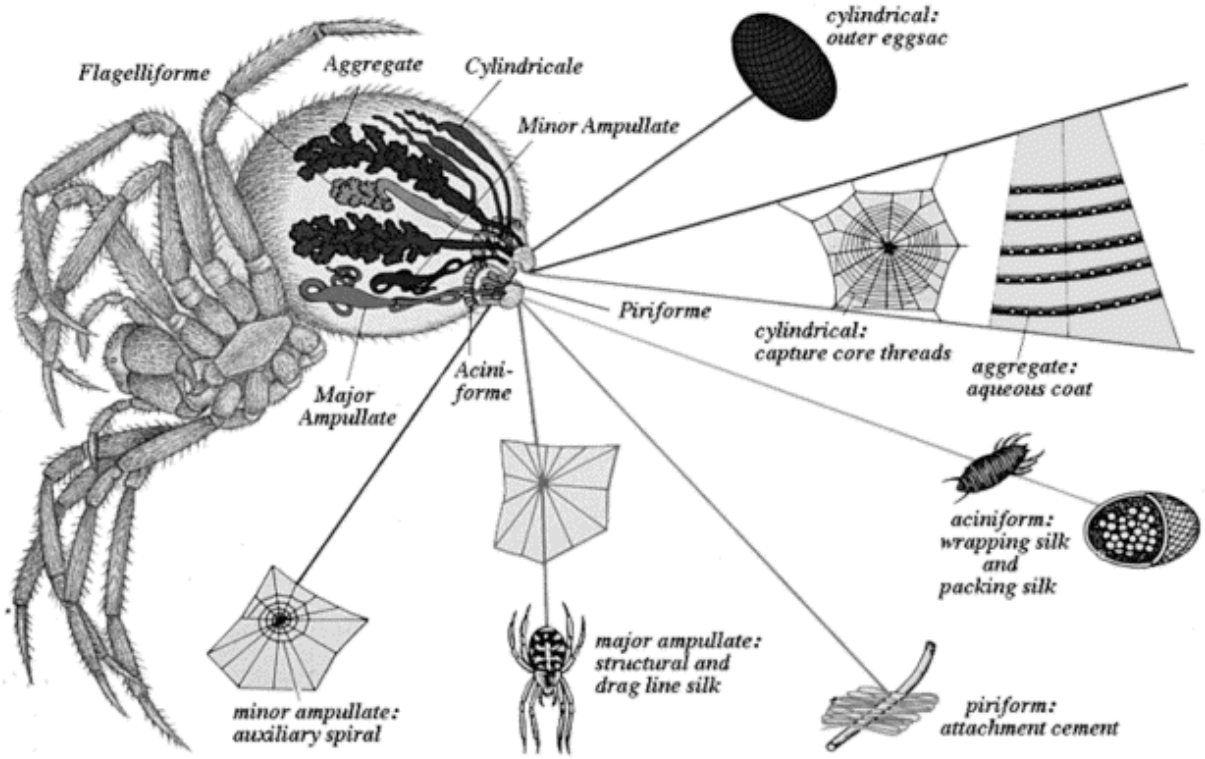

Figure 1 Schematic design of A. diadematus spider showing the system of glands, each secreting a different type of functional silk. [reproduced from Vollrath [4]]

Thus silk produced by the major ampullate gland (Abbr.: MA-silk) is used as a structural silk for the radial threads (a thread corresponds to two single fibres) of the web or as a "dragline" providing a "safety-rope" that the spider can rely on as it falls. The term "dragline" relates to the fact that the spider constantly drags its safety-rope behind. Dragline threads are produced through a pump-and-valve pressure system of the spinning system (Figure 2). The S-shaped glandular ducts thicken the liquid dope secreted from the gland into a highly viscous substance. Fibre formation is assumed to be due to a combination of strong shearing forces in

the tapered duct and a pH-change resulting in an aggregation of the liquid-crystalline polymer[5]. The nascent thread is extruded by the spigot.

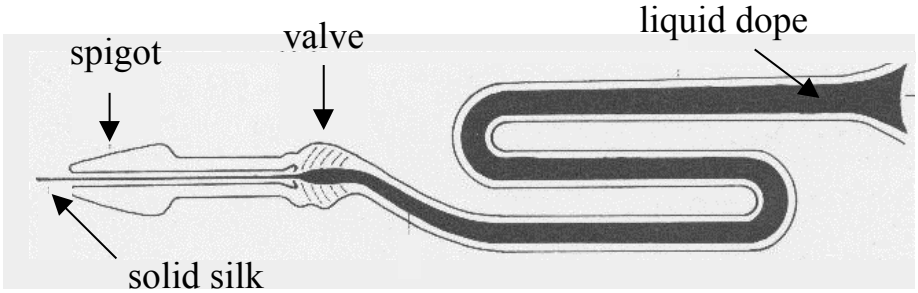

Figure 2 Schematic representation of dragline silk formation. The liquid dope is secreted by the major ampullate glands. *[adapted from Wilson[6]]*.

Figure 3 Picture of female Golden Orb Spider (*Nephila edulis*). (source: http://the-i.org/pic_fauna/01)

Experimental studies on biological silk production have been often performed on spiders from the *Nephila* species (e.g. *Nephila clavipes, Nephila edulis*...), which can be easily bred in the laboratory. Single dragline silk fibres produced by *Nephila* spiders have up to few microns diameter, which is exceptionally big for spiders.

Orb-webs are mainly composed of two kinds of silks: the highly extensible capture thread and the stiffer structural silks[4]. Both have comparable ability to absorb the prey's kinetic energy.

Dragline silk has been particularly well characterised as it shows great promise for technological applications:

- High tensile strength, stronger than steel[7, 8],
- High extensibility as compared to high performance fibres like Kevlar®[7],
- Biodegradability,
- Production at ambient temperature and pressure in an aqueous environment.

There is therefore a considerable interest in understanding the microscopic origin of these properties and to be able to mimic this material.

Mechanical properties[7, 8]

Mechanical properties are key parameters of the spider silk function. Thus dragline silk combines elasticity and strength, resulting into a tough material. Toughness is defined by the area under the stress-strain curve (Figure 4). Thus it depends not only on strength and extensibility but also on the stiffness (slope of the curve). One notes the high extensibility of synthetic rubber, which has, however, a very low strength. (Table 1).

Table 1 comparison of tensile mechanical properties of spider dragline silk with rubber and Kevlar® [from Gosline et al.[8]]

Material	Strength (GPa)	Extensibility (final/initial length)	Toughness (MJ m^{-3})
Nephila dragline	1.15	1.27	160
Synthetic rubber	0.05	8.50	100
Kevlar® 49	3.6	1.027	50

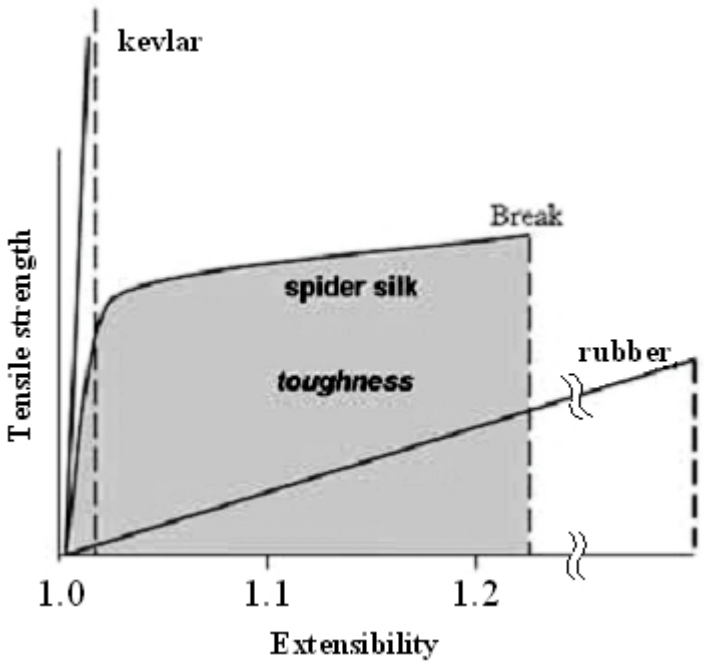

Figure 4 Schematic representation of the stress-strain curves of materials with properties indicated in Table 1.

The influence of water on the mechanical properties is very important as shown in Figure 5. Thus air-dry silk is a moderately high-modulus material. Upon exposure to water, it becomes viscoelastic and highly extensible.

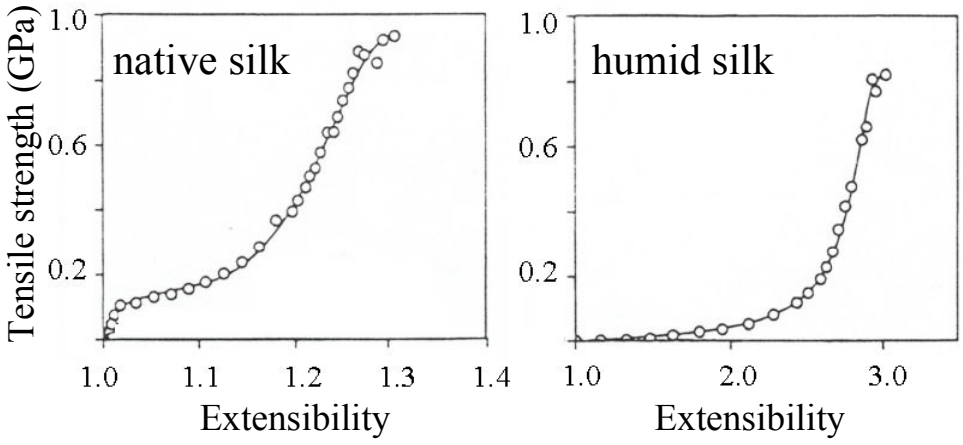

Figure 5 Simulated influence of water on calculated stress versus extensibility curves (o). Note the different extensibility axes for native and humid silk. The curve is drawn to guide the eye (from Termonia [9])

Water degrades therefore the mechanical properties of dragline silk, which are important for the functioning of the web. This implies for example that the nascent fibre should become as soon as possible air-dry in order to reach optimum performance. For this spiders can for example recuperate internally water liberated during the solidification of the silk fibre[10].

Water can also be very easily expelled from a wet fibre by simple squeezing, which could take place under biological conditions by action of the tarsal claws[11]. When immersed in water, dragline silk shrinks by approximately 40-50%. Work[12] called this transition "supercontraction", but to date no one has discovered or described a function for it. Supercontraction will occur in air if relative humidity reaches approximately 90% or more[8].

Structural models

Primary structure

Major ampullate spider silks are composed of several proteins with repetitive sequences. Thus two protein called Spidroin 1 (Sp1) and Spidroin 2 (Sp2) have been determined genetically for *Nephila*[13, 14]. These two proteins have molecular weights of at least 60 kDa for Sp1 and 54 kDa for Sp2. Both proteins contain repeating sequence motifs. Thus for Sp1, a first repeated motif is composed of a polyalanine $(A)_n$ or polyalanylglycine segment $(AG)_n$ of n:6-9 amino acids. This segment is followed by a glycine-rich region made by a $(GGX)_n$ segment, where n is in the range from 5 to 11, X an aminoacid that may vary. In Sp2, a motif containing a $(A)_n$ polyalanine segment is also found, followed by proline and glycine-rich regions. This repetitive nature of amino acid sequences in silk fibres has led to the proposal of "structural modules"[15].

Secondary structure

It is well known that spider dragline silk or silkworm Tussah silk are semicrystalline materials with small crytalline β-poly(L-alanine) domains interspersed in an amorphous matrix[16-22]. Figure 6.A shows schematically the hydrogen-binding scheme of the antiparallel β-sheet structure, which is the favoured model for β-poly(L-alanine). The corresponding diffraction patterns are shown in Figure 6.B (review: [23]). The formation of the crystalline β-poly(L-alanine) domains is thought to occur due to a folding of the protein chain so that the repetitive $(A)_n$ repeats aggregate into crystalline domains.

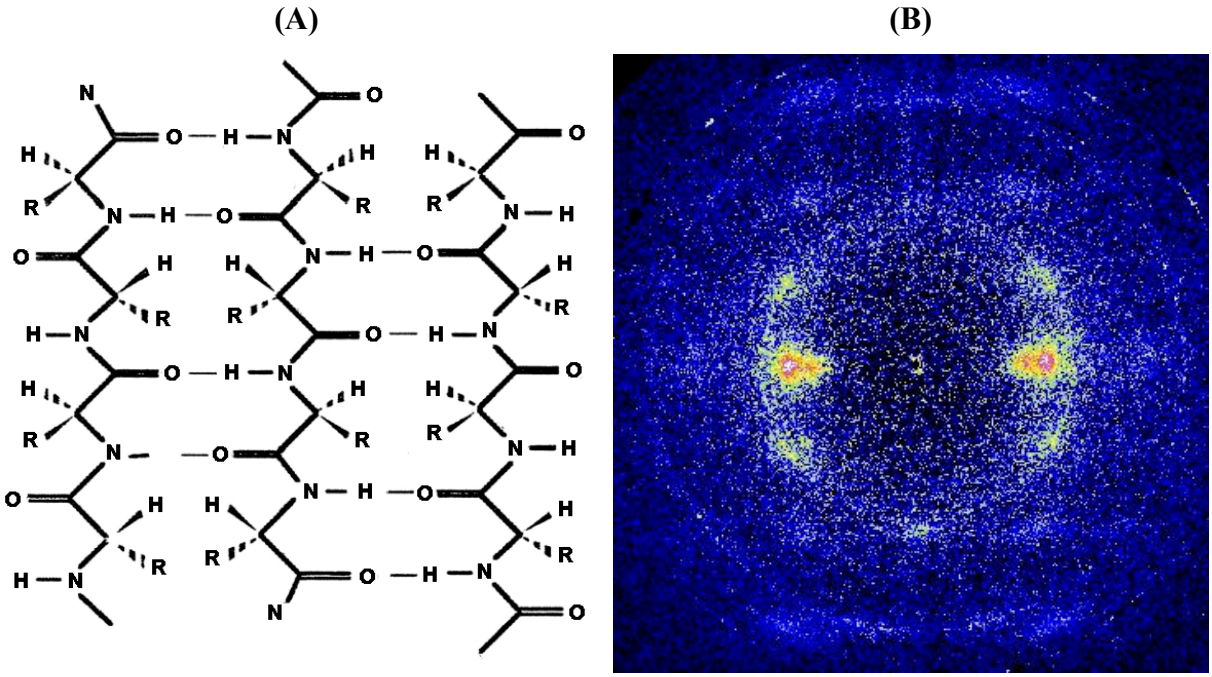

Figure 6 (A) Schematic picture of antiparallel β-sheet structure. R = CH_3 for β-poly(L-alanine). (B) SR microdiffraction pattern of spider dragline silk (ID13-results; unpublished).

Models for macroscopic function

In this section we will mention several models, which have been made to simulate the mechanical properties of silks.

Molecular model

Hayashi *et al.*[24] schematize the sequence of protein silks as sets of shared amino acid motifs, described as secondary structures modules. Three structural modules are proposed. $(A)_n$ and $(AG)_n$ form β-sheet, crystalline domains in the fibre. The glycine-rich, $(GGX)_n$ repeat regions of MaSp1 form 3_{10} helix structures, which could serve as link or transition between crystalline β-sheet domains and less rigid protein chains. The glycine and proline rich repeat of MaSp2 conforms to a β-spiral, showing a similar structure to a spring. This structure is proposed to serve as the elastic mechanism of the fibre. Such a model allows understanding silk properties only in qualitative way.

Group Interaction Modelling

Porter *et al.*[25] use a mean field modelling method of the interaction of characteristic structural units, which has been developed to predict the engineering properties of a range of man-made polymers. This model assumes that silk consists of hydrogen-bonded chains

arranged in ordered and disordered regions. The more rigid ordered domains are dispersed at a nanometre scale within the less rigid amorphous phase. The main difference between the ordered and disordered structures is the density of hydrogen bonds. It allows the structure-properties relations to be efficiently predicted, in terms of chemical composition and rather simple morphological structure.

Hierarchical models

Termonia's network model[9] relies on molecular modelling of crystalline and amorphous phases. The amorphous phase is depicted by entangled chains, linked together by hydrogen bonding. The role of the crystallites is to reinforce the matrix via a constrained interface layer. This model simulates properties in agreement with observations, while highlighting the importance of the interphase. The model can also explain the influence of water on the mechanical properties by the effect of water molecule to prevent the formation of hydrogen bonds.

Gersappe[26] uses a molecular dynamics simulation approach to analyse the molecular mechanisms by which nanoscale filler particles reinforce polymeric matrices. This is therefore a two-phase model similar to Termonia's model. According to this model, the mobility of the nanoscale filler particles, which is similar to that of the surrounding matrix, is a key to its efficiency to increase the toughness of the polymer. The nanoscale crystalline domains observed in spider silk are assumed to play the same role as the nanoscale filler particles.

Scope for improvement of models

The predictive power of hierarchical models depends on an understanding of the structure and dynamics of silk. Thus, the influence of water on macromolecular properties and the nature of the nanometer-sized domains are not well understood at the microscopic scale. This requires experimental techniques sensitive to hydration-related changes in microscopic structure and dynamics. Neutron scattering techniques are particularly interesting in this respect due to the strong interaction of neutrons with hydrogen atoms.

METHODS

Les phénomènes de diffusion des rayons X comme des neutrons permettent d'obtenir des informations sur l'arrangement de la matière, couvrant des échelles allant de la structure interne, atomique, d'une molécule jusqu'aux agencements de macromolécules. Si l'on mesure par ailleurs le transfert d'énergie au cours de la diffusion inélastique, on obtient une information sur la dynamique des éléments diffuseurs. Les neutrons ont par ailleurs plusieurs particularités qui rendent les techniques de diffusion associées complémentaires de celles de diffusion des rayons X. Les neutrons sont diffusés par les noyaux des atomes, et non pas par leurs nuages électroniques. La nature nucléaire de cette interaction les rend sensibles à des atomes différents, mais aussi sensible au remplacement isotopique. La chimie d'une molécule n'étant que peu altérée par ce remplacement isotopique, il est possible en diffusion neutronique d'observer un objet ayant la même structure et les mêmes propriétés sous des angles différents. Par ailleurs, les neutrons utilisés ont une très faible énergie par rapport aux rayons X, comparable à celles des mouvements des atomes, ce qui facilite l'utilisation des techniques de diffusion inélastique. Le handicap de l'importante quantité d'échantillon requise est en partie compensé par la nature non-destructive des faisceaux de neutrons. Ainsi, les deux échantillons de respectivement 20 et 150 mg de fil de traîne de Nephila Edulis, spécifiquement collectés au département de zoologie d'Oxford en vue de ces expériences, ont pu servir durant plus d'une année de manipulations.

Dans la pratique, différentes techniques permettent de couvrir différentes gammes d'échelles et d'énergies. Les techniques employées au cours de ce projet sont la diffraction des fibres, la diffusions aux petits angles, la diffusion inélastique et quasiélastique mesurée par spectromètre de type "temps-de-vol" des neutrons et la diffusion quasiélastique mesurée par spectromètres à rétrodiffusion. Chacun des huit instruments utilisés durant le projet est rapidement décrit dans ce chapitre, et le détail des environnements et des protocoles de chaque expérience y est donné. La soie a été étudiée, suivant les instruments, dans différentes conditions d'humidité -essentiellement sèche, humidifiée par H_2O et humidifiée par D_2O- et de températures -de 20 K à température ambiante- sans qu'aucun signe de dégradations micro ou macroscopiques ne soit observé. Certains des outils et appareillages permettant de contrôler ces conditions expérimentales ont du être spécifiquement adaptés aux instruments et à l'échantillon. Enfin, la technique de diffraction des neutrons a été complétée par des simulations de clichés sur la base de modèles cristallins.

General introduction to X-ray and neutron scattering

In this section, we introduce briefly the foundations of X-ray and neutron scattering. The aim is to provide an introduction to the theory behind the techniques used during the project, also for non-specialists. In view of the experiments performed, the methodological emphasis will be put on neutron scattering. For further details, please refer to the textbooks, for instance G. L. Squires[27], M. Bée[28] and J. Als-Nielsen[29].

Interaction of X-rays and neutrons with matter

Both neutrons and photons can be described as particles and as waves. Thus the wave nature can be described by the *de Broglie* wavelength $\lambda = 2\pi/k = h/(mv)$, where **k** is the wave-vector[30]. For experiments reported in this work, wavelengths are of the order of one angstrom (10^{-10} m).

X-rays and neutrons interact in general weakly with matter, in particular organic matter. This implies that they are mainly transmitted through the samples studied in the present work without any change. The small interaction term with matter corresponds to three basic processes: (i) absorption (ii) refraction and (iii) scattering. Absorption and refraction by our sample are extremely small, and will be neglected. The discussion will therefore be limited to scattering processes.

Principle of a scattering experiment

Let us consider an incoming monochromatic beam of wavelength λ and momentum $\hbar k$ (Figure 7). Each particle of the sample may give rise to a scattered outgoing wave. The scatterers will be electrons in the case of X-rays, and nuclei in the case of neutrons. Due to the small size of scatterers with respect to the wavelength, they can be considered as point-like[1] and the scattered waves can be described as spherical. At a far distance (with respect to the wavelength, e.g. at the detector position) from the sample, the waves are described as plane waves.

[1] if we consider scattering by atoms, the approximation of point-like scatterers is valid for neutrons, while a correction is required for X-rays for which the atomic form factors depend on the scattering angle.

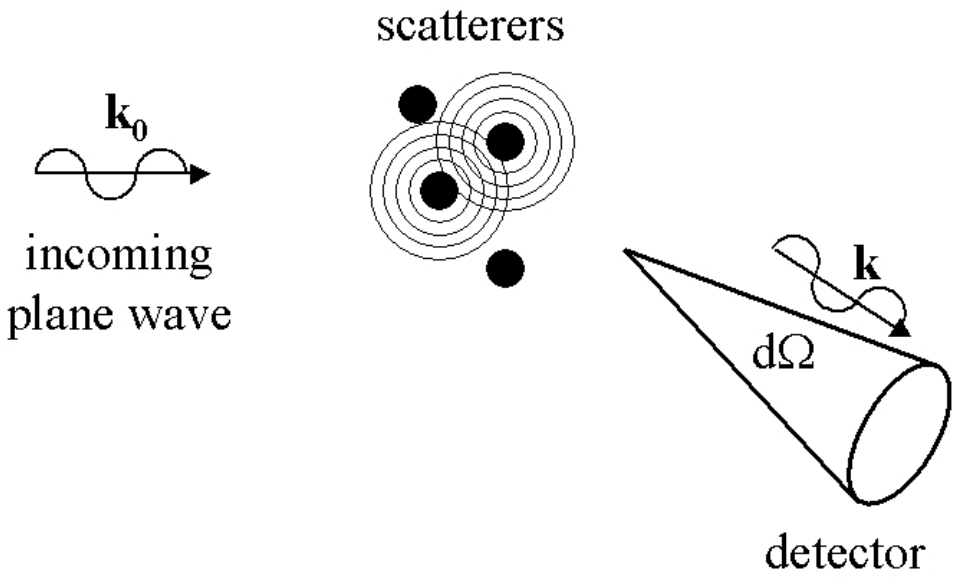

Figure 7 Scheme of a scattering experiment.

Figure 8 shows in general terms the different possibilities. The scattering vector **Q** is defined as the difference between the final and incoming wave vectors **k** and $\mathbf{k_0}$.

$$\mathbf{Q} = \mathbf{k} - \mathbf{k_0}$$

Q contains the relevant information, which are the scattering angle and the energy transfer ħω, defined as the difference between the final and initial energies of the beam.

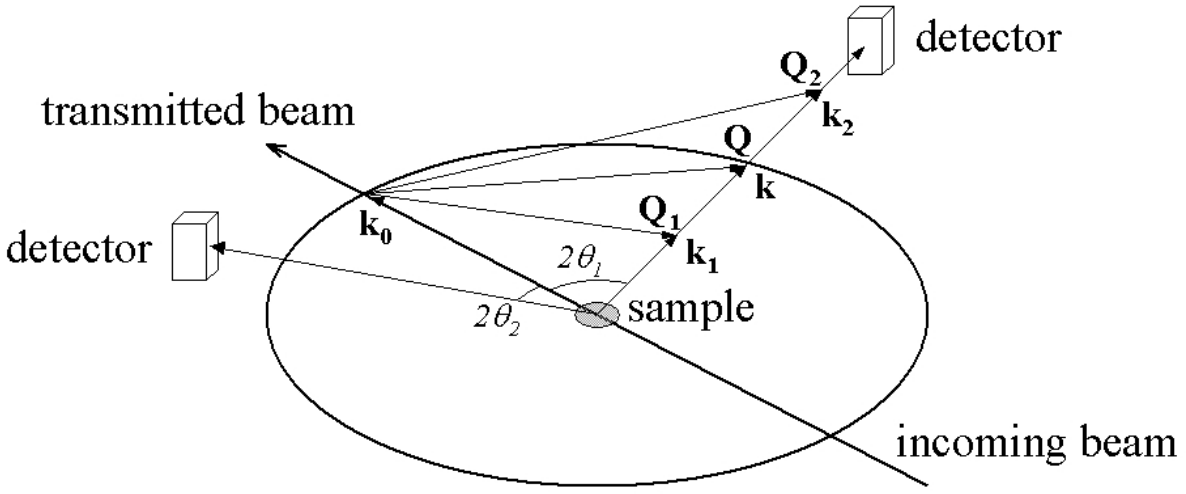

Figure 8 Scheme of a scattering experiment. For each 2θ scattering angle, the **Q** vector depends of the energy transfer. [from [28]]

Let us summarise the reason why such an experiment informs on the scattering material.

A scattering experiment allows to record an intensity by a detector at a given Q-value, which corresponds to the modulus squared of the sum of all scattered waves. In other words, the

intensity is given by the sum of all pair-products of each individual amplitudes. This means it contains information on the position of a scatterer with respect to all the others, or the so-called pair-correlation of scattering centres. For both X-ray and neutron scattering, scattering centres (electronic cloud or nucleus) are atom positions.

Scattering cross-sections and correlation functions.

The formalism introduced in this chapter will be the one used in neutron scattering. It can usually be analogously applied to X-ray scattering.

The double differential scattering cross-section per atom is the experimentally accessible parameter. The formulation given below (equation 1) corresponds to the kinematic approximation, or first Born approximation, in which it is assumed that there is no multiple scattering or that it can be neglected. Besides some specific cases (e.g. Bragg scattering of perfect crystals, total reflection from surfaces), this holds for X-ray and neutron scattering.
Within this approximation, the probability that a particle with initial energy E_0 and wave vector $\mathbf{k_0}$, impinging on a sample of N scatterers, is scattered with the final energy $E_0+\hbar d\omega$ and wave vector $\mathbf{k}$ into a small solid angle $d\Omega$ around the direction of $\mathbf{k}$ is :

$$\frac{d^2\sigma}{d\Omega d\varpi} = \frac{k}{k_0}\frac{1}{2\pi}\frac{1}{N}\int\left\langle \sum_{\alpha,\beta} b_\alpha b_\beta e^{-i\vec{Q}.\vec{r}_\alpha(0)} e^{i\vec{Q}.\vec{r}_\beta(t)} \right\rangle e^{-i\omega t} dt \qquad (1)$$

Where the double sum on the indexes α and β relates to the species of scatterers, $\mathbf{r}_\alpha$ and $\mathbf{r}_\beta$ are their position, b_α and b_β are the scattering lengths, and $\mathbf{Q}$ the previously defined scattering vector. For more detailed explanations and justifications, please refer to text books [28, 30, 31].
Let us now consider the simplest case of identical scatterers, all with the same b. It appears that the average, which includes a configurational average with respect to the coherence volume defined by experimental parameters, a time average during data collection, and a thermal average, is a function of $\mathbf{Q}$ and t. It is called the intermediate scattering function $S(\mathbf{Q}, t)$.

$$S(\vec{Q},t) = \frac{1}{N}\left\langle \sum_{\alpha,\beta} e^{-i\vec{Q}.\vec{r}_\alpha(0)} e^{i\vec{Q}.\vec{r}_\beta(t)} \right\rangle \qquad (2)$$

The Fourier transforms of S(**Q**,t) are, in space, the pair-correlation function G(**r**,t) (where **r** describes the difference vectors $\mathbf{r}_{\alpha\beta} = \mathbf{r}_\alpha(0) - \mathbf{r}_\beta(t)$), and, in time, the dynamic scattering function S(**Q**,ω). S(**Q**,ω) is therefore the Fourier transform in space and time of G(**r**,t). These are the essential quantities.

The dynamic scattering function then appears in the simplified equation (1) as:

$$\frac{d^2\sigma}{d\Omega d\varpi} = b^2 \frac{k}{k_0}\frac{1}{\hbar} S(\vec{Q},\omega) \tag{3}$$

S(**Q**,ω) therefore is deduced from the measurement, under specific conditions depending on the instrument. We then can deduce the pair-correlation function from it.

There is a clear interpretation of the pair-correlation function G(**r**,t). It gives the probability that there is a particle at the place **r** and time t, when there has been a particle at place 0 and time 0.

For instance, it can provide a description of the structural properties of a crystal. There, the unit cell corresponds to well-defined equilibrium positions at $t \to \infty$, G(**r**, ∞), and the measurements will consist in the determination of the corresponding purely elastic scattering contribution S(**Q**, 0) (Figure 9, left). Another observable phenomena will be the periodic motion of lattice vibrations, which will cause inelastic scattering, S(**Q**, ω) with $\omega \neq 0$ (Figure 9, middle). And finally if relaxation processes or diffusion of particles occur, we will observe the so-called quasi-elastic broadening of the scattering S(**Q**, $\omega \approx 0$) (Figure 9, right).

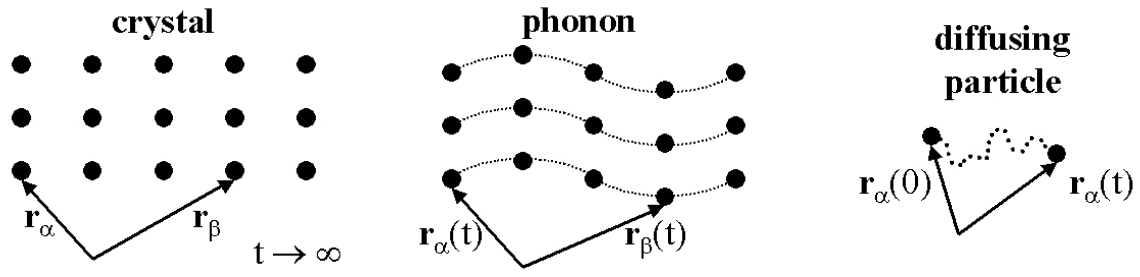

Figure 9 Left: case of crystal lattice, purely elastic scattering S(**Q**, 0) occurs at Bragg peaks. Middle: lattice vibrations; here a phonon mode gives rise to inelastic scattering S(**Q**, ω). Right: diffusive motion of a single particle leads to quasi-elastic scattering S(**Q**, $\omega \approx 0$).

Many approximations are made in the current descriptions for which more complete formulations can be found in the references. We can, however, most of the time still apply these interpretations for realistic samples (especially, with different sorts of scatterers) to get a suitable description, based on general and common functions to all techniques presented here.

To summarise, a scattering experiment allows to measure the dynamic scattering function or at least a part of it, and from its Fourier transform in space and time, we obtain the pair-correlation function G(**r**,t) or the corresponding part of it, which describe the microscopic properties of the sample.

Fibre diffraction

The relevant features of a fibre diffraction pattern will be described in the following subchapter. It will use the general principles of crystallography. For an introduction on crystallography, please refer to textbooks such as [29].

The diffraction pattern of semicrystalline polymers such as spider silk consists of broad Bragg peaks, due to the presence of crystallites, superimposed upon a background, which includes the scattering by the amorphous component. The crystalline fraction is usually described in terms of crystalline domains, or crystallites. In general, the crystallites have one of their crystallographic axes, denoted **c** in Figure 10, aligned along the fibre axis, whereas the azimuthal orientation of the **a** - **b** plane is random. This implies that all the lattice nodes will be distributed along concentric circles around the fibre axis in a similar way as for a rotated single crystal (Figure 10).

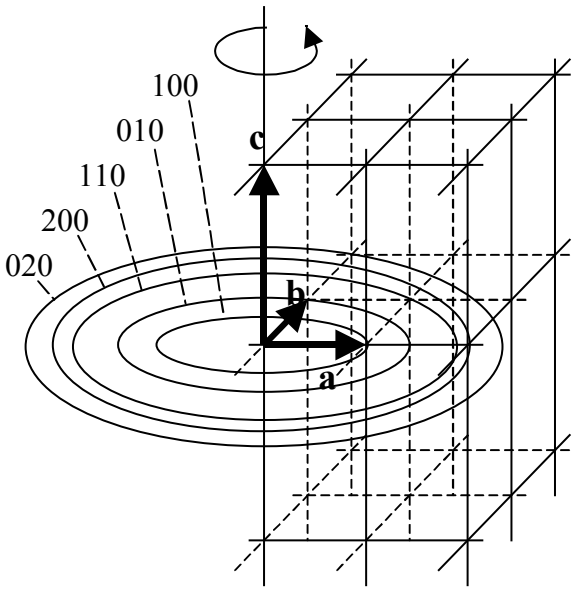

Figure 10 Schematic view of the effect of the distribution in space of uniaxially oriented crystallites. For simplification, only part of the equatorial nodes distribution are represented in the form of concentric circles (from [32]).

In fibre diffraction geometry, the incident beam is generally perpendicular to the fibre axis. In such a case, the reciprocal lattice will always intersect the Ewald sphere and will give rise to a number of reflections on a flat screen as seen in Figure 11.

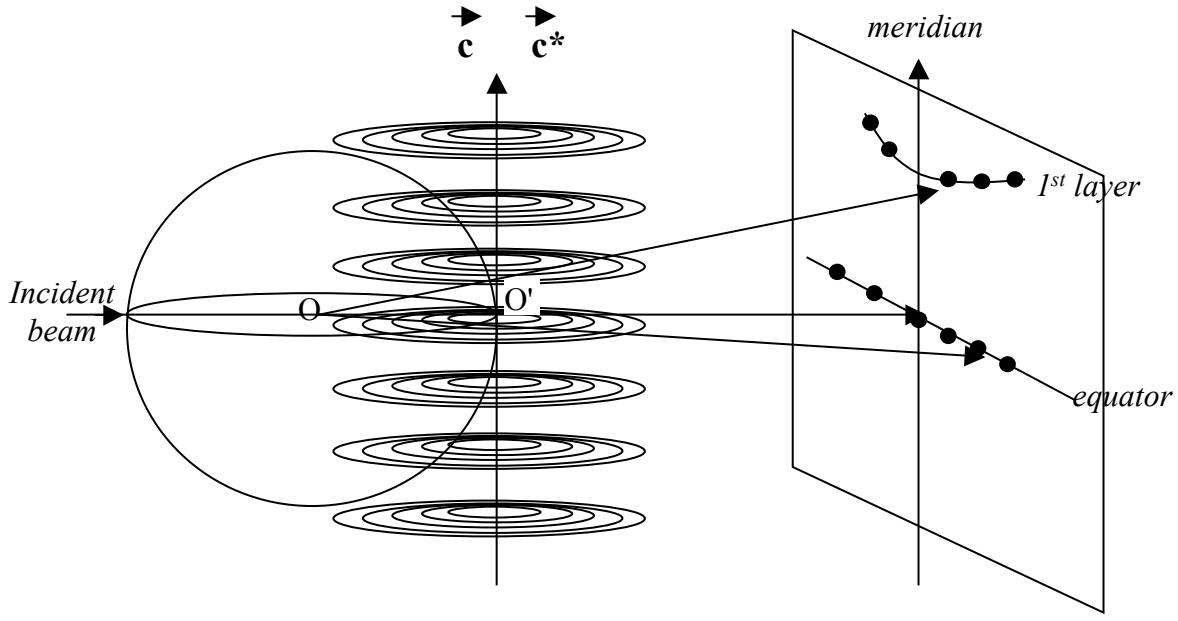

Figure 11 Geometry of fibre diffraction and corresponding diffraction pattern where only the equator and the first upper layer line are represented (from [32]).

Bragg reflections therefore occur in layers at $Q_z = lc^*$ with $l = 0, \pm1, \pm2, ...$, etc. and $c^* = 2\pi/c$. The l=0 layer is called the equatorial layer or equator. The fibre axis is called the meridional

axis or meridian. From the intensity of the diffraction spots and by measuring their distance to the origin of the pattern, one can identify the crystal system and establish the unit cell parameter **a**, **b**, **c**.

Due to the imperfect alignment of the crystallites along the fibre axis and for other crystalline imperfections such as their finite size, the lattice points show an extension in reciprocal space. Instead of well defined circles, they show an arcing. Consequently the reflections observed on the diffraction pattern are no longer point-like but rather broad arcs. A typical diffraction pattern is shown schematically in Figure 12, which gives an overview of possible contributions to the diffraction pattern from the polymer microstructure and dynamics. The Bragg spacing (1) informs on the crystal lattice parameters. The azimuthal width (2) is related to the degree of orientation of the crystallites. The radial width (3) depends on the size of the crystalline domains, on the crystal lattice parameters and on thermal vibration. The amorphous content gives rise to the background scattering (4).

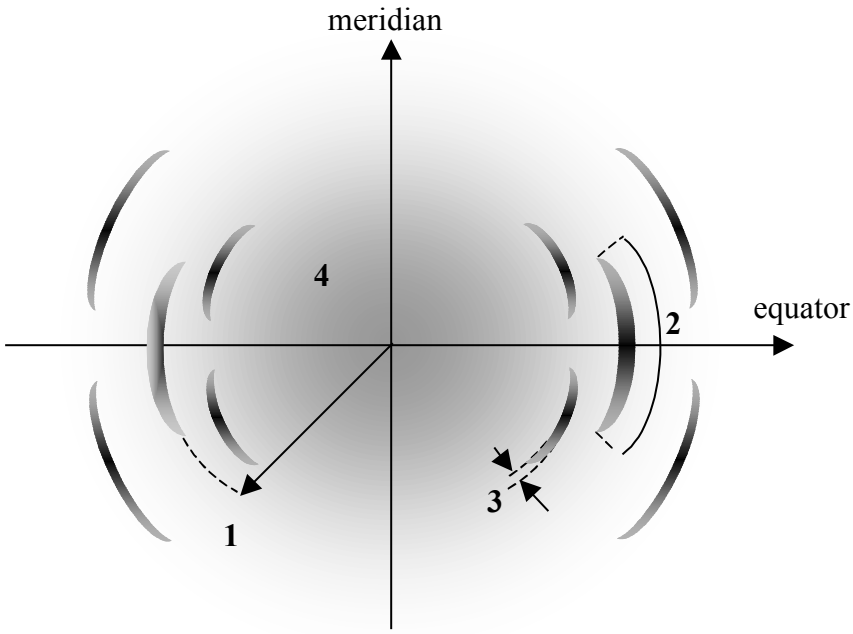

Figure 12 Schematic fibre diffraction pattern and its typical features (see text, from [32]).

X-ray and neutron sources

The Grenoble research campus ("polygone scientifique") combines two international facilities for scattering experiments, namely the ILL and the ESRF. The partner countries are mostly from Europe with notable exceptions such as Russia (ILL) and Israel (ESRF). Both sources

are brilliance optimised (intensity per unit-time per solid angle per cross-section area per energy interval) and belong to the most brilliant worldwide. (brilliance is in the case of SR also called "spectral brightness")

Neutron sources[33, 34]: there are basically two ways currently available to produce neutrons for scattering experiments, namely nuclear spallation and nuclear fission. Spallation makes use of a proton beam to collide with a heavy-metal target, driving neutrons from its nuclei. The difficulty in designing a spallation source is to handle the emerging heat and shock-waves. Fission makes use of a nuclear chain reaction. The brilliance is then essentially given by the spatial density of the fissile material. Thus, the limit in brilliance for a nuclear fission reactor is essentially determined by the cooling efficiency per volume. Boundary conditions for cooling are given by the wavelength distribution, since this distribution is also defined by the coolant. The neutrons produced have energies up to tens mega-electron volts (MeV), and the corresponding wavelengths are too short for investigating condensed matter. Furthermore, such neutrons tend to damage solids. Therefore, neutrons must be "cooled down" for scattering experiments. The cooling is done by bringing the neutrons into thermal equilibrium with a moderating material. The material used has a large scattering cross section, such as water or liquid hydrogen. The moderator is placed close to the neutron source. Neutrons enter the moderator and, after a series of collisions in the material, lose energy until they reach those of the atoms of the moderator. The ILL is a nuclear reactor optimised for low energy neutrons (so called cold and thermal neutrons as introduced later in this chapter) which are ideal for most scattering experiments. In the next sections, cold or thermal sources will refer to moderators emitting the corresponding cold or thermal neutrons.

Synchrotron radiation sources[35, 36]: SR consists of electromagnetic waves emitted by accelerated relativistic particles (electrons or positrons). Such electromagnetic radiation is highly collimated and the range of accessible wavelengths depends on both the electron energy and the local acceleration of the particle. The ESRF operates close to 6 GeV and the photons are produced from the visible range up to the very hard X-ray regime of about $2.5*10^{-12}$ m. The useful spectral range starts in the IR-range with many experiments performed in the range 10^{-10} m to $2*10^{-10}$ m.

The ESRF consists of:

- a linear accelerator which accelerates electrons emitted from an electron gun to energies ranging of a few hundreds MeV or more.
- a circular booster synchrotron which accelerates electrons as bunches close to 6 GeV.
- a storage ring where relativistic electrons are periodically injected with a specific bunch structure. The energy of the circulating electron bunches is maintained by radiofrequency cavities.

The storage ring is in reality a polygon consisting of straight sections joined by strong bending magnets. SR is emitted from bending magnet sections and from periodic magnetic elements -called wigglers or undulators- which are installed in the straight sections. Wigglers and undulators consist of a series of individual magnets oriented in such a way as to induce a lateral sinusoidal trajectory of the electrons. Wigglers emit a broad continuum wavelength range, while undulators will show a quasi monochromatic narrow bandwidth radiation at well defined energies.

Specific properties of neutrons

Energy

For scattering experiments, neutrons of low energy (thermal or cold) are used. The energy of a free neutron corresponds to its kinetic energy, $E = (1/2)mv^2$. For a *de Broglie* wavelength $\lambda = 2\pi/k = h/(mv)$ of 10^{-10} m, this corresponds to an energy of about 50 meV. At the same wavelength, the X-ray photon has an energy $h/(c\lambda)$ of approximately 12 keV.

The low energy of a neutron together with its neutral charge implies an absence of any radiation damage to the sample. This is very useful for precious samples -such as the silk used in the present work- as one can use the same sample for multiple experiments.

As we have seen in the source section, the neutrons initially produced by the sources have too high energies (or too low wavelength) for condensed matter studies. In order to lower this energy, they are "cooled down" by passing through a moderating material having the temperature T. The distribution of speeds of the neutrons in the beam then obeys a Maxwellian distribution around a mean value v such as $E = (1/2)mv^2 = (3/2)k_BT$, where k_B is the Boltzmann constant.

One thus talks of temperature for neutron beams. "Thermal" neutrons, corresponding to T = 300K, have an energy of about 25 meV and a wavelength of the order of 0.18 nm. When we talk about "cold neutrons", it refers to lower temperature, therefore lower energies and longer wavelength.
The energy of thermal and cold neutrons is of the same order of magnitude as intermolecular energies in condensed matter. It therefore is suitable to probe not only structural but also dynamical properties at the microscopic scale.

Interaction with nuclei

The interaction neutron-nuclei depends on magnetic and nuclear forces. Neutrons can therefore probe the magnetic properties of a sample, but this property is not relevant in our studies, where magnetism can be neglected. Concerning the nuclear forces, they occur only at short distances (10^{-14} - 10^{-15} m) compared to the wavelength (10^{-10} m). Scattering is therefore isotropic, and can be characterised by a unique parameter, the scattering length b. Most of the time in neutron scattering experiments, this parameter is real and energy-independent.

However, and this is of particular interest, the scattering length b does not vary in a regular manner for different elements, in contrast to X-rays. In addition, it varies from one isotope to another, as shown in Figure 13. A very useful property of neutron scattering is its sensitivity to light atoms and in particular hydrogen atoms. It therefore is very suitable to probe water.
Another interesting property comes from the variation in scattering lengths from one isotope to another, which is used in isotopic-labelling and contrast variation techniques. This will be described in more detail in a further subchapter.

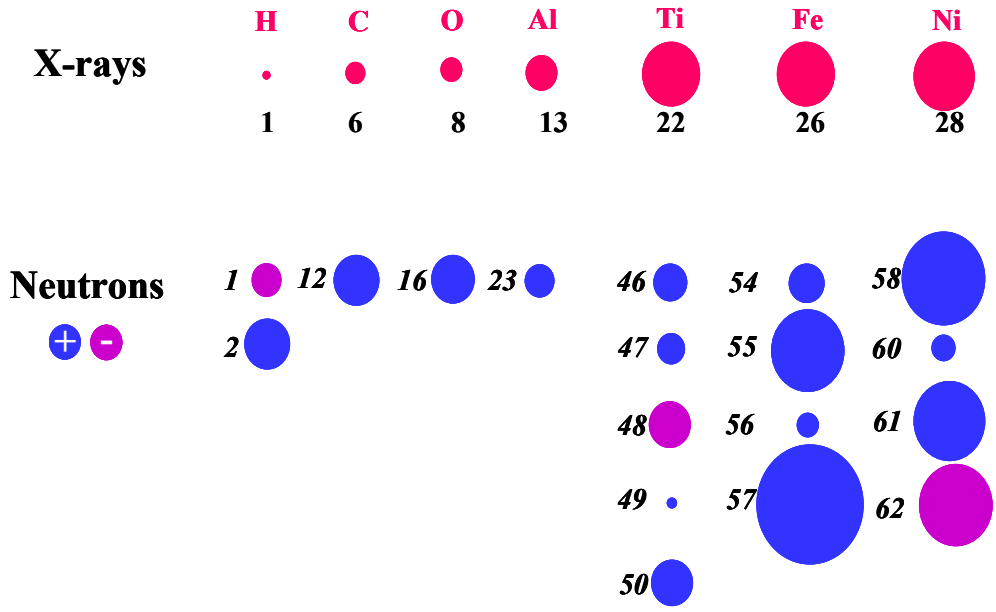

Figure 13 Scattering length for X-rays and neutrons, for different elements[37]. Note that X-rays are scattered by the electron clouds. The size of the spheres is proportional to f (sinΘ=0). Neutrons are scattered by the atomic nuclei. The size of spheres is proportional to b.

Incoherent scattering

The existence of nucleic incoherent scattering in neutron scattering has no equivalence with X-rays[2]. Coherent scattering (of X-rays or neutrons) occurs if all atoms of the same species have the same scattering length (which is always the case with X-rays, as it then only depends on the number of electrons). Scattered waves from all scatterers may then interfere with each other, and the scattering depends on relative distances between the constituent atoms. Elastic coherent scattering then tells us about the structure at the equilibrium (similar to Figure 9, left) and coherent inelastic scattering provides information about the collective motions of the atoms (similar to Figure 9, middle).

Incoherent scattering appears in neutron scattering because not all scatterers have always the same scattering length. The first reason for this is that different isotopes have different scattering lengths. Because isotopes are randomly distributed, the scattered waves don't interfere, which leads to incoherent scattering. But even a unique population of isotopes may actually give different scattering lengths. Indeed, a neutron has a spin of 1/2, and the interaction depends on the actual spin of the compound system of the neutron and the nucleus. The sum of a non-zero nuclear spin s with a spin of one half leads to two values of spin for the

[2] The term "coherence" is widely used in scattering and always refers to geometry considerations. In that case, we are talking about coherence from nuclear configuration.

compound (s + 1/2 and s - 1/2), which will leads to two possible values of scattering length b^+ and b^-.

For each isotope, we can distinguish a coherent scattering length b^{coh}, corresponding to the mean value of the different scattering lengths over the different spin states, and an incoherent scattering length b^{inc} which will be the average standard deviation. The corresponding coherent and incoherent scattering cross-sections are defined by $\sigma_{coh} = 4\pi(b^{coh})^2$ and $\sigma_{inc} = 4\pi(b^{inc})^2$. The values for several isotopes are summarised in Table 2. The cross-sections are given in barns (1 barn = 10^{-24} cm^2)

Table 2 Scattering lengths and cross-sections of a few elements. Positive or negative scattering length values correspond to the repulsive or attractive nature of the interaction[28].

	Z	A	b^{coh} (10^{-15} m)	b^{inc} (10^{-15} m)	σ_{coh} (barns)	σ_{inc} (barns)
H	1	1	-3.742	25.217	1.76	79.91
D	1	2	6.67	4.033	5.597	2.04
C	6	12	6.653	0	5.563	0
O	8	16	5.805	0	4.235	0
Al	13	27	3.449	0.26	1.495	0.01
V	23	51	-0.402	6.42	0.02	5.19

In the simplest case of a single isotope, with a nuclear spin zero, all scattering lengths will be equal and the scattering is completely coherent. That is the case of ^{12}C or ^{16}O.

Hydrogen (^1H) on the other hand shows a very strong incoherent scattering cross-section, actually the largest of all elements and isotopes. Vanadium is a nearly completely incoherent scatterer, and is therefore often used as reference sample for calibration of instruments.

Inelastic or quasielastic incoherent scattering may be due, for example, to the interaction of a neutron wave with the same atom but at different positions and different times, providing information for instance about atomic oscillation or diffusion (similar to Figure 9, right).

Sample preparation

Collection: Silk fibres were collected by the "forced silking technique"[38] from *Nephila edulis* spiders, which were reared at the Oxford University zoology laboratory[39]. Spiders were anaesthetised only lightly and well prior to silking in order to avoid an influence on the

microstructural properties of the silk. The silk was directly spun onto a dedicated aluminium sample holder. Thus, two well-aligned silk samples of 20 mg and 150 mg were collected (Figure 14).

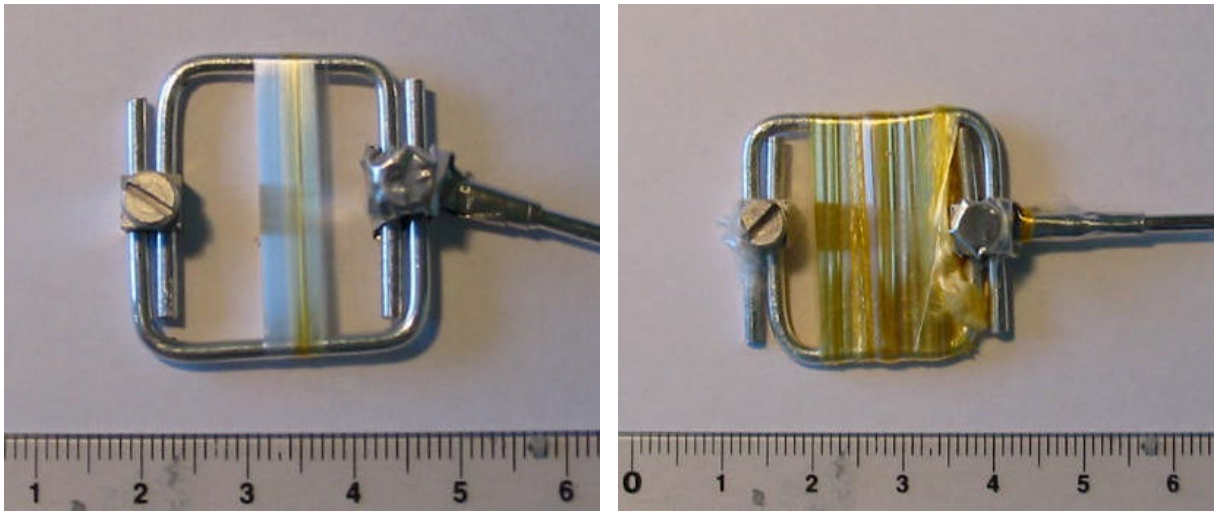

Figure 14 aligned bundles of *Nephila edulis* spider dragline silk on their aluminium sample holder. Left: 20 mg sample. Right: 150 mg sample. The attached hooks were used to rotate the sample holder during the silk collection, and were removed for the experiment.

Preparation: All experiments reported in this thesis report were carried out within about one year. The samples were stored under cool and dry conditions. For the experiments, hydration with H_2O or D_2O was performed using three different protocols:

- soaking of the sample, usually for a short time (up to one minute in D_2O). They were however both soaked for more than one hour once, during the D16 experiment.
- storage of the sample in an atmosphere saturated with H_2O or D_2O (see Figure 15) for times between 12 to 36 hours.
- *in-situ* humid air flow in the sample enclosed environment. The details of this protocol depend on the instrument on which it was performed, and thus will be detailed in the corresponding sample environment paragraphs.

Figure 15 Hydration of the 150 mg silk sample stored in a dessicator. Water (H_2O or D_2O) is put in the reservoir under the sample.

The ageing of the sample, the hydration processes and the changes of temperature during neutron experiments may have lead to a degradation of the sample. Therefore, a few fibres were taken from the 150 mg sample after the series of neutron experiments which included several hydration and cooling cycles. The X-ray patterns of these fibres were acquired. The quality of the patterns showed no sign of degradation.

Instruments and experiments

The aim of this section is to provide an overview of the different instruments, which were used for the specific case of spider silk. For details, see *ILL Yellow book*[34] and [40] for SR-microdiffraction instrumentation. The experiments performed will also be described in detail after each presentation of the corresponding instruments.

We were very fortunate in obtaining almost all the beamtime required on each instrument, plus benefiting occasionally of test beamtime. An important number of experiments could be thus performed. A few of them are not yet fully analysed, for various reasons (unsuccessful or simply lacking time), but are still presented here in detail in order to summarise all the information required for a further analysis.

Neutron diffraction and small-angle scattering

D19 instrument: four-circle diffractometer at thermal neutron source

- Decription of instrument

D19 is located at a beam tube close to the reactor, which allows preserving the full thermal spectrum. A set of three different monochromators, each of them at four possible positions, allows selecting the wavelength between 0.1 to 0.24 nm. The beam size is defined by a nosepiece.

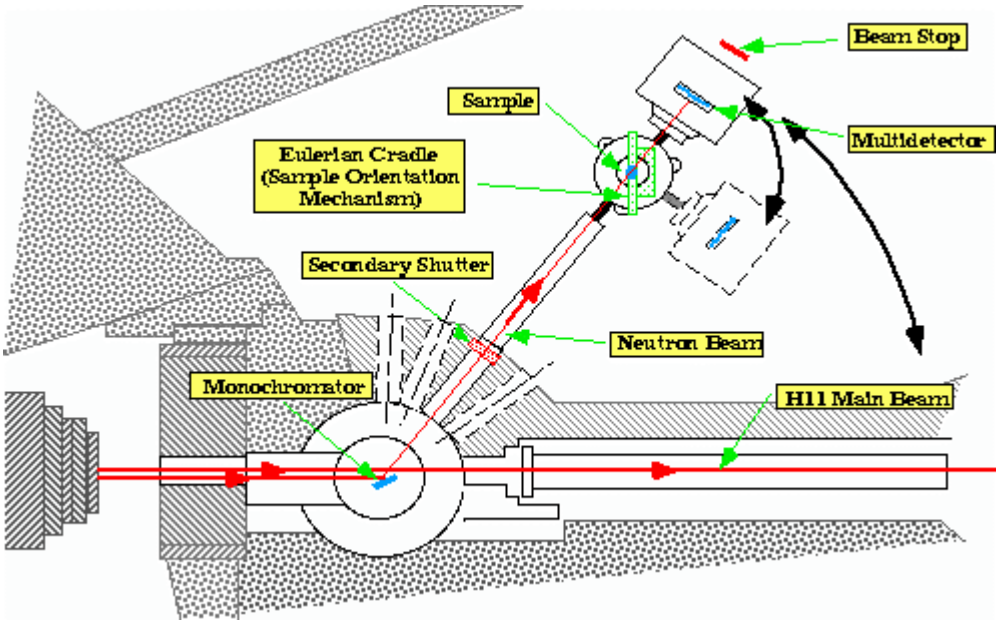

Figure 16 Sketch of the layout of the D19 four-circle diffractometer.

Data were collected on a 64*64 pixels ^{3}He gas-filled detector with a 200 mm^{2} active area placed at 568 mm from the sample.

- Sample environment

An Eularian cradle (Figure 17) allows to orient the sample through the control of three angle parameters, a ω-circle which rotates the χ-circle on which is carried the φ-axis.

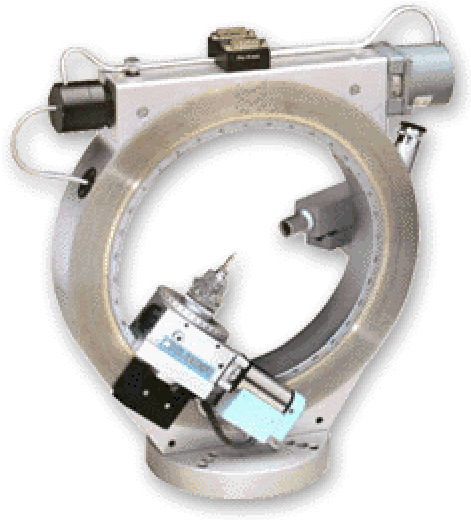

Figure 17 Typical Eulerian cradle used for X-ray crystallography.
Source:www.xhuber.com/en/positioning/circle/500/511/511/511.htm

A fourth angle γ corresponds to the detector position, or 2θ. One can record a complete fibre diffraction dataset, covering the whole reciprocal space, by using several exposures at different fibre tilts. For the first spider silk experiment, a full fibre diffraction pattern up to a 2θ angle of 60° was covered in 28 angular positions. The data recorded are merged to form a composite image in reciprocal space using the ILLD19 program which uses the equations given by Fraser et al.[41]. Moreover, the D19 sample environment is equipped with an automated humidity control system [42] (Figure 18). The relative humidity is controlled by varying the proportion of a mixture of dry and wet gas that is passed through the sample enclosure. The compressed air can be dried by passing it through dehydrated silica gel. Its flow is then split into two lines: a wet line where the gas is humidified by bubbling it through water, and a dry line. The relative humidity is monitored with a humidity probe and the proportions of the gas mixture are varied to keep the chosen RH value of 80% by an electronically controlled valve. In addition to the RH control, the water used can be a mixture of D_2O and H_2O, which allows performing contrast variation techniques.

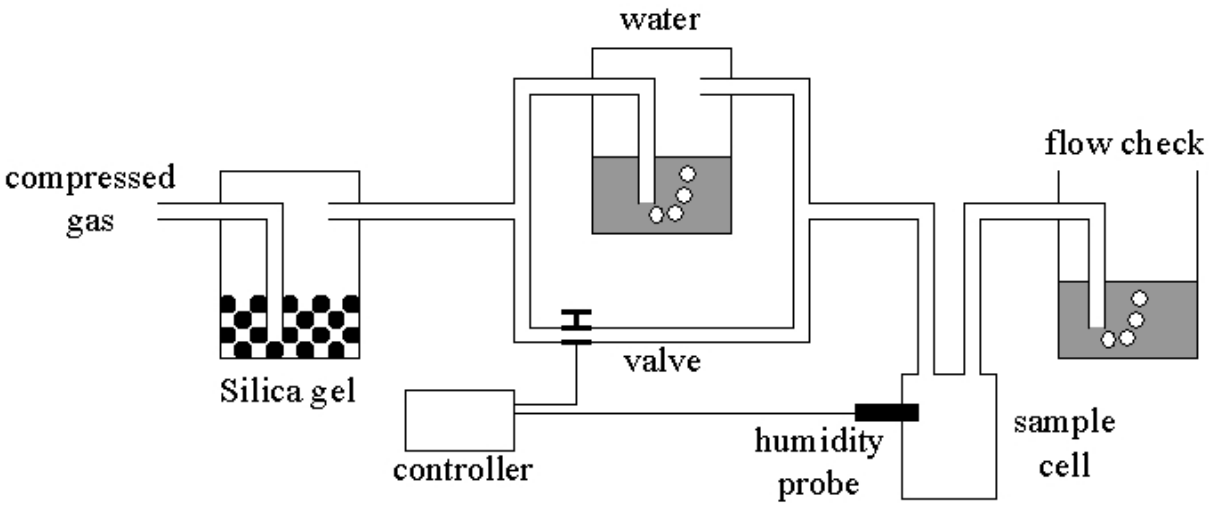

Figure 18 Schematic diagram of the automated humidity control system on D19 [from [42]]

The first experiment was performed with the 150 mg sample. Its aluminium square frame was fixed on top of a goniometer head installed on the Eulerian cradle. The sample was at the centre of rotation of the cradle circles, enclosed in the humidity cell. In order to cover the whole reciprocal space it is necessary to rotate the sample. A total of 28 different combinations of angular positions were used. The positions were chosen to minimise the shadowing of the aluminium frame. The sample was forming a flat rectangle of approximately 15x25 mm. The beam had a circular shape of 10 mm of diameter. Assuming a constant distribution of sample on this surface, the estimated amount of illuminated sample is therefore, depending on the orientation of the sample, of 30 mg (sample perpendicular to the beam) to 35 mg (for the maximum inclination of 30° of the sample with respect to the beam).

The conditions were similar for the second experiment, except that the frame of the sample of 20 mg was fixed together with the frame of the 150 mg sample.

- Data acquisition

Both experiments were performed at a wavelength of 0.24 nm, for which the flux is the highest on D19.

First experiment (number: 9-11-965)

For the detector response correction a standard vanadium calibration sample pattern was recorded. For each angular position, the acquisition is performed until a predefined count of neutrons is reached on the monitor, corresponding to about 20 minutes. The sequence of the experiments was as follows:

* acquisition of vanadium for detector response
* two complete data sets (the 28 angular positions previously mentioned) for silk humidified with D_2O

* D_2O-humid silk acquisitions for the higher angles (for $2\theta = 40°$ and $2\theta = 60°$)
* sample removed and acquisition of the empty cell for background correction

The sample was then mounted again at the same position. Only the aluminium frame was removed from its support, which conserves especially the relative orientation of the sample. Thus the position of the sample is reproduced with a precision of less than one millimetre.

* D_2O-humid silk acquisitions at the angular positions corresponding to the weak peaks (total acquisition time on D_2O-humid silk: about seven days)
* sample removed and acquisition of the empty cell
* acquisition of vanadium
* H_2O replaced with D_2O
* three complete data sets for silk humidified with H_2O
* H_2O-humid silk acquisitions for weak peaks (total acquisition time on H_2O-humid silk: about four days)

Second experiment (number 8-02-324)

For the detector response correction a standard vanadium calibration sample pattern was recorded. The acquisitions correspond to a unique series of 20 angular positions, covering the reciprocal space up to a 2θ angle of 60°. This sequence let some small gaps in the reciprocal space, at positions were no reflections are expected. For each angular position, the acquisition is performed until a predefined count of neutrons is reached on the monitor, corresponding to about 15 minutes. The sequence of the experiments was as follows:

* 15 acquisitions of D_2O-humid silk
* 9 acquisitions of the empty cell
* 31 acquisitions of D_2O-humid silk

This second experiment on D19 is mentioned for completeness but its results are not directly used for the analysis.

D16 instrument: four-circle diffractometer at cold neutron source.

- Instrument description

D16 is installed on a cold neutron guide. It is a four-circle diffractometer used in a similar way than D19, therefore no further description is given. Data were collected on a 128*128 pixels and 2*2 mm^2 pixel-size ^{3}He gas-filled detector placed at a fixed distance of 1000 mm to the sample position. The spider silk experiment was performed at a wavelength of 0.454 nm. D16 basically makes the junction between WANS and SANS experiments.

- Sample environment

The experiment was performed with both the 20 mg sample and the 150 mg sample, one after the other. Prior to the experiment, the 150 mg sample was soaked in D_2O. The aluminium frames were placed on top of a goniometer head inside the humidity chamber. The humidity chamber is installed on the Eulerian cradle of D16.

Two tubes were connected to the chamber: the incoming flow was dry air, which could be passed through a bottle of water containing different H/D ratios (Figure 19).

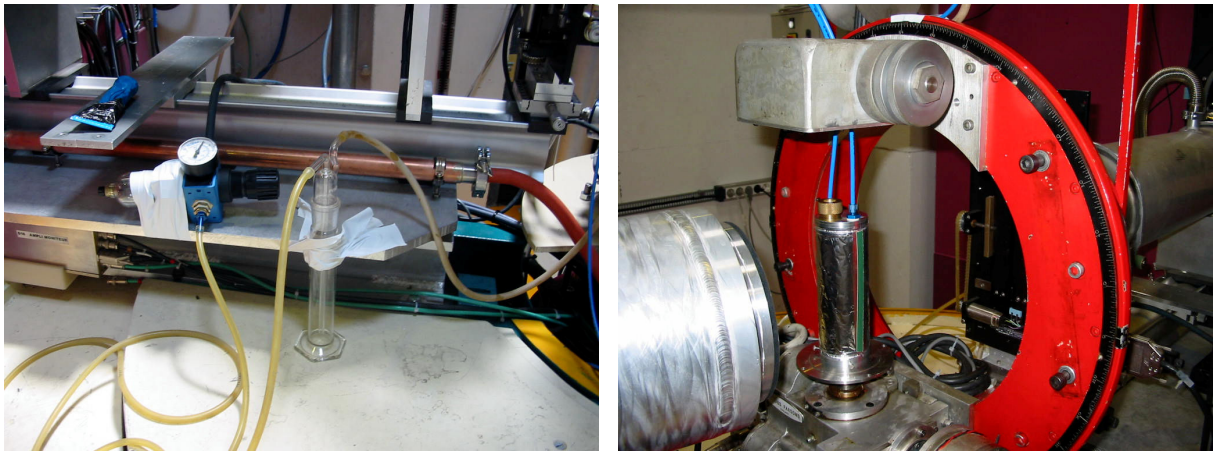

Figure 19 Hydration system on D16. Left: the dry compressed gas flow is controlled by a valve, and then passes through a bubbling bottle (empty on the photo). Right: the humidity chamber installed on the D16 Eulerian cradle. One tube is connected to the bubble bottle, the other tube ends up in a bottle of glycerol (not shown).

A valve controls the flow. In contrast to the D19 humidity setup, there was no mixing with a secondary flow of completely dry air, which allowed the relative humidity to be controlled. The evacuating tube ended up in a bottle containing glycerol, in which bubbles testify for the flow. During the experiment, when changing the mixture of D_2O/H_2O, only the bottle containing the hydrating water was removed and manipulated.

- Data acquisition

Acquisitions for the direct beam and for water calibration sample were performed before the experiment. The 20 mg sample was then placed in the humidity cell under a 100% D_2O-humid flow. The acquisitions were performed without beam stop. The detector was slightly tilted (centred at $2\theta=9°$) so that the direct beam is not detected (the detector cover an area of about +/- 7° from the centre to the edge). When nothing else is specified, data were collected for the equatorial and the meridional signals during 30 minutes each. The sequence was as follows:

* 14 acquisitions with silk under 100% D_2O-humid flow.
* 1 acquisition at higher scattering angle ($2\theta=54°$) along the equator.
* 4 acquisitions with silk under dry air flow.
* 2 acquisitions at higher scattering angle ($2\theta=54°$ and $2\theta=60°$) along the equator.
* 4 acquisitions with silk under 36 % D_2O-humid flow.
* 4 acquisitions with silk under dry air flow.
* 4 acquisitions with silk under 42 % D_2O-humid flow.
* 5 acquisitions with silk under dry air flow.
* 5 acquisitions with silk under pure H_2O humid flow.
* 3 acquisitions with silk under dry air flow.
* 9 acquisitions with silk under 8% D_2O-humid flow.
* 4 acquisitions with silk under dry air flow.
* 10 acquisitions with silk under 60% D_2O-humid flow.
* 4 acquisitions with silk under dry air flow.
* 9 acquisitions with silk under 80% D_2O-humid flow.
* 4 acquisitions with silk under dry air flow.

The 20 mg sample was then removed. Acquisitions for the empty cell, with an empty sample holder, were performed for 30 minutes at the different angular positions used. The sample was

soaked in H_2O and 9 acquisitions were performed with the silk under a pure H_2O-humid flow. However, there was a little hole in the thin aluminium foil of the humidity cell during the experiment, resulting in a small leak of the humid gas. The hole was created during the manipulation of the humidity cell when removing and placing back the sample. The previous sequence is not concerned. The humidity cell was repaired.

The 150 mg sample is soaked in D_2O for about 1h and then placed in the humidity cell under a pure D_2O humid flow. 4 acquisitions were performed, at 4 angular positions: the same meridional and equatorial positions as defined for the previous sequence, one position centred at $2\theta=54°$ along the equator and one position centred at $2\theta=19°$ along the meridian.

D11 instrument: small-angle neutron scattering instrument at cold neutron source

- Instrument description

D11 is SANS instrument with pinhole geometry located at a cold neutron source (Figure 20). The beam is monochromatized by a velocity selector providing a band pass $\Delta\lambda/\lambda=9\%$ (FWHM) . The experiment described below was performed at a wavelength of 0.6 nm.

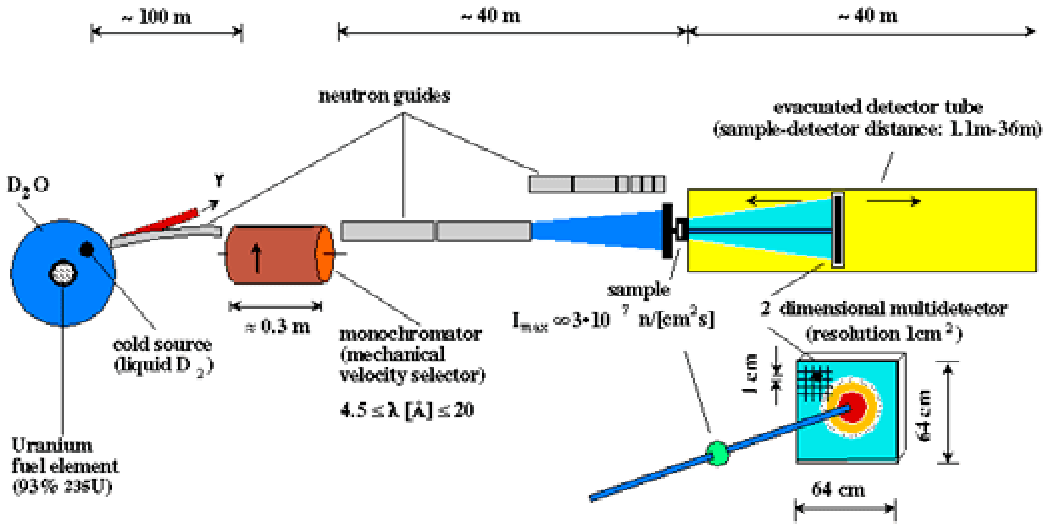

Figure 20 Sketch of the layout of the D11 SANS instrument.

A ^{3}He gasfilled detector of 64*64 pixels and 10*10 mm^2 pixel size was used at a distance of 1500 mm.

- Sample environment

The experiment was performed with the 20 mg sample, stored in a D_2O-saturated humid atmosphere for one day prior to the experiment. Its aluminium frame was placed on top of a goniometer head inside the humidity chamber. The goniometer head was used as a standard sample support, but not to precisely orient the sample.
The hydration system is already described in the D16 sample environment paragraph. The only difference is that there is no Eulerian cradle on D11. The humidity cell was scotched directly on the D11 sample area table. It was not moved during the experiment.

- Data acquisition

The acquisitions of cosmic background (no beam, cadmium mask), of the beam in air and of the empty humidity cell were performed. The sample was then placed in the humidity cell under a constant flow of pure D_2O-humid air. The patterns were always recorded during exactly 20 minutes. Transmission measurements were performed until a total count of 1000 is reached on the monitor (corresponds to about 3 minutes)
The sequence of the experiments was as follows:

* three patterns
* two transmission measurements

The bubbling bottle was then opened, the water removed in order to put the sample under a constant flow of dry air.

* seven patterns
* transmission measurement

The bottle of hydrating water was cleaned and filled with pure H_2O, so that the sample was under humid flow.

* 0%-D_2O humid flow
* four patterns
* transmission measurement
* switch to dry air flow
* four patterns
* transmission measurement

This sequence was repeated for the following H/D ratios: 8%, 16%, 42%, 70%.

At the end of the experiment, patterns and transmission are recorded for a standard water calibration sample, for the water container, and once more the empty beam background

D22 instrument: small angle neutron scattering instrument at cold neutron source

- Instrument description

The D22 SANS instrument was used in a similar way to D11 and does also not significantly differ from the D11 instrument with respect to the experiments performed. No description of the instrument will therefore be given. It was operated at a wavelength of 0.6 nm with detector-to-sample distances of 17000, 5000 and 1400 mm. The D22 data extend therefore to smaller Q-values than the D11 data. A ^{3}He gasfilled detector of 128*128 pixels and 7.5*7.5 mm^2 pixel size was used.

- Sample environment

The two samples of 20 mg and 150 mg were tested. They were stored in an enclosed atmosphere saturated with D_2O for about 12 hours before the experiment. They were then placed in an environment defined by glass windows with an opening to let the neutron beam going through. The conditions of the experiment were therefore atmospheric.

- Data acquisition

Acquisitions of the direct beam, to define the beam centre, were performed at the three detector distances. Transmissions of the water calibration sample, of the water cell and of the two silk samples were measured with the detector at 17000 from the samples. All these acquisitions were performed until a constant count of 2500 was reached on the monitor, corresponding to a time of about 2 minutes each. The next acquisitions on the silk were performed in 600 seconds, with the following sequence:

* acquisition of the air background during 1800 seconds at a detector distance of 17000 mm.
* 3 acquisitions with the 150 mg sample at a detector distance of 17000 mm.
* 9 acquisitions with the 20 mg sample at a detector distance of 17000 mm.
* acquisition of the air background during 1000 seconds at a detector distance of 5000 mm.

* 3 acquisitions with the 150 mg sample at a detector distance of 5000 mm.
* 6 acquisitions with the 20 mg sample at a detector distance of 5000 mm.
* acquisition of the air background during 1000 seconds at a detector distance of 1400 mm.
* 3 acquisitions with the 150 mg sample at a detector distance of 1400 mm.
* 3 acquisitions with the 20 mg sample at a detector distance of 1400 mm.

Neutron spectroscopy

General introduction to inelastic neutron spectrometers

Cold or thermal neutrons propagate with a speed on the order of the speed of sound (2.08 meV corresponds to 0.672 nm wavelength corresponds to 630 $m.s^{-1}$ propagation. Thus it is possible to infer on energy changes at the sample by measuring neutron speed changes through the flight time on a given path. This is the idea of time-of-flight (TOF) spectrometers. In order to measure a time, it is necessary to define a time t=0 and to "chop" the neutron beam in successive packets. The IN6 TOF spectrometer uses the so called "direct geometry". First, the energy of the incoming neutron packet is selected, and then the energy changes are detected.

The energy resolution of TOF spectrometers is, however, limited by the monochromaticity of the incoming beam. The energy resolution can be improved by the use of backscattering geometry. The basic idea is the first derivative of Bragg's law giving the error on the wavelength λ reflected by a crystal monochromator.

$$\frac{\Delta\lambda}{\lambda} = \frac{\Delta d}{d} + \frac{\Delta\theta}{\tan(\theta)} \qquad (4)$$

where d is the crystal lattice spacing and θ is the incident angle with respect to the crystal surface (Bragg angle). As becomes obvious from this equation, the Bragg angle contribution to the error vanishes at θ = 90°, when the incoming beam is scattered back into its incoming path, or "backscattered".

The principle of backscattering is used twice in classical backscattering spectrometers. At the primary spectrometer the wavelength is selected by a normal incidence reflection at the

monochromator crystal. At the secondary spectrometer, the final energy of the detected neutrons scattered by the sample is defined by a normal incidence reflection at the analysers.
For all backscattering spectrometers, the "inverse geometry" is used. The final energy is constant, while the incoming energy of the neutrons delivered by the primary spectrometer can vary. The shift can be induced either by changing the lattice parameter of the monochromator by changing its temperature or by a mechanical Doppler shift by fixing the monochromator on a moveable piston. The two methods are illustrated in the description of respectively IN10b and IN16 instruments.

General sample environment on neutron spectrometers

Spectroscopic experiments were carried out at temperatures from 10 K to 300 K. For such temperatures, the standard ILL "orange" cryostats were used (Figure 21). The refrigerant used is liquid ^{4}He evaporating near the sample.

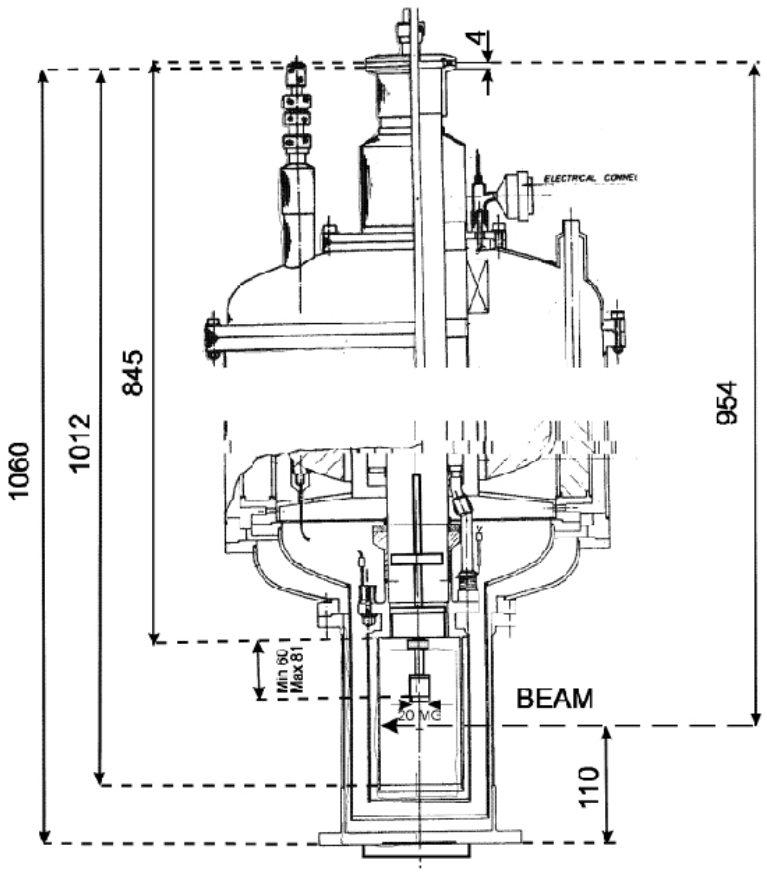

Figure 21 Technical drawing of an ILL "orange" cryostat. Lengths are given in mm. The neutron beam passes through thin aluminium walls. The sample environment can be cooled down to about 2 K.

The sample is loaded in the cryostat from the top using a cane through a central well. The cryostat is placed on the instrument so that its bottom end is on the path of the neutron beam. The cane is supported from above, at a high which can be adjusted for the vertical alignment of the sample with the beam. Once the cane is placed, the well environment is sealed. The air which potentially entered in the well is removed by pumping and replaced with helium exchange gas.

Standard canes comprise a platinum temperature probe close to the sample. Spider silk experiments were performed with specific canes, which comprise in addition one or two heatable capillaries going through the cane. These capillaries allow the gaseous sample environment to be controlled *in-situ* when the sample is at room temperature. The advantage of this method is that the exact alignment of the sample is maintained whilst its humidity state is modified. One of the main difficulty is that the cryostat well contains a "cold point", an intermediate position of the well which is always close to the temperature of liquid nitrogen (70 K), nearly independent of the sample temperature. The capillaries in the sample cane are thus heated to avoid condensation of water and a possible blocking by ice inside the capillary. The more successful single-capillary cane used for the present work features in addition an insulating vacuum between the capillary and the cryostat well. *In-situ* drying of the sample was performed using this single capillary cane, by pumping on the sample environment. The cane with two capillaries was developed for *in-situ* hydration of spider silk, for which a flow of humid gas passing through the sample environment is necessary. During the thesis project, however, condensation into liquid droplets of water could not be avoided. As this could lead to formation of crystalline ice at the surface of the silk once it is cooled down, data obtained with this hydration process were not taken into account for the analysis. More refinements are required for performing hydration inside a cryostated environment, however, it is noted that the main difficulties were surmounted.

The 150 mg sample was always used for spectroscopic measurements. It generally was oriented vertically, i.e. with the fibre axis perpendicular to the scattering plane.

IN6 instrument: neutron time-of-flight spectrometer at cold neutron source

- Instrument description

The IN6 TOF-instrument is designed for inelastic and quasielastic scattering experiments with a maximum energy transfer of about 200 meV and a resolution of the order of 100 μeV. It

performs "time-focussing" (Figure 22, for details see [34]), which allows improving the flux by a factor three as compared to a single monochromator setup, while maintaining the energy resolution. IN6 is installed on a cold neutron guide and can be operated at the wavelengths of 0.41, 0.46, 0.51 or 0.59 nm.

Data are collected on a fixed detector bank made of 337 ^{3}He counter tubes covering a Q-range of about 0.2 to 20 nm^{-1}. It is noted that it is also possible to obtain diffraction information from the inelastic spectra by grouping the intensities over all the energy channels.

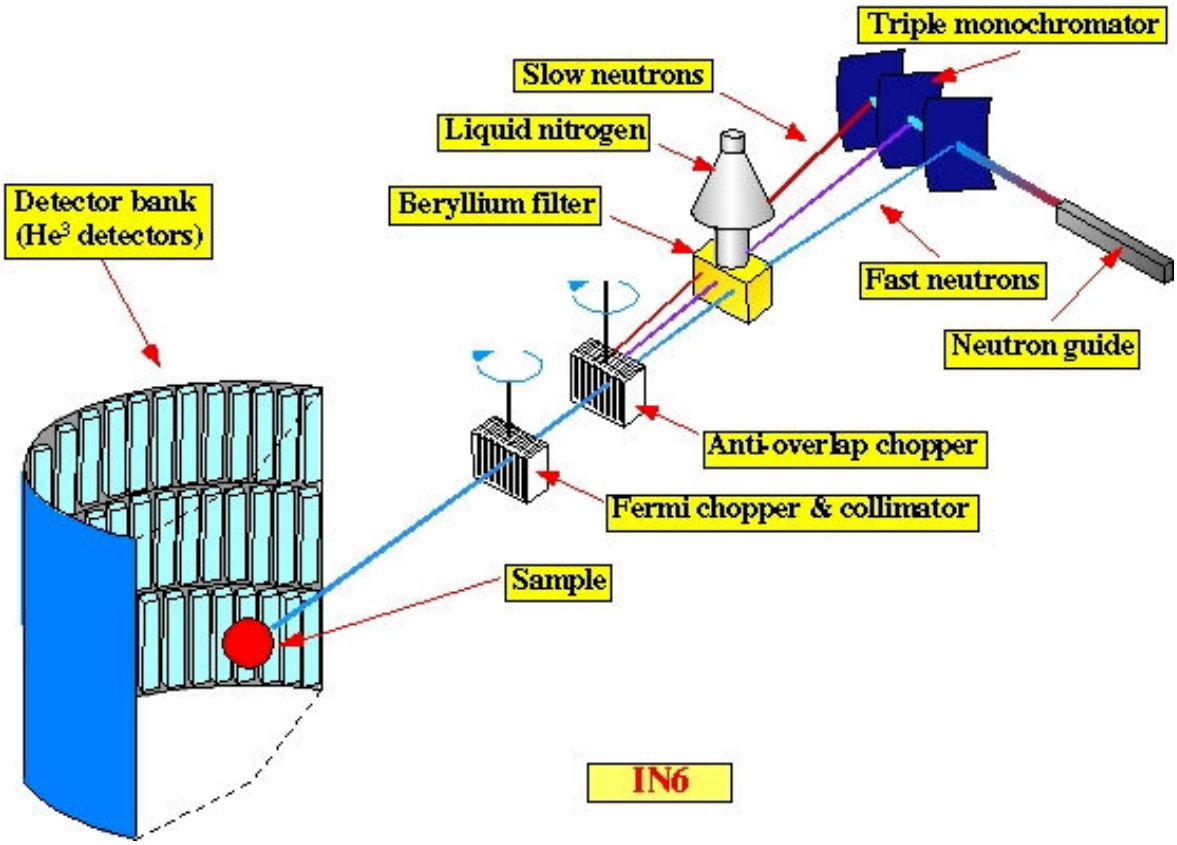

Figure 22 Sketch of the layout of the IN6 time-of-flight spectrometer.

- Sample environment

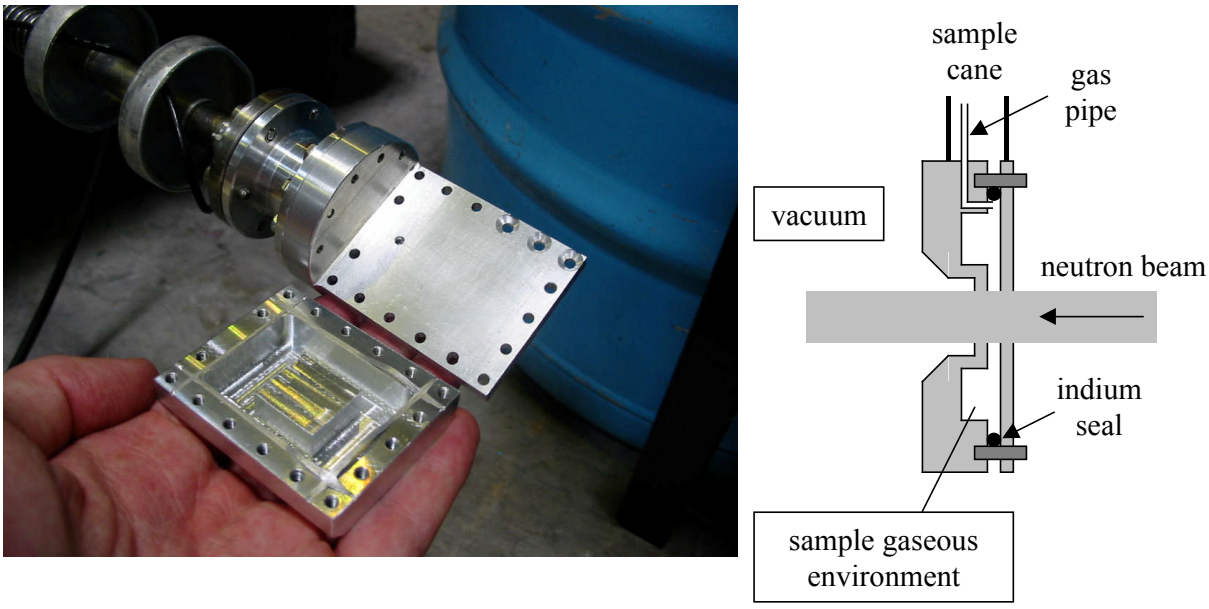

Figure 23 Left: photo of the empty IN6 sample cell, opened and mounted on a cane. Right: schematic side view of the enclosed sample cell.

The sample environment conditions were the same as the standard previously described for spectroscopic measurements. Moreover, IN6 was used to study the influence of humidity. Time-of-flight spectrometers are usually not used for samples containing water because they are sensitive to motions of gaseous molecules, occurring at the energies detected. For this reason, we needed a specifically designed cell, to minimise the volume of free gas on the path of the neutron beam, as shown on Figure 23.

- Data acquisition

All the IN6 experiments were performed at a wavelength of 0.51 nm.

First experiment (number: 8-04-287)

The sequence of experiments was as follows:

* acquisition for the empty cryostat at room temperature.
* dry silk (in vacuum) at 290 K for 300 minutes.
* dry silk at 250 K for 300 minutes.
* dry silk at 100 K for 60 minutes.
* empty can at 250 K for 175 minutes.
* empty can at 290 K for 150 minutes.

* H_2O-humid silk (humidified by storage in humid atmosphere for about 10 hours) at 290 K for 240 minutes.
* H_2O-humid silk at 250 K for 270 minutes.
* H_2O-humid silk at 100 K for 160 minutes.
* calibration sample: vanadium plate in the specific sample holder at 290 K for 140 minutes.
* D_2O-humid silk (humidified by storage in humid atmosphere for about 5 hours) at 290 K for 240 minutes.
* D_2O-humid silk at 250 K for 240 minutes.

Second experiment (number: 8-04-331)
The sample was stored in humid atmosphere saturated with D_2O for 12 hours. The sequence of experiments was as follows:

* D_2O-humid silk at 300 K for 305 minutes.
* D_2O-humid silk at 100 K for 360 minutes.
* D_2O-humid silk at 180 K for 240 minutes.
* D_2O-humid silk at 250 K for 120 minutes.
* D_2O-humid silk at 290 K for 80 minutes.
* *in-situ* dried silk for 180 minutes.
* empty can at 290 K for 240 minutes.
* empty can at 180 K for 240 minutes.
* empty can at 100 K for 109 minutes.

The sample was humidified by a short soaking in H_2O. The larger droplets were removed with a handkerchief. The sample was stored in H_2O-humid atmosphere during the acquisition of the empty can. It then was placed back in the sample cell for the next sequence:

* H_2O-humid silk at 100 K for 110 minutes.
* H_2O-humid silk at 290 K for 240 minutes.
* H_2O-humid silk at 180 K for 200 minutes.

IN16 instrument: neutron backscattering spectrometer at cold neutron source

- Instrument description

The IN16 backscattering spectrometer (Figure 24, Frick *et al.*[43]) is an "inverse geometry" instrument, which means that the incident wavelength rather the analysed wavelength is scanned during inelastic data acquisition. The shift of the incident wavelength with respect to the wavelength defined by the monochromator lattice spacing is achieved by a Doppler shift. This shift is induced mechanically by moving the crystal along its normal axis. IN16 reaches a very high energy resolution of 0.9 μeV, while the accessible energy transfer window is limited to about +/-15 μeV. The neutrons scattered by the sample are reflected on the analysers, arranged on spherical supports with a radius of 2 metres, covering an area of about 7 m^2. They then pass through the sample a second time and are detected, in the standard configuration, with 20 ^{3}He filled detector tubes (plus two small angle detector tubes not in exact backscattering geometry). The Q-range covered for spider silk experiments is of about 0.2 to 19 nm^{-1}. For the experiments described in the current thesis, the instrument was always used in this standard setup using unpolished Si(111) monochromator and analyser crystals.

IN16 is installed on a cold neutron source. All spider silk experiments were performed at an analysed wavelength of 0.627 nm using unpolished Si(111) crystals and a corresponding unpolished Si(111) monochromator.

As a special feature of IN16, diffraction detector banks are installed. These consist of a total of 320 ^{3}He single detector tubes (grouped by software to 160 pairs). They are placed at a distance of 2 meters, under the analysers in the standard setup, thus being underneath the scattering plane with an inclination angle of -24.4°. Hence, it is possible to record a 1-dimensional cross-section through the diffraction pattern of the sample simultaneously with the inelastic data.

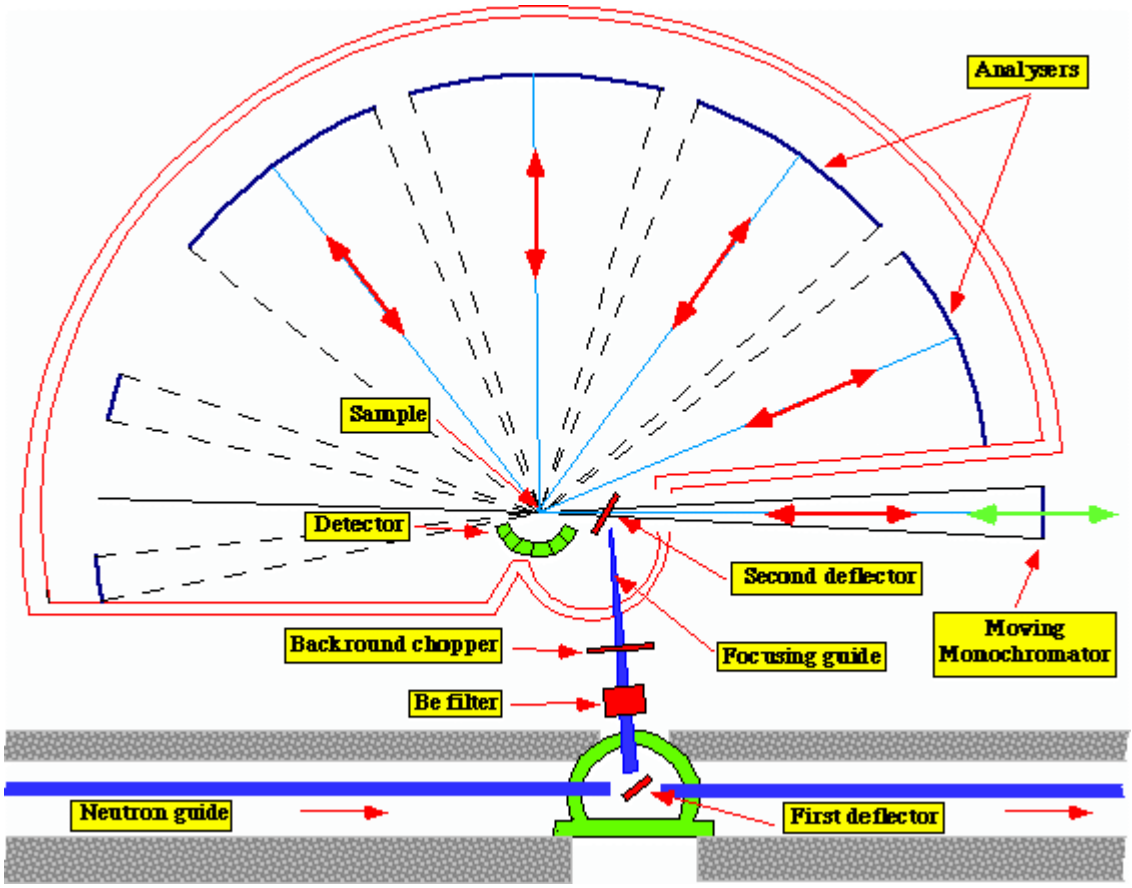

Figure 24 Sketch of the layout of IN16 (top-view). A narrow wavelength band is selected from the white beam transported through a cold neutron guide at the first deflector. The pre-monochromatic beam is deflected at the second deflector and hits the moving (Doppler) monochromator. The highly monochromatic beam subsequently travels backwards towards the sample. This is possible since the second deflector is installed on a rotating disk with alternating open and deflecting segments. With this setup, exact backscattering can be achieved on the incident side. The scattered neutrons are analysed (again at exact backscattering condition) at a fixed wavelength.

- Sample environment

The 150 mg sample was kept at normal atmospheric environment (temperature and humidity) before the acquisition. The sample was then fixed on the bottom flange of the sample cane (Figure 25). The sample environment conditions were the same as the standard previously described for spectroscopic measurements.

Figure 25 150 mg sample mounted on the bottom flange of the sample cane. During the IN16 experiments, the sample was surrounded by an aluminium hollow cylinder sealed with indium to the bottom flange. The end of the inner capillary of the cane opens into this sample volume. This heatable capillary was used for in-situ drying.

- Data acquisition

First experiment (number: 8-04-287)

The sequence of experiments was as follows:

* elastic scan of dry silk; temperature varying from 10 K to 300 K during approximately 360 minutes.
* quasielastic scans of dry silk at 100 K for 5 hours, at 250 K for 240 minutes and at 290 K for 240 minutes.
* replacement of sample by a layer of vanadium of 1 mm thickness placed on the border of the cylinder container.
* vanadium quasielastic scan at 290 K and an elastic scan while cooling down to 10 K.

The sample was then humidified by a short soaking in H_2O. The larger droplets were removed with a handkerchief. The H_2O-humid silk was then put back in the cryostat and the next sequence of experiments started:

* quasielastic scans of H_2O-humid silk for 240 minutes at 20 K, 250 K and 290 K.
* elastic scan of H_2O-humid silk from 20 K to 300 K.

* short elastic scan of H_2O-humid silk at 300 K (15 minutes, three acquisition points) while pumping on the sample environment.
* background signal of the empty can (without the sample holder) by an elastic scan from 300 K to 10 K and with a quasielastic scan of 240 minutes.

The sample was then humidified by a short soaking in D_2O. After cleaning the sample with a handkerchief it placing it into the enclosed environment on the cane as fast as possible (about 1 minute). A final scan was then performed. It was not possible to perform quasielastic measurements for silk humidified with D_2O as the end of the reactor cycle had occurred.

* elastic scan of D_2O-humid silk from 300 K to 10 K and back to 300 K.

Second experiment (number: INTER-59)
Acquisition of the vanadium callibration sample was performed. The silk was stored in D_2O atmosphere for 48 hours prior to the experiment. The sequence of experiments was as follows:

* quasielastic scans of D_2O-humid silk for 300 minutes at 250 K, 265 K and 290 K
* elastic scan of D_2O-humid silk from 290 K to 10 K
* elastic scan of D_2O-humid silk from 10 K to 290 K
* elastic scan during *in-situ* drying by pumping
* quasielastic scan of dried silk for 300 minutes at 290 K and for about 120 minutes at 265 K

Third experiment (number: 8-04-331)
For this specific experiment, and only for this one, the fibres were oriented horizontally, along the scattering plane. The silk was stored in D_2O-humid atmosphere for about 48 hours prior to the experiment. The sequence of experiments was as follows:

* quasielastic scans of D_2O-humid silk for 360 minutes at 250 K, 290 K and 20 K
* elastic scan of D_2O-humid silk from 20 K to 290 K
* elastic scan during *in-situ* drying by pumping
* quasielastic scan of dried silk for 240 minutes at 290 K

The sample was then mounted on the 2-capillaries cane and the following experiments were performed:

* elastic scan during *in-situ* hydration with H_2O at about 290 K (temperature increasing up to 300 K because of the heating of the capillaries)
* quasielastic scan of H_2O-humid silk for 300 minutes at 303 K, 265 K and 20 K
* elastic scan during *in-situ* drying by pumping at about 290 K (temperature increasing up to 300 K because of the heating of the capillaries)
* elastic scan during *in-situ* hydration with D_2O at about 300 K
* quasielastic scan of D_2O-humid silk for 300 minutes at 300 K, for 270 minutes at 260 K and for 150 minutes at 20 K
* quasielastic scan of a full cylinder of vanadium for 360 minutes at 290 K

The sample was removed, hydrated by short soaking in H_2O followed by storage in H_2O-humid environment during the acquisition of the vanadium signal, and put back in the cryostated environment. Several elastic scans were performed during *in-situ* drying by pumping. It is noted that, as already mentioned in the "General sample environment on neutron spectrometers" subchapter, the *in-situ* hydration was not satisfying as condensation occurred within the capillaries, possibly soaking the fibres. This third experiment on IN16 is mentioned for completeness but its results are not used for the analysis.

IN10 instrument: neutron backscattering spectrometer at cold neutron source

- Instrument description

No detailed description of the IN10 backscattering spectrometer is given as the principle is very similar to IN16. While having a lower flux than IN16, IN10 allows accessing a larger energy scale by using a heatable monochromator rather than a mechanical Doppler shift to scan the incident energy. The instrument is called IN10b when in this specific configuration and it allows filling the gap in energy scale between IN16 and IN6. For the current thesis, IN10b was used with the KCl(002) monochromator and unpolished Si(111) analysers corresponding to an analysed wavelength of 0.627 nm. The instrument was used with the standard detector setup using seven individual He^3 detector tubes.

- Sample environment

The sample area hosts a standard cryostat, allowing experiments at temperatures varying between 10 K and 300 K to be performed.

Prior to the experiment; the 150 mg sample was stored overnight in a H_2O-saturated humid atmosphere. It is mounted on the one-capillary cane in the same way as already described for the IN16 experiments.

- Data acquisition

The sequence of experiments was as follows:

* humid silk at 290 K, energy transfer from -5 μeV to 15 μeV
* humid silk at 90 K, energy transfer from -5 μeV to 90 μeV
* humid silk at 290 K, energy transfer from -5 μeV to 90 μeV
* realignment of the monochromator to improve the incoming flux
* humid silk at 300 K, energy transfer from -5 μeV to 45 μeV

The temperature was then set to 290 K and the sample was dried *in-situ* by pumping on the sample environment for several minutes. The monochromator was realigned before the acquisition started:

* dried silk at 290 K, energy transfer from -5 μeV to 45 μeV
* dried silk at 90 K, energy transfer from -5 μeV to 70 μeV

Synchrotron radiation scattering

X-ray microfocus beamline (ID13)

- Instrument description

The ID13 beamline is located at a low-β undulator source. A general description of the ID13 beamline has been given elsewhere[40]. Experiments are typically performed at a wavelength of 0.09765 nm. Several X-ray optical setups are available. The microbeam X-ray optics setup used in the present work is made of a focusing KB-mirror and a collimator, which defines the final beam size at the sample position. For spider silk experiments on single fibres of a few μm diameter, a typical focal spot size of 5 μm is well adapted. We used a MARCCD detector with 2048*2048 pixels of 64.45*64.45 μm^2 pixel size and 16 bit readout. The size of the X-ray converter screen was 130 mm.

- Sample environment

Single fibre experiments were usually done using a microgoniometer developed for protein crystallography (Figure 26; Top). The microgoniometer provides an easy way to match the position of a 5 μm beam with a specific position on a fibre. This is particularly interesting for local diffraction on samples consisting of several fibres. Alignment of sample and beam is facilitated by an on-axis microscope objective with a central bore for the X-ray beam. In addition the sample can be cooled to 90-100 K by a N_2 cryoflow system, which is a standard method used in protein crystallography for reducing radiation damage. Figure 26 (Bottom) shows as a typical case a single dragline silk fibre, which has been glued by fast glue to the end of a tapered glass capillary. The glass capillary is attached to the sample support, which is placed on the ϕ-rotation axis. The sample can be scanned through the beam by two orthogonal translation stages attached to the rotation axis.

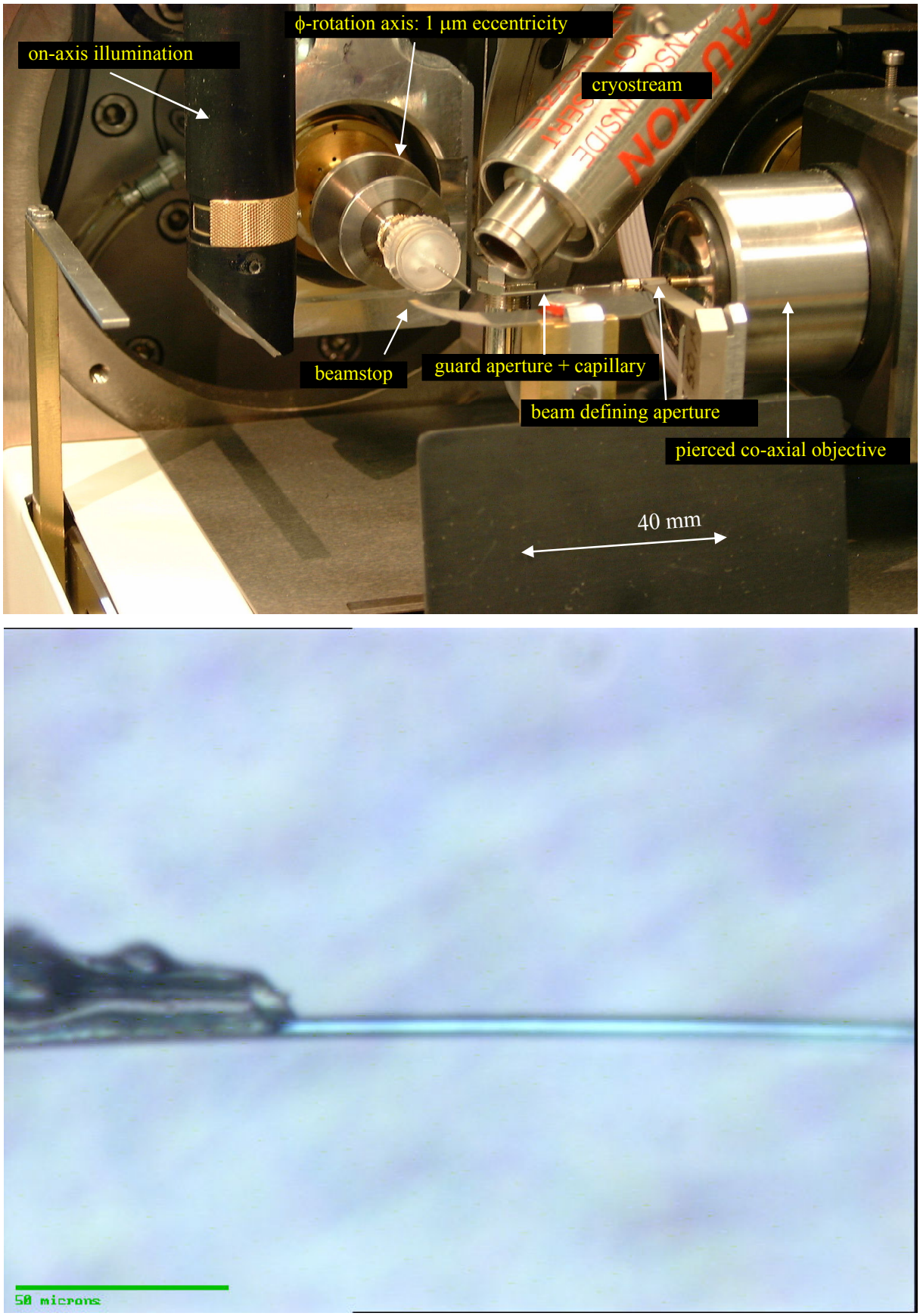

Figure 26 Top: photo of ID13 microgoniometer environment showing a sample holder on the ϕ-rotation stage. The sample is cooled by a N2 cryoflow system and observed through a c-axial objective. Bottom: microscope image of a single spider dragline fibre glued to a glass capillary placed on the goniometer head.

- Data acquisition

The data acquisition procedure was the same for all samples: 15 seconds of exposure on the fibre followed by 15 seconds of exposure slightly off the silk, for background acquisition.

Sample 1: the sample was cooled down to 95 K and two diffraction patterns were collected. The sample was then taken off and humidified by soaking the extremity of the silk during a few seconds into a water reservoir. The silk was then rapidly (about 5 sec.) put back under the cryoflow at 95 K and an acquisition was performed. The temperature was then decreased to 273 K (two acquisitions performed) and up to 293 K for drying of the silk (one acquisition).

Sample 2: the sample was humidified in the same way. Acquisitions were performed at 200 K and 250 K.

Sample 3: the sample was humidified in the same way. An acquisition was performed at 220 K.

Sample 4: the sample was hydrated in a water reservoir. Contraction of the sample sample was observed during the soaking process. The sample was then rapidly placed under the cryoflow at 100 K. Acquisitions were performed on the fibre and on an area of the fibre at the edge of the flow range where formation of crystalline ice was observed with the microscope. The temperature was then increased to 250 K (one acquisition) and to 270 K (three acquisitions).

Simulation of fibre diffraction patterns

Structural models

Several models for the 3-dimensional structure of β-polyalanine have been proposed (for a review: see Fraser et al.[23]). In this thesis, the models from Marsh et al.[44] (Marsh-model) and from Arnott et al.[17] (Arnott-model), which are based on X-ray fibre diffraction experiments, will be used.

Both models assume pseudo-orthorhombic unit cells. The setting has been chosen in this work so that the c-axis corresponds for both models to the fibre axis. The a-axis is along the hydrogen bond direction of the antiparallel β-sheets and the b-axis corresponds to the direction of the side-chain methyl groups. The c-axis parameter is defined by the repeating

motif of the alanine residues. For β-sheets this corresponds to two alanine-residues, which amounts to about 0.7 nm. The a-axis repeat of about 0.47 nm is determined by the distance between hydrogen-bonded chains. The anti-parallel chain arrangement leads to a two times larger a-axis parameter. The β-sheets are stacked along the b-axis with a distance between two sheets of about 0.53 nm. Every second β-sheet is shifted by a/2, leading to a doubling of the b-axis dimension. This chain-packing corresponds to the Marsh-model shown in Figure 27, where the unit cell has the dimensions a = 0.944 ; b = 1.06 and c = 0.695 nm and contains 8 peptide residues.

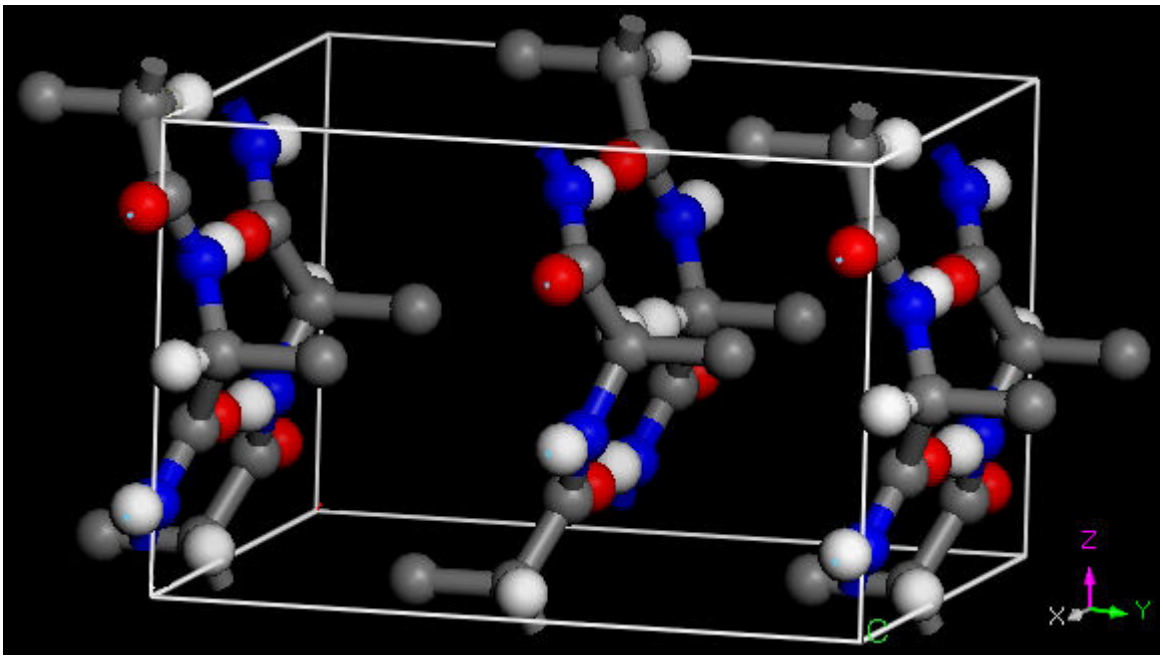

Figure 27 3-D view of a unit cell of the Marsh *et al.* model. Four of the chains shown are shared between two unit cells. Carbon atoms are in grey, nitrogen atoms in blue, oxygen atoms in red and hydrogen atoms in white. (original setting modified so that c-axis corresponds to chain axis)

The Arnott-model differs from the Marsh-model by a halving of the unit cell along the a-axis. This is based on the following assumptions: (i) the neighbouring sheets of the Marsh-model can be displaced randomly by a factor ±1/2 in the a-direction. This is reasonable as the sheet-sheet interactions are the same for either arrangement. (ii) the Arnott-model introduces an equivalent statistical structure where each chain site can be considered to contain half an up-pointing chain, and half a down-pointing chain. The direction of the hydrogen-bonded chain has always to remain opposite, to respect the antiparallel nature of the arrangement. The Arnott-model allows also a shift between the chains of neighbouring sheets along the c-axis. This is represented by a Δz variable parameter, which is the relative translation along the chain axis of the chain at (0,0) and (1/2,1/2) in the ab plane (fractional co-ordinates). When

this parameter is non-null, the symmetry of the crystal model is lowered from the space group $C222_1$ to the space group $P2_12_12_1$, which allows the observation of the (h + k)-odd reflections. Such reflections were, however, never observed by X-ray diffraction on polyalanine samples. This does not exclude a non-zero value for ΔZ, as long as it remains small enough (0.065 nm in the model) so that reflections with (h + k) odd remain too weak to be detected.

This favours the Arnott-model shown in Figure 28, where the unit cell has the dimensions a = 0.473 ; b = 1.054 and c = 0.689 nm and contains 4 peptide residues. One of the half-chains is highlighted in yellow.

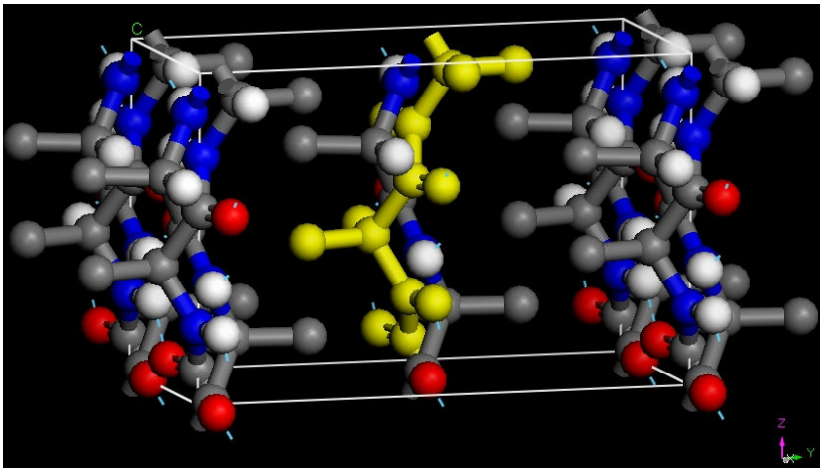

Figure 28 3-D view of a unit cell of the Arnott et al. model. Four of the chains shown are shared between four unit cells at the corners. Carbon atoms are in grey, nitrogen atoms in blue, oxygen atoms in red and hydrogen atoms in white. One of the half-chain is highlighted in yellow.

In the Marsh- and Arnott-models, the hydrogen atoms of the methyl groups are not included but will be used in the current following simulations. Although the methyl groups are free to rotate around the side chain axis, they are kept rigid for simplicity. Simulated fibre diffraction patterns were obtained with these model parameters using the Cerius[2] program.

Simulations

The effect of H/D isotopic replacement on the neutron diffraction pattern from the two crystalline models previously described is simulated with Cerius[2] program, and then compared with the experiment.

The program calculates reflection intensities from the structural model. The "fibre diffraction" pattern is then produced by applying the fibre geometry to this model (assuming free rotation around the fibre axis) and then the reflection shapes are corrected depending on the

crystallites parameters (size, orientation). These parameters were obtained from X-ray diffraction experiments on spider dragline silk[45]. For the simulated patterns shown, the crystallites size assumed are of 5 x 2 x 6 nm along a, b and c-axis. The orientation angle between the molecular chains in the crystals and the fibre axis has a value of 7° (FWHM). Note that the program does not take in account any contribution from amorphous material or incoherent scattering for background simulation.

Cerius^2 allows fibre diffraction patterns for both X-rays and neutrons to be simulated but does not permit any isotopic replacement. During the course of this thesis, the MS modelling program (*Accelerys*) -which permits isotopic replacement- became available, but simulated only powder diffraction. In order to simulate the influence of the replacement of hydrogen nuclei by deuterium on the Cerius^2 fibre diffraction pattern, carbon atoms where used instead of deuterium. The coherent scattering length of deuterium is of 6.671 barns while it is 6.6460 barns for natural carbon, which is a value almost identical with respect to the coherent scattering length of hydrogen (-3.7406 barns). Obviously, replacing an hydrogen by a carbon atom has no physical meaning, but this does not matter for simulating a pattern. For the alanine peptides, only the hydrogen atoms attached on the backbone nitrogen are assumed to be exchangeable through the soaking of the sample in D_2O.

Results and discussion: atomic scale model

La technique de diffraction neutronique des fibres est appliquée pour la première fois à la soie d'araignée. Deux clichés sont obtenus pour les fibres humidifiées avec H_2O et avec D_2O. Les deux sont dans les grandes lignes semblables aux clichés obtenus par diffraction des rayons X. Néanmoins, le cliché de la soie dont le solvant est deutéré présente une réflexion méridionale supplémentaire, jamais observée sur les clichés en rayons X, apparaissant à une position interdite par le modèle d'empilement cristallin communément admis pour décrire les cristallites de la soie. Ces modèles cristallins ne sont pas pour autant remises en cause : en effet, la caractérisation de ce pic confirme qu'il est issu d'un domaine d'une nature différente de celle des cristallites. En revanche, il correspond bien aux caractéristiques du domaine ordonné non-cristallin, de type smectique, proposé dans un modèle à trois phases (cristallites, phase ordonnée non-cristalline, matrice amorphe). L'observation de ce pic, uniquement après échange avec le deutérium, semble confirmer expérimentalement ce modèle, tout en renseignant sur l'accessibilité du domaine ordonné non-cristallin à l'échange isotopique. Par ailleurs, la comparaison des clichés expérimentaux avec des simulations de clichés pour les modèles cristallins démontre que les domaines cristallins ne sont pas ou très peu accessibles à l'échange isotopique, et donc pas non plus accessibles à l'eau.

Une expérience de microdiffraction de rayons X est effectuée sur des échantillons constitués d'une unique fibre de soie, humidifiée et gelée. La technique permet de différencier une glace cristalline, donnant des pics bien définis ou bien des anneaux fins, d'une glace amorphe donnant des anneaux diffus. Il est clairement établi que l'eau absorbée par la soie gèle dans un état amorphe. Ce résultat est d'une grande importance pour l'interprétation à venir des expériences de diffusion inélastique et quasiélastique des neutrons.

This chapter presents the experiments and results related to the atomic scale structure. This is the domain of β-sheet folding and is studied by wide-angle scattering methods. Neutron scattering data were obtained with the D19 wide-angle diffractometer and complementary synchrotron scattering experiments were performed with the ID13 beamline.

Wide-angle neutron scattering experiments on D19

Results

As already mentioned (chapter 2; Methods) 28 different angular positions are used. This allows covering a quarter of the reciprocal space, which is sufficient due to the fibre texture. All patterns obtained are merged into a composite image covering this quarter of reciprocal space, and mirroring this quarter produces the final pattern. Figure 29 shows the two neutron diffraction patterns obtained in this way for silk humidified with H_2O and D_2O. The frames visible on the patterns correspond to the borders of the detector at the different angular positions. Blank areas along the meridian correspond to blind regions in reciprocal space of a fibre, due to the curvature of the Ewald sphere (for details see chapter 2, Methods; D19 experiment). There is an important difference in the mean background intensity, of 1.6 [a.u] for the silk humidified with H_2O and of 1.2 [a.u.] for the silk humidified with D_2O. On this intensity scale, the most intense reflection intensities are of 0.2 [a.u] above the background level. The intensity scales are therefore different for the two patterns. This difference in threshold values is responsible for the apparent different shapes of the beamstop shadows. The neutron fibre diffraction patterns resemble in general to the X-ray patterns[18]. The neutron experiment was performed up to maximum Q-values of 29 nm^{-1}. This allowed some reflections of the third layer line (113 and 013, around 28 nm^{-1}) to be observed, but they appear to have a weak signal/noise ratio. For comparison, X-ray diffraction of a single fibre at room temperature allows generally to observe signal up to the fourth layer line.

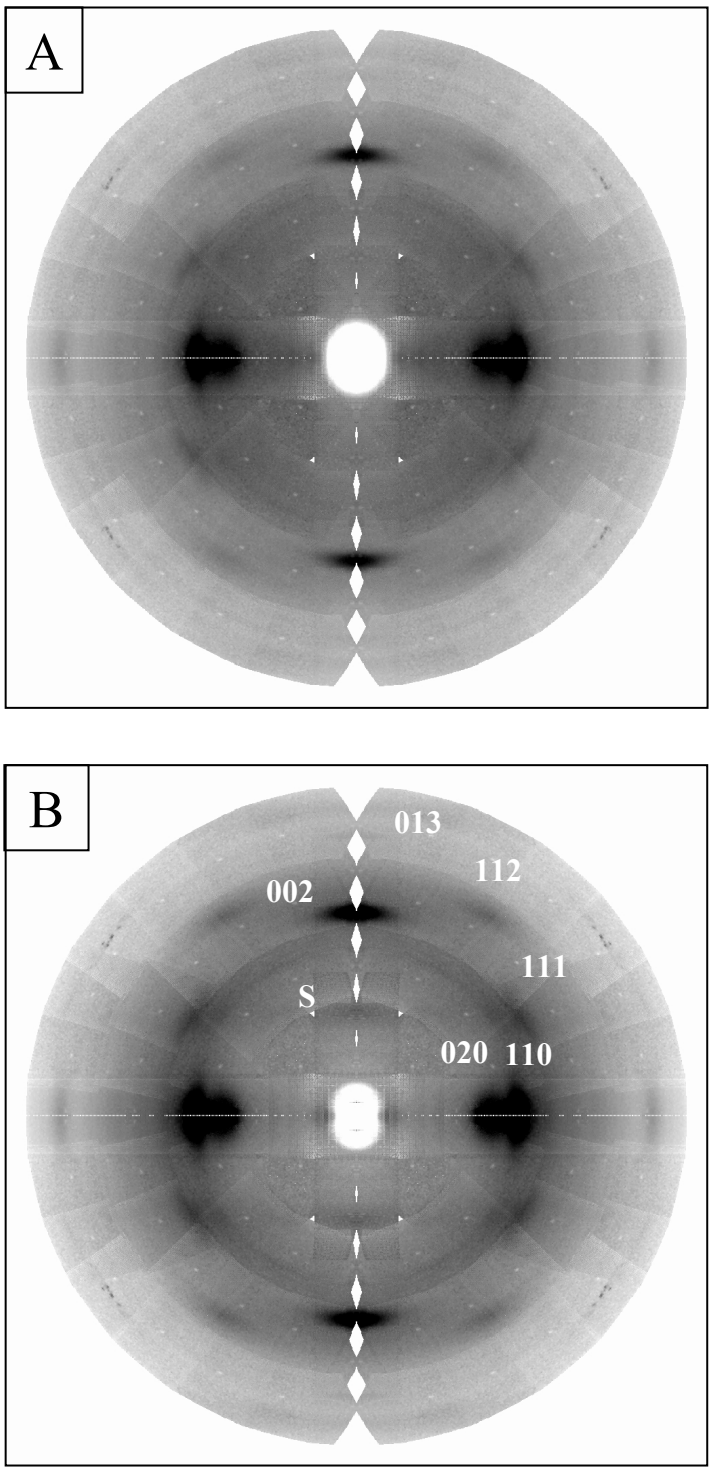

Figure 29 WANS patterns for silk humidified with H_2O (A) and D_2O (B). The image represents reciprocal mapping (see test), with Q_{min} defined by the beam stop of about 4 nm^{-1} and Q_{max} at the edge of the pattern of about 29 nm^{-1}. Indexing based on Arnott et al.[17]. D19 instrument. λ = 0.24 nm. RH : 80%. Experiments performed at room temperature.

The neutron scattering data for the D_2O-exchanged pattern show, however, a diffuse superlattice reflection (S) appearing at the position of the 001 reflection, which is not allowed for the space groups derived from X-ray data[16, 17].

Only the first experiment performed on D19 is presented. It is noted that most of the results are observed by comparing the patterns of H_2O and D_2O-humid silk. By contrast, only the D_2O-humid silk pattern was obtained in the second experiment. The pattern is then similar to Figure 29.B.

Discussion

Resolution: the main aim of the WANS experiments was to try observing intensities to higher angles than for X-ray scattering. This was expected to be possible as the neutron scattering length are constant with scattering angle while X-ray scattering form factors depend on the scattering angle. The observed WANS patterns do not show, however, an improvement of scattering at higher angles as compared to X-rays. Although the experiment was not optimised for the highest resolution, the third layer line intensities have already a poor signal/noise ratio. This suggests that internal disorder dominates both WAXS and WANS patterns.

H/D exchange: the change in background level for the H_2O and D_2O humidified samples suggests an H/D exchange in the samples although it does not provide information on the exchange on a microscopic level. We will therefore simulate in this paragraph the influence of H/D exchange on the WANS patterns. This will be done for the two existing atomic models of β-poly(L-alanine) from Marsh et al.[16] and Arnott et al.[17] (see chapter 2, Methods). The patterns are simulated with the Cerius^2 program (for details: see chapter 2). Such simulations are evidently restricted to the crystalline fraction. The H/D exchange in the simulations will be limited to the exchangeable atoms corresponding to the N-H/D bonds.

Simulated patterns for hydrogen-exchanged polyalanine (Abbr.: H-polyalanine) and deuterium-exchanged polyalanine (Abbr.: D-polyalanine) are shown in Figure 30. The simulated patterns resemble experiment SR-diffraction[18] and the neutron diffraction pattern (Figure 29) but suggest a much higher crystallinity as the inherent rotational disorder of the hydrogen atoms was not taken into account. We will therefore only consider the equatorial *hk*0 reflections, which are not affected by this c-axis rotational disorder. The calculated intensities of the strongest equatorial reflections are listed in Table 3.

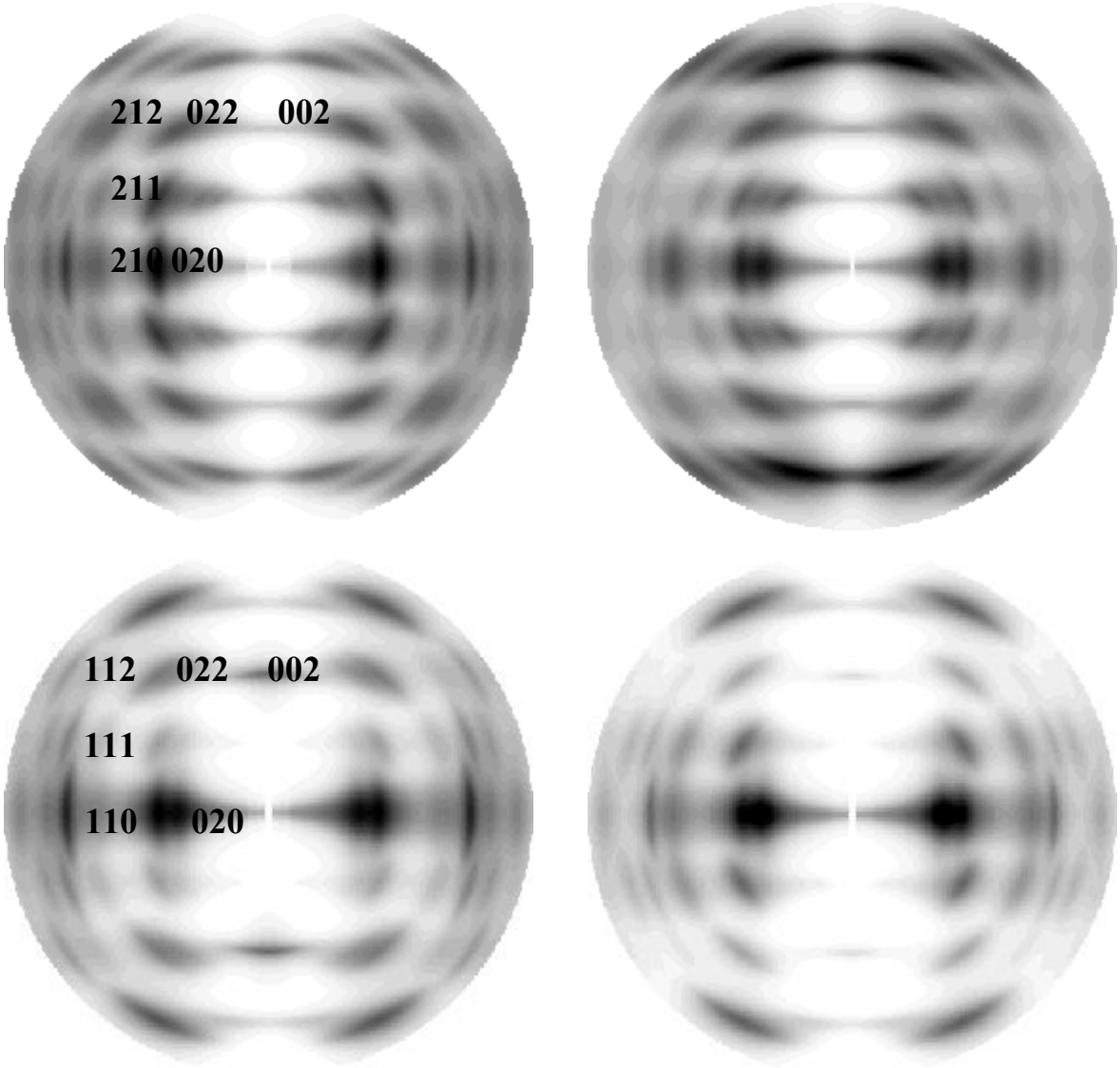

Figure 30 Simulated neutron fibre diffraction patterns. Top: Marsh et al.[16] and bottom: Arnott et al.[17] showing selected indices according to the corresponding unit cells. Left: H-polyalanine; right: D-polyalanine. Both patterns are on a logarithmic intensity scale. The different indices are due to a halving of the unit cell in the Arnott et al. model.

Table 3 calculated neutron scattering intensities (arbitrary units) of equatorial reflections from H- and D-polyalanine crystal models.

	Marsh et al.[16] H-polyalanine	Marsh et al. D-polyalanine	Arnott et al.[17] H-polyalanine	Arnott et al. D-polyalanine
I_{020}	930	4330	3250	6640
I_{210} (Marsh) I_{110} (Arnott)	3553	2180	3080	2580

A comparison of the two models will be based on the ratio of integrated intensities of equatorial reflections $R = I_{110}/I_{020}$.

* Marsh et al. H-polyalanine: R = 3.8 D-polyalanine: R = 0.5.
* Arnott et al. H-polyalanine: R = 0.95 D-polyalanine: R = 0.39

Experimentally determined values from the neutron diffraction patterns give R = 1.1 for silk humidified with H_2O and R = 1.2 for silk humidified with D_2O, which are practically identical, given the uncertainty in background subtraction due to the presence of amorphous material. This is a completely different behaviour as compared to the very strong influence of H/D exchange predicted by the simulations.

The conclusion is therefore that the crystalline polyalanine fraction in silk shows only a negligible H/D exchange. This result on the accessibly of the crystalline fraction to the H/D exchange in silk will become important for the interpretation of neutron data where an H/D exchange is expected. This is for instance the case for the neutron spectroscopy measurements, which are focused on the amorphous fraction. It also gives an argument on the next paragraph's discussion on the nature of the diffuse reflection (S) observed in the D_2O-humidified silk pattern.

Superlattice reflection:

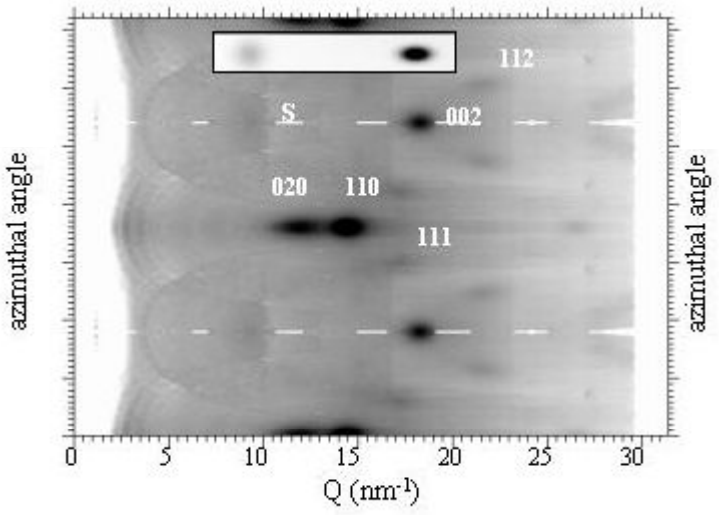

Figure 31 Cake-regrouped neutron fibre diffraction pattern of D_2O-humidified silk. The inset shows the 2D-Gaussian profiles of the simulated 002 reflection and the superlattice peak (S). Indexing based on Arnott et al.[17]. D19 instrument. λ = 0.24 nm. RH : 80%. Room temperature.

For quantitative analysis, the superlattice reflection (S in Figure 29.B) and the 002 reflection were fitted using 2D Gaussian profiles and a first-order polynomial background (Figure 31). The azimuthal width of the superlattice reflection derived from the fit is of 36.2° fwhm. This is significantly larger than for the 002 reflection (16.8° fwhm). The azimuthal width of the meridional 00*l* (or *hk*0) reflections can be related to an axial orientation distribution of crystalline domains[18, 45]. This does, however, not provide an explanation for the enlarged azimuthal width of the superlattice peak. A possible explanation would be crystal defects[46] resulting in a breakdown of the $l = 2n$ extinction. This is however very unlikely as it has never been observed by SR diffraction experiments on a range of dragline silk[20, 47]. For the same reason, the presence of the superlattice peak is difficult to reconcile with a different space group or a superstructure due to a repetitive sequence of other residues, such as serine residues in silk MA-spidroins [23, 44, 48]. The assumption of more or less random distribution of β-sheet nuclei[49] in the amorphous matrix is furthermore incompatible with the meridional position of the S reflection. The azimuthal width of the superlattice reflection corresponds, however, to the broadening of the oriented equatorial halo due to short-range order as seen by WAXS, which can be separated from the 210 reflection by profile fits[20, 45]. Dragline protein chain-folding models suggest an aggregation of alanine sequences through a backfolding of β-strands via serine-glycine of glycine-asparagine "hairpin loops"[14, 49-51]. It is therefore tentatively assumed that the glycine-rich chains, which do not participate in the formation of a polyalanine block, are constrained into a smectic β-sheet structure, which is laterally disordered due to a mismatch of side groups. A larger orientation distribution of chain axes in the smectic phase would explain the increased azimuthal width of the superlattice reflection as compared to the crystalline domains 002 reflection.

The 0.7 nm superlattice reflection corresponds therefore for a smectic model to the repeating chain unit in the short-range order domains. According to this model, the fact that the S reflection is visible only for the D_2O-humidified silk illustrates that the short-range order domain is accessible to water or at least to H/D exchange through hydrogen atoms diffusion.

The presence of nanofibrillar objects composed of crystalline domains separated by short-range order domains, and their accessibility to water and H/D exchange is discussed from SANS experiments in the next chapter.

Low temperature X-ray diffraction on water absorbed by silk fibres

SR scattering experiments on wet nascent silk during spinning suggests a homogeneous distribution of water in the amorphous network[52]. A number of neutron scattering experiments, in particular QNS-experiments, were, however, performed at cryogenic temperatures and it was therefore necessary to investigate the low temperature structure of water absorbed in the fibres.

The SR microdiffraction experiments were performed on single fibres at the ESRF-ID13 beamline. Silk fibres were soaked prior to the experiment in water and then rapidly cryofrozen at 100 K in a N_2 cryostream. An image of the fibre investigated is shown in Figure 32.A and the corresponding diffraction pattern in Figure 32.B.

Soaking with water is known to result in a shrinking of the fibre, which is also called supercontraction[53]. It has been shown that the orientation of the crystalline domains along the fibre is strongly reduced upon supercontraction[53-55]. The current data confirm this loss in orientation for the low temperature soaked fibre as the azimuthal broadening of the equatorial peaks has broadened. (Figure 32.B; compare with Figure 33.B) We also note that there is no evidence for crystallised ice, which suggest that the cryofrozen water is in an amorphous state. A weak powder ring with a d-spacing of about 0.76 nm is attributed to this amorphous ice as it cannot be attributed to the silk reflections.

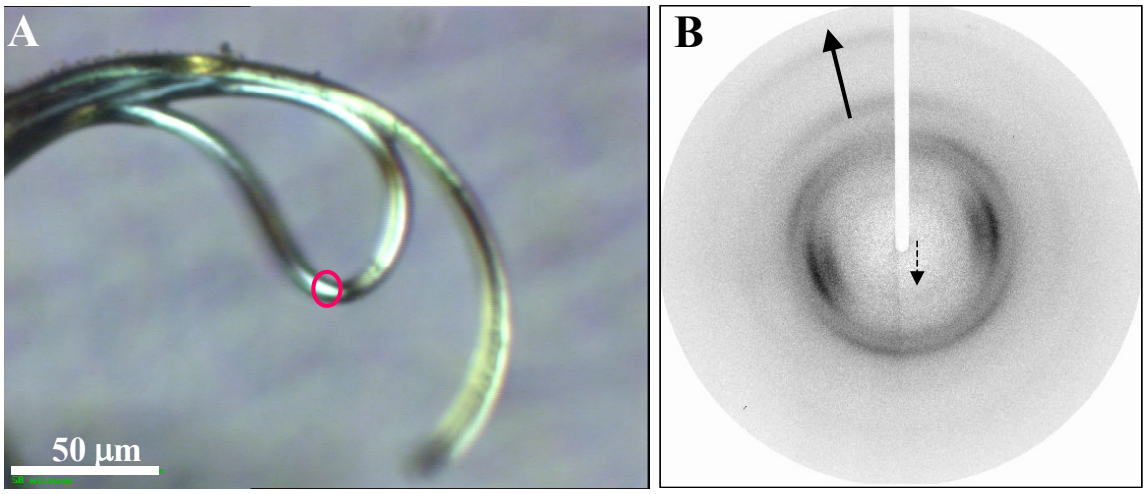

Figure 32 A: Spider dragline silk, soaked in water and then frozen under a cryostream nitrogen flow at 100 K. The red circle represents the point of acquisition. B: corresponding diffraction pattern. The large arrow indicates the fibre axis; the small arrow point to a powder ring attributed to amorphous ice. Note that the fibre axis is not exactly orthogonal to the beam direction.

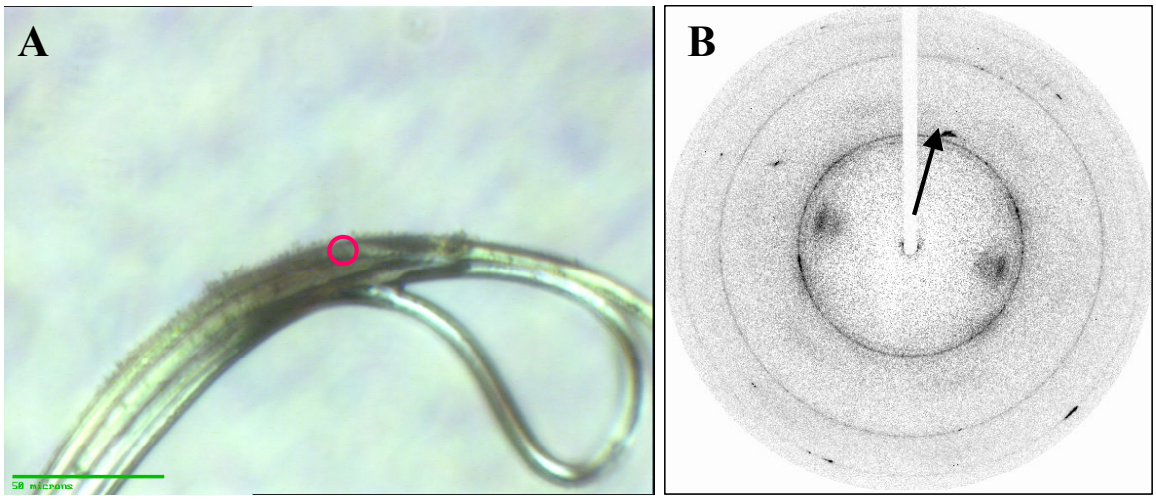

Figure 33 A: Ice crystallized at the edge of the cryoflow on the fibre. The red circle represents the point of acquisition. B: corresponding diffraction pattern showing an overlap of dragline silk reflections and ice powder rings. Some spots are due to larger ice crystallites. The arrow indicates the fibre axis.

Figure 33.A shows a different part of the sample with small ice crystallites. Ice formation is often seen for cryoflow systems at the edge of the cold zone, which is only a few mm wide. In the present case this ice could come from air humidity or from inside the water-soaked fibre. The corresponding diffraction pattern shows the powder reflections of small, randomly oriented ice crystallites and some spots due to larger ice crystallites. As the azimuthal width of the equatorial reflections corresponds again to air-dry silk it is probable that at least part of the crystalline ice in Figure 33.B has come from inside the fibre after melting of the amorphous ice. It is also interesting to note that the powder rings are rather narrow and not grainy, which could be due to the highly dispersed state of water in the amorphous network.

We conclude therefore that water absorbed by the silk fibres is in an amorphous state at low temperatures, which is of particular interest for the discussion of the low temperature QNS spectra in the following chapter.

Results and discussion: supramolecular structure

Les expériences, antérieures au projet, de diffusion de rayons X aux petits angles par la soie d'araignée montrent essentiellement deux contributions, une réflexion méridionale et une traînée équatoriale, observées et caractérisées en détails dans des travaux précédents. Dans le modèle à trois phases, la réflexion méridionale est attribuée à la succession des domaines cristallins et des domaines ordonnés non-cristallins au sein d'une nanofibrille, tandis que la traînée équatoriale contient des informations structurales sur les nanofibrilles au sein de la matrice amorphe. Ces contributions sont ici observées au cours d'expériences de diffusion de neutrons aux petits angles. Les intensités des contributions évoluent pour les fibres humidifiées sous divers taux d'échanges H/D, ainsi que pour les fibres séchées à partir des taux d'échange correspondants. La cinématique de l'opération de séchage du paquet de fibres peut être mesurée via l'évolution de l'intensité du pic méridional en fonction du temps d'exposition à un flux d'air sec. De même, en se plaçant dans une situation où l'évolution du pic est liée à l'échange H/D, la cinématique de cet échange H/D est mesurée, et au moins un phénomène d'échange rapide (avec un temps caractéristique de l'ordre de 6.5 minutes) est mis en évidence. L'évolution de l'intensité du pic méridional est expliquée par un échange H/D au sein des domaines ordonnés non-cristallins, via l'eau qu'ils contiennent mais affectant aussi les atomes d'hydrogène labiles des chaînes de polymère dans ces domaines, tandis que les domaines cristallins demeurent seulement hydrogéné quel que soit le taux d'échange du solvant, d'où évolution du contraste entre les deux domaines. L'évolution de l'intensité de la traînée équatoriale est en revanche expliquée par l'effet de l'eau essentiellement, qui pénètre plus facilement la matrice amorphe par opposition aux nanofibrilles riche en domaines cristallins, la densité moyenne de la nanofibrille intervenant désormais dans le calcul de contraste.

Une expérience supplémentaire a permis d'obtenir des données de qualité à très petits angles. Les résultats confirment les analyses en diffusion des rayons X aux petits angles et permettent d'affiner les estimations des dimensions des nanofibrilles, en mesurant une longueur axiale moyenne de l'ordre de 170 nanomètres.

WANS data discussed in Chapter 3 suggest that the crystalline polyalanine fraction is not affected by H/D exchange. It is, however, well known that the amorphous fraction absorbs water as the mechanical properties[9] are affected and the crystalline domains disorder upon hydration[56]. It was therefore of interest to study the influence of the H/D exchange on the supramolecular structure using the D11 and D22 small-angle scattering camera.

Small Angle Neutron Scattering: D11 experiment

Results

Six D_2O/H_2O ratios are chosen for hydrating the silk (see Figure 34). The percentages indicated in the figure correspond to D_2O content : 0% corresponds to pure H_2O and 100% corresponds to pure D_2O. After 80 minutes of hydration, the silk was dried by a constant flow of dry air during 80 minutes. The patterns obtained for humidified and dried silk are shown on Figure 34.

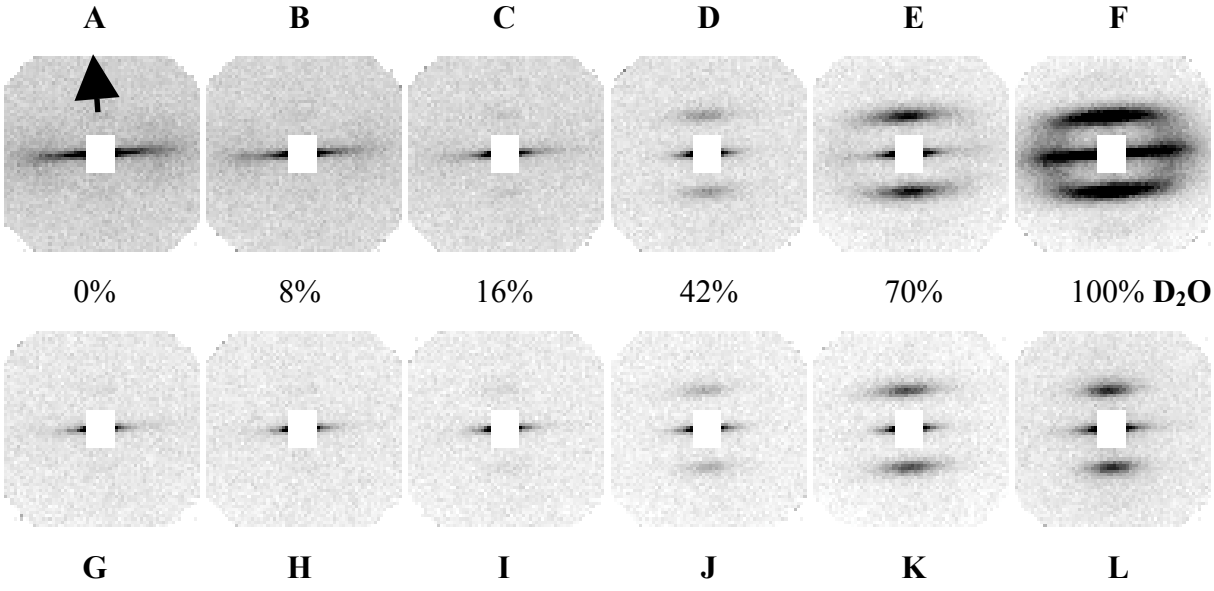

Figure 34 Influence of H/D ratio of hydration water on SANS patterns of humidified silk (top) and dried silk (bottom). D11 instrument, λ = 6 Å, Q_{min} = 0.4 nm^{-1} and Q_{max} = 2.1 nm^{-1}. The patterns were corrected for absolute intensities (air scattering background subtracted, correction for transmission). The same linear intensity scale is used for all patterns. The arrow indicates the fibre axis.

The SANS pattern of the completely deuterated silk corresponds to SAXS results[21, 57, 58] showing a meridional peak and an equatorial streak. The meridional peak positions with d=7.2 nm for dry silk and d=7.6 for humid silk agree with these studies. The intensities of the SANS patterns increase with hydration, as already observed by SAXS. For both humid and

dried silk at constant H/D exchange, the profiles of this peak show the same radial width, which suggest that no significant changes occur during hydration, in agreement with the WANS experiment (chapter 3). A novel feature of SANS is, however, that the meridional peak -observed for deuterated silk- is practically extinguished for dry and humid hydrogenated silk. The equatorial streak intensity of humid silk is also seen to vary with the H/D ratio, but in a different way as it reaches a minimum in intensity for a different H/D value than the meridional peak. The influence of the H/D content for dried silk seems to follow the same evolution.

Discussion

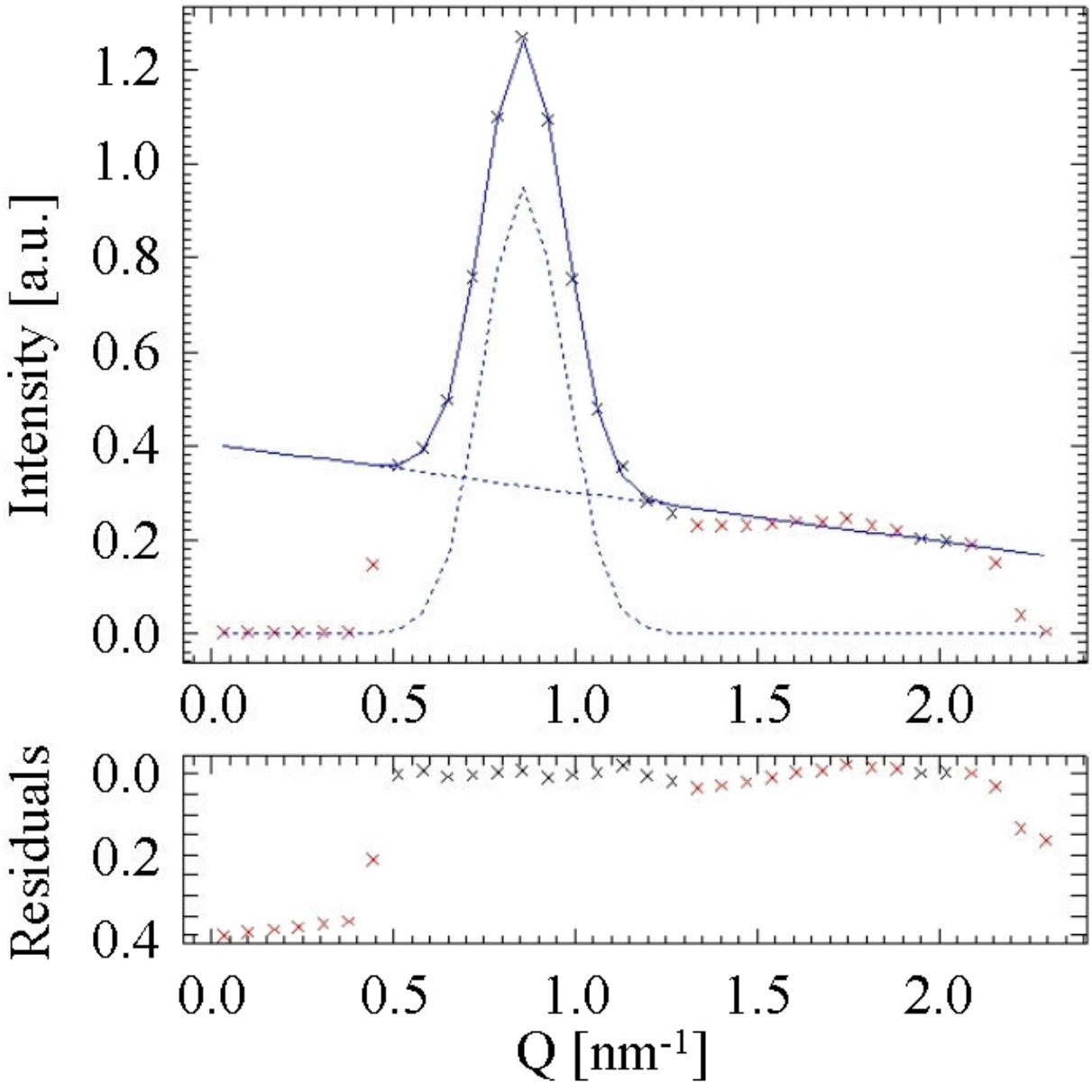

Figure 35 Fit of the meridional SANS peak profile from silk humidified with pure D_2O.

Kinetics of the drying process: the pattern of humid silk, 100% D_2O, prior to drying is shown in Figure 34.F. The silk was then dried under an air flow (see above) during 140 minutes, while SANS patterns were constantly recorded with 20-minute time steps. The last pattern obtained is shown in Figure 34, L. For modelling of the meridional SANS peak profile, a single Gaussian function and a first-order polynomial background were used (Figure 35). The drying results in a loss of intensity of the meridional peak (Figure 36). The time dependence of the intensity change time allows the kinetics of the drying process to be determined.

The intensity decay can be fitted by a first-order exponential decay with a decay constant of τ=31.8 minutes. During the D11 experiment, the typical time spent on drying the fibre for the other H/D ratios were of 60 minutes, followed by a 20 minutes acquisition time (shadowed area on Figure 36).

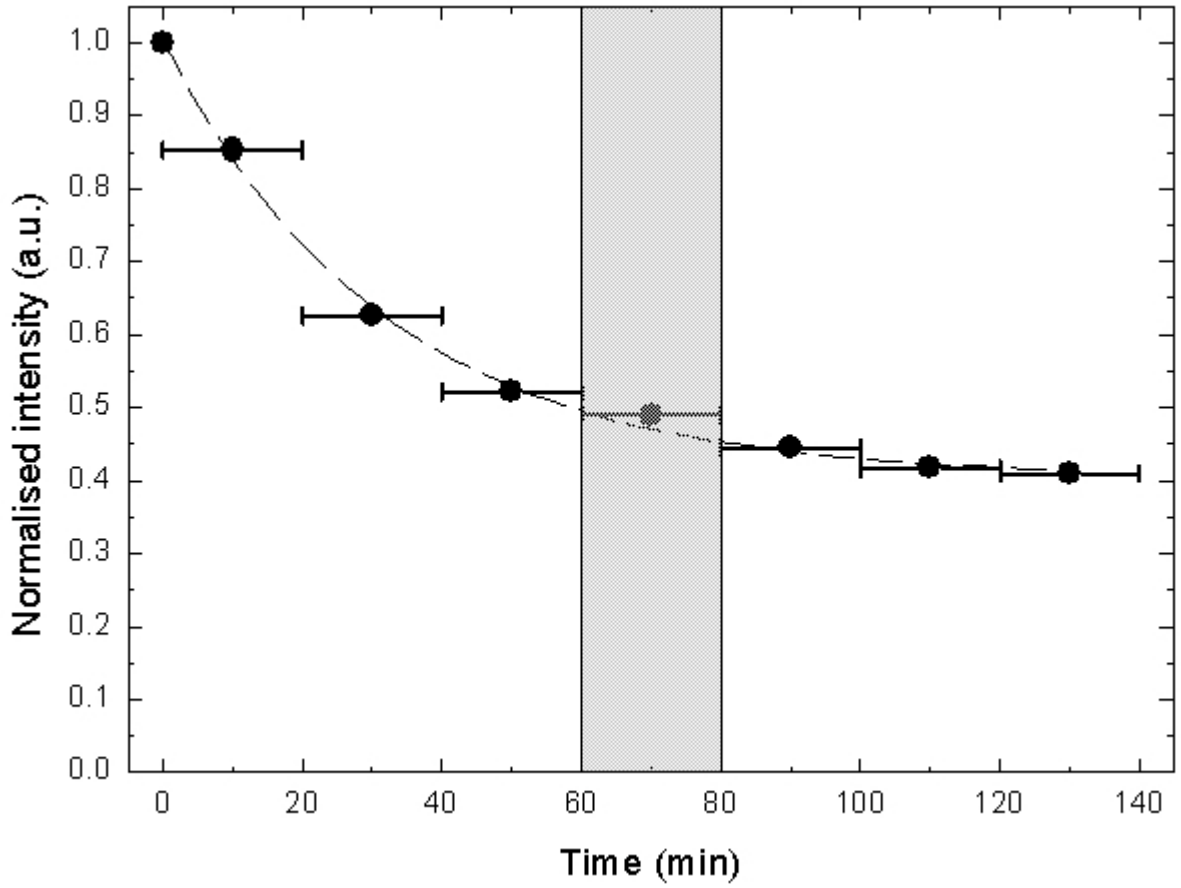

Figure 36 Variation of the integrated meridional peak intensity during the drying of silk humidified with 100% D_2O. The dashed line corresponds to the fit by an exponential decay with a non-null offset. The shadowed area (60 to 80 minutes) corresponds to the time-window during which "dried silk" patterns shown on Figure 34.(G to L) are obtained.

According to this measurement of the kinetics of drying, there is still during this time a small evolution of the humidity level in the silk. The so-called "dried silk" contains therefore

residual water content of an unknown absolute value. The drying process was, however, always the same for each H/D ratio with respect to the initial hydration state of the sample (see next subchapter). It is therefore reasonable to assume that this value of water content is approximately reproduced for each acquisition on dried silk at the different H/D ratios.

Kinetics of the H/D exchange: Before measuring the H/D exchange kinetics, the sample was extensively humidified with D_2O-humid gas for a day and then dried with dry air during 140 minutes. The pattern prior to H/D exchange is shown in Figure 37.A. The silk was then humidified with H_2O-humid gas, while acquiring the data during 80 minutes with 20-minute steps. The last pattern (Figure 37, E) corresponds to silk humidified with pure H_2O.

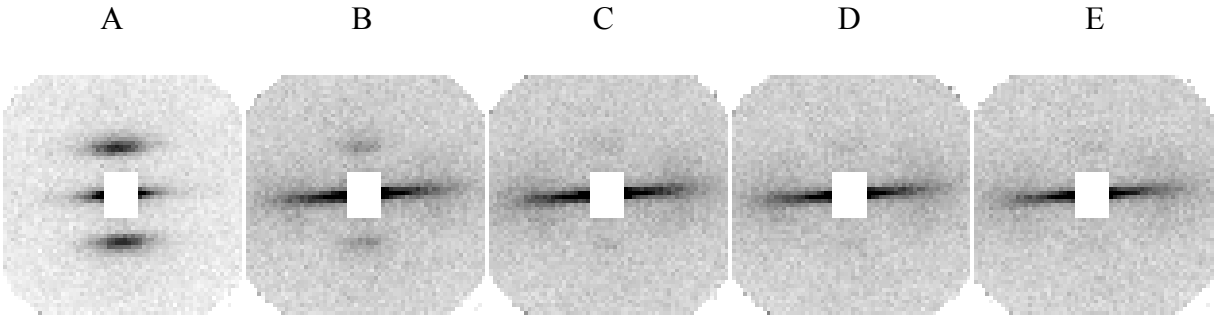

Figure 37 SANS patterns of dried silk containing deuterium during hydration with H_2O. Pattern A corresponds to silk previously humidified with pure D_2O for a day, then dried with dry air during 140 minutes. The next patterns (B-E) correspond to continuous acquisition over 20 minutes while the silk is under a constant flow of H_2O-humid gas. D11 instrument, λ = 6 Å, Q_{min} = 0.4 nm^{-1} and Q_{max} = 2.1 nm^{-1}. Absolute intensities. Same linear intensity scale for all patterns.

As indicated earlier, the hydration increases the intensity of the small-angle pattern. The opposite effect is however observed during hydration with H_2O of a deuterated sample. This must be therefore due to the replacement of the exchangeable deuterium atoms in the dried silk by hydrogen atoms. The evolution of the integrated intensity deduced from the fit of the meridional peak (Figure 38) with increasing H/D exchange allows determining the H/D exchange kinetics. The intensity decay can be fitted by a first-order exponential decay with a decay constant of τ = 6.5 minutes. The same experiments performed with different H/D ratio (from 0% dried silk to 8% humid silk, from 8% to 16%, from 16% to 42% and from 42% to 70%) give a similar value.

Patterns for humid silk shown in Figure 34 (A to F) are all obtained after at least one hour of constant humid flow, and correspond to 20 minutes of acquisition time. According to the plot in Figure 38, both the humidity state and H/D exchange state are at the equilibrium for this

period, after this hour of hydration. One cannot exclude however that a further, slower H/D exchange process occurs.

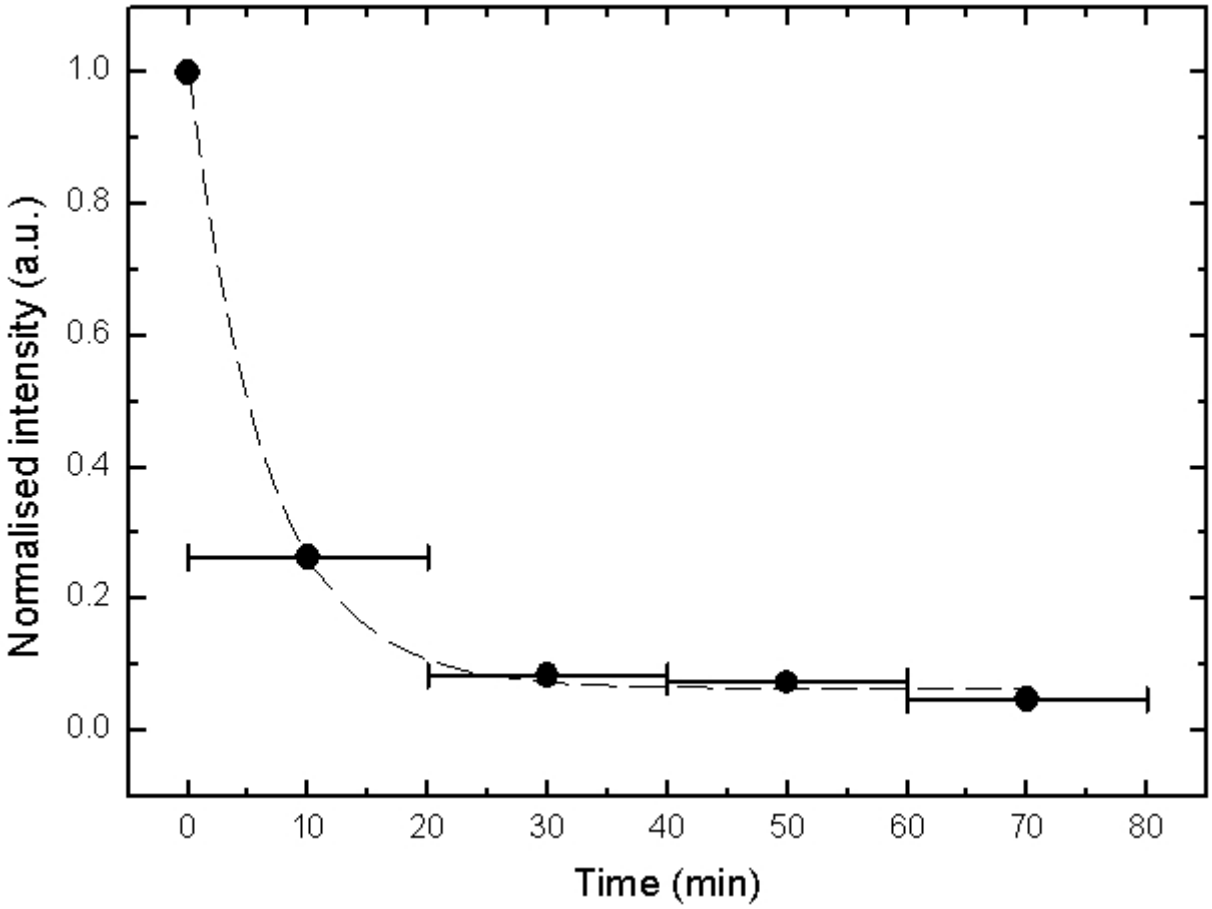

Figure 38 Kinetics of H/D exchange from the variation of the integrated meridional peak intensity. The dash line corresponds to the fit by an exponential decay with a non-null offset.

Analysis of the evolution with H/D exchange: the evolution of the meridional and equatorial intensities are shown in Figure 39. The meridional intensity is as previously indicated obtained by modelling the meridional peak profile with a single Gaussian function and a first-order polynomial background (Figure 35). The equatorial intensity was obtained by summing all counts in the equatorial band. The variation of both meridional peak (circles) and equatorial streak (squares) intensities as a function of the D_2O content of the solvent are shown in Figure 39 for both humid (full symbols) and dried silk (open symbols).

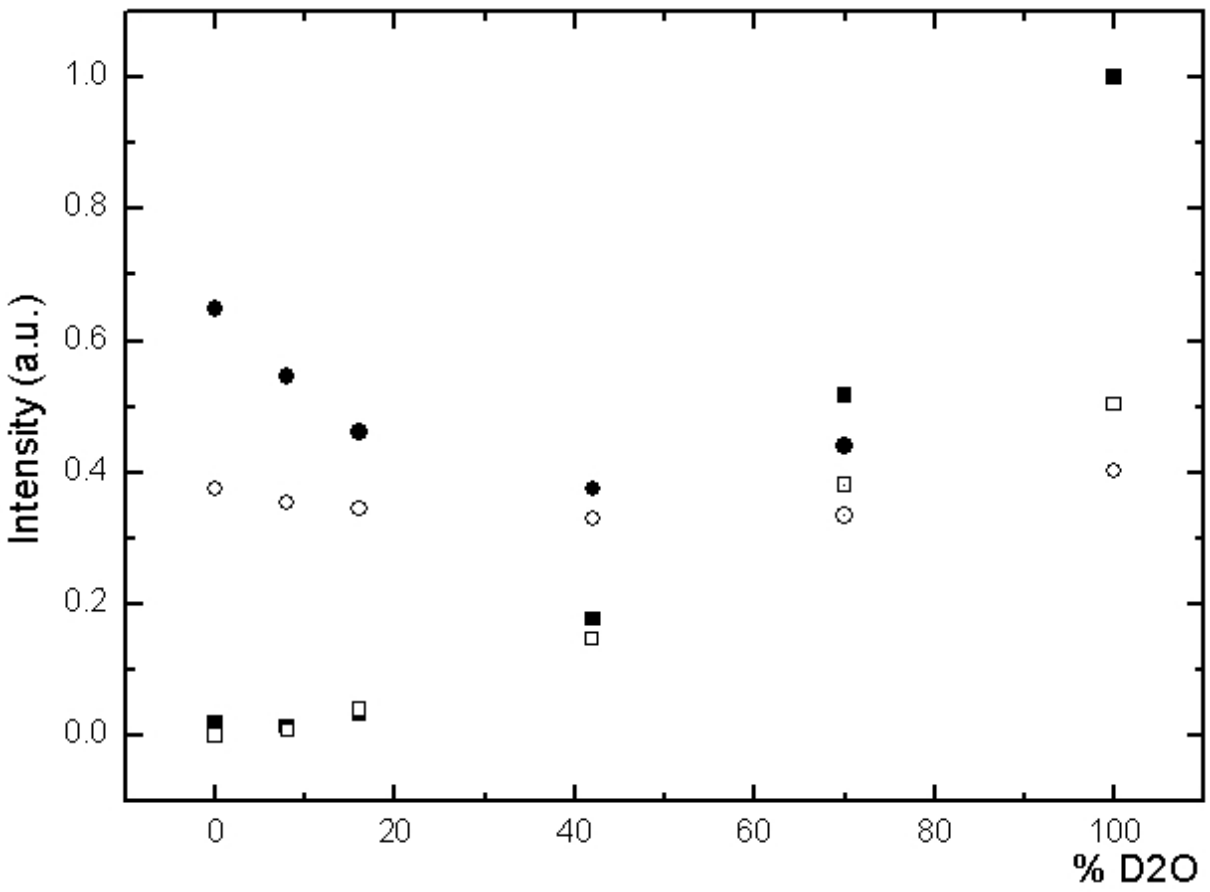

Figure 39 Integrated equatorial streak (squares) and integrated meridional peak (circles) as a function of the D_2O content of the solvent for humid silk (full symbols) and dried silk (open symbols). Equatorial intensities and meridional intensities are normalised to the respective most intense point, corresponding in both cases to the silk humidified with pure D_2O.

The meridional "long period" peak can be attributed to a sequence of crystalline (alanine-rich) and short-range order (glycine-rich) domains in the nanofibrils[21, 50, 57]. The intensity is given in the SANS case by

$$I(Q) = k\Delta_{sld}{}^2 |P_c(Q)| Z(Q) \quad (1)$$

where k is a normalisation constant, $\Delta_{sld} = \overline{C}_{sld} - \overline{A}_{sld}$ is the mean scattering length density difference between crystalline and short-range order domains, P_c is the form factor of a crystalline domain, and $Z(Q)$ is the Laue interference function[59]. At constant hydration level, the variation of meridional intensity with H/D ratio of the solvent depends principally on the variation of the scattering length term. An H/D exchange on the chains will affect practically only the polyglycine N-H group in the short-range order domains, which are accessible to solvent molecules. Such an exchange on the chains of the short-range order domains is also suggested by the meridional superlattice peak which is only observed for the D_2O-exchanged material (see chapter 3, "evidence for a smectic order").

The total scattering lengths of H-alanine (1.645 x 10^{-12} cm/molecule) and H-glycine (1.728 x 10^{-12} cm/molecule) are similar, which results in a virtual extinction of the meridional peak for H_2O as solvent[60]. The exchange to D-glycine (2.769 x 10^{-12} cm/molecule) introduces a Δ_{sld} increase, which shows up in an increase of the meridional peak intensity.
Including one water molecule with the glycine residues in the short-range order domain would change the total scattering length of H-glycine-H_2O to 1.56 x 10^{-12} cm/molecule and of D-glycine-D_2O to 4.684 x 10^{-12} cm/molecule. A fraction of water entering the short-range order domains is suggested by the dependence of the lamellar spacing on the hydration state[57, 58].
Thus, the effect on the meridional peak intensity observed on Figure 39 is explained by the H/D exchange influence, including the exchange on the chains. This last point explains that the effect remains strong for dried silk.

The intensity of the equatorial streak is proportional to the product of the nanofibrils form factor $P_n(Q)$ and the contrast $\Delta\rho^*$ due to the scattering length density difference between nanofibrils and surrounding random matrix:

$$I(Q) = k' P_n(Q) \Delta\rho^* \tag{2}$$

This has been discussed in more detail for SAXS data for cellulose nanofibrils in flax[61]. Water molecules entering the more or less dry random silk matrix will reduce its density and hence increase the $\Delta\rho^*$ term, which is readily observed for *in-situ* SAXS experiments[21, 58]. For SANS, the H/D exchange will affect $\Delta\rho^*$ through the variation of the scattering length density of the nanofibrils and of the solvent in the matrix. Figure 39 shows that the equatorial streak reaches a minimum, for both humid and dried silk, at about 40% D_2O, which corresponds roughly to the match point for proteins[60]. The match point of the exchangeable glycine is at about 50% D_2O while the match point for H-alanine is at about 30% D_2O. The observed minimum therefore corresponds to a compromise between the exchangeable and the non-exchangeable fractions.
Thus, the effect on the equatorial streak intensity is mainly explained as an effect of water absorption, and therefore is strongly visible only for humid silk.

Small Angle Neutron Scattering : D22 experiment

Results

The D22 camera was only available for a short period and was used for studying the SANS pattern over a wider Q-range from 0.02 nm^{-1} to 3.5 nm^{-1} than available on D11. The large range required experiments at three different detector distances. Figure 40 shows the three patterns obtained for each detector distances for the 150 mg sample.

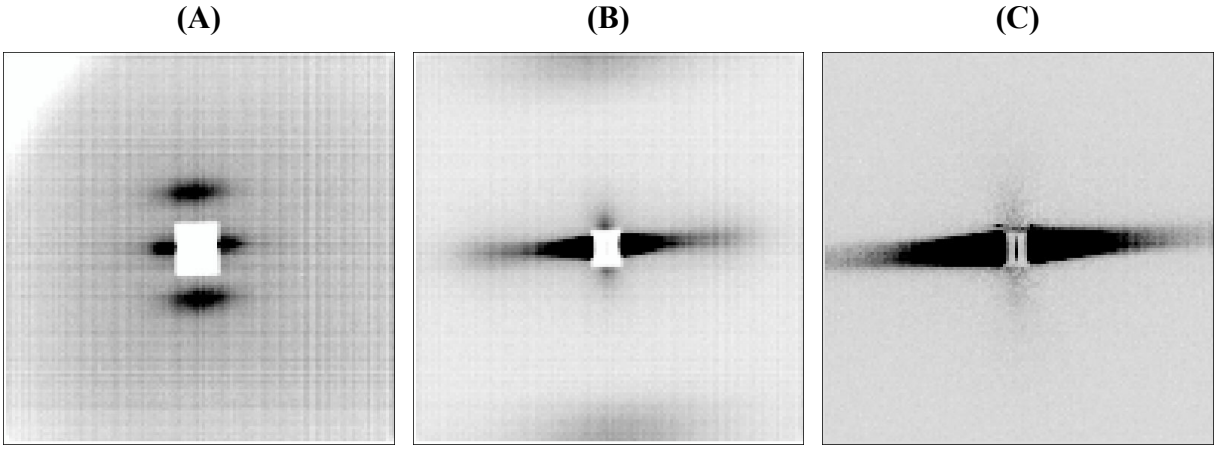

Figure 40 SANS patterns of 150 mg of spider dragline silk at atmosphere humidity and temperature. A: detector distance of 1.4 m, Q_{min} = 0.2 nm^{-1} and Q_{max} = 3.5 nm^{-1}. B: detector distance of 6 m, Q_{min} = 0.08 nm^{-1} and Q_{max} = 1 nm^{-1}. C: detector distance of 17 m, Q_{min} = 0.02 nm^{-1} and Q_{max} = 0.3 nm^{-1}. D22 instrument. λ = 0.6 nm. Different linear intensity scales are used for each pattern.

The meridional peak and the equatorial streak previously described for the D11 camera results are visible. As the data extend to small Q-values, the equatorial streak can, however, be analysed in more details.

Discussion

Nanofibrillar dimension: a detailed analysis of the equatorial streak recorded by SAXS in terms of orientation and dimensions of nanofibrillar objects has already been reported[57]. The SANS data obtained on D22 support this analysis. The broadening of the equatorial streak was determined at selected Q values parallel to the meridional axis by fitting Gaussian functions to the peak profiles (Figure 41).

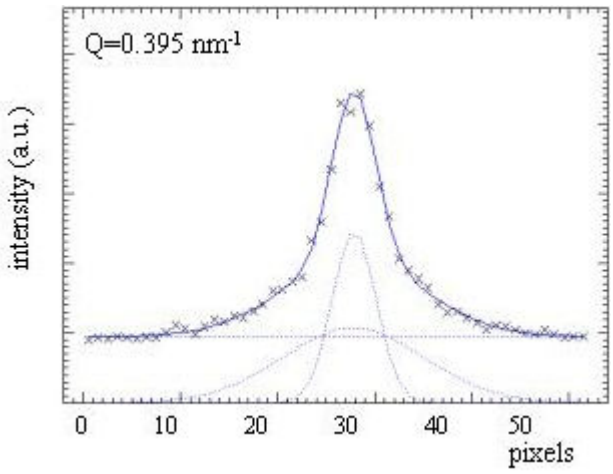

Figure 41 Broadening of the equatorial streak t Q = 0.395 nm^{-1}. Crosses correspond to the experiment data and solid lines to the fits. At this Q value, a broad and a narrow peak are necessary to fit the data.

The data obtained for the smallest Q-values available (detector distance of 17 m) show that a single Gaussian function allows fitting the equatorial streak up to about Q ≈ 0.26 nm^{-1} while the width of the streak is decreasing to a constant value of about 8° fwhm. At larger Q values, a second broader Gaussian function of about 26° fwhm is required to model the streak (Figure 42). The data at the 5 m detector position confirm these two peaks and allow extending the fits to larger Q values.

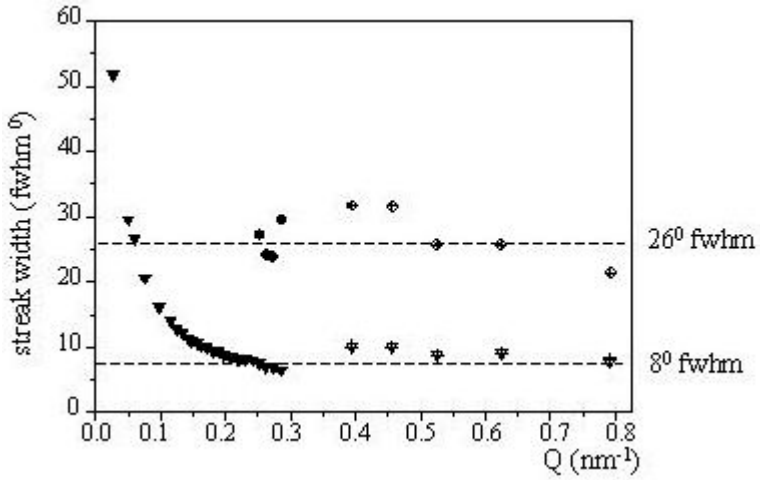

Figure 42 Angular width of equatorial streak as a function of Q. A single Gaussian function (triangles) could be fitted to the streak up to Q ≈ 0.26 nm^{-1}. For higher Q values a second Gaussian function (circles) has to be used. Filled symbols correspond to data obtained at the 17 m detector position and open symbols to the 5 m detector position.

The previous SAXS analysis[57] assumes that the streak width is dominated at the smallest Q values by the dimension of the nanofibrillar objects and at higher Q values by their orientation. Thus, the two peak widths observed suggest the presence of two types of

nanofibrillar domains differing in chain orientation distribution. The low-Q tail, starting at about $Q \leq 0.25$ nm^{-1}, was attributed to central scattering due to larger scale features such as voids or crazes[57]. Avoiding the central scattering part of the curve, the angular width at $Q=0.25$ nm^{-1} is 8° fwhm, corresponding to $\Delta Q = 0.033$ nm^{-1} fwhm. The lower limit in nanofibrillar dimensions in axial direction (L) can be derived from the Scherrer formula[62] via $L = 1.8\pi/\Delta Q$ as about 170 nm. For a repeating unit of about 7.5 nm this corresponds to about 22 units along the nanofibrillar axis.

Results and discussion: dynamics

Des mesures de spectres de diffusion inélastique et quasiélastique par les techniques de spectrométrie de type "temps-de-vol" et de rétrodiffusion sont effectuées avec succès à températures ambiantes et inférieures, sur des échantillons de fibres alignées à différents états d'humidité (sèche, humidifiée avec H_2O, humidifiée avec D_2O), ce qui démontre pour la première fois la faisabilité de telles expériences pour ces échantillons. La possibilité d'obtenir des informations de diffraction en parallèle aux mesures de spectrométrie permet de contrôler la bonne marche des expériences en vérifiant la formation potentielle de glace sur la surface des échantillons, et donc de s'assurer de la cohérence des mesures. L'utilisation des différents instruments permet de couvrir une large gamme d'énergies. Un élargissement quasiélastique est nettement visible pour les soies humidifiées, et sa dépendance en fonction du vecteur de diffusion semble à première vue suffisamment marquée pour permettre une caractérisation de la mobilité moléculaire. Néanmoins, un processus de relaxation clair n'a pas pu être mis en évidence, et à ce stade il n'a pas été possible de faire correspondre un modèle aux données. A noter un faible, mais néanmoins mesurable signal quasiélastique pour la soie sèche, qui indique une faible mobilité des éléments diffuseurs, tandis que cette mobilité est très fortement augmentée lorsque de l'eau est ajoutée. Il est suggéré que le signal alors observé corresponde à la mobilité des polymères induite par la présence d'eau, sans pour autant exclure une contribution de l'eau confinée dans la soie. L'analyse de scans effectués sur un spectromètre à rétrodiffusion dans une fenêtre d'énergie constante, avec un transfert d'énergie nul -appelés scans élastiques-, corrobore cette interprétation. Elle permet aussi d'identifier le comportement harmonique, de type vitreux, pour la soie sèche, tandis que pour la soie humide la fonte de la glace amorphe contenue dans la fibre apparaît comme progressive. Le fait que cette fonte soit continue ou encore l'aspect caractéristique en "exponentielle étirée" de la courbe d'auto-corrélation obtenue d'après le signal quasiélastique sur le spectromètre de type "temps-de-vol", suggèrent l'existence non pas de quelques phénomènes de relaxation isolés mais plutôt d'une hiérarchie de phénomènes de relaxation pour la soie humide. Il est noté que la caractérisation de la mobilité moléculaire doit être couplée de manière attentive aux informations structurales.

Neutron spectroscopic experiments have been performed to obtain wave-vector resolved dynamical information on molecular length scales, and covering time scales from about four nanoseconds (backscattering spectroscopy) to picoseconds (time-of-flight spectroscopy). The experiments have been done as a function of temperature using a cryostat, with different humidity conditions of the sample. It was also possible to obtain from the spectroscopic experiments low resolution diffraction information. This was done in order to obtain further information on the status of water in the cryofrozen samples. (see also chapter 2)

Time-of-Flight spectrometry: IN6

Results

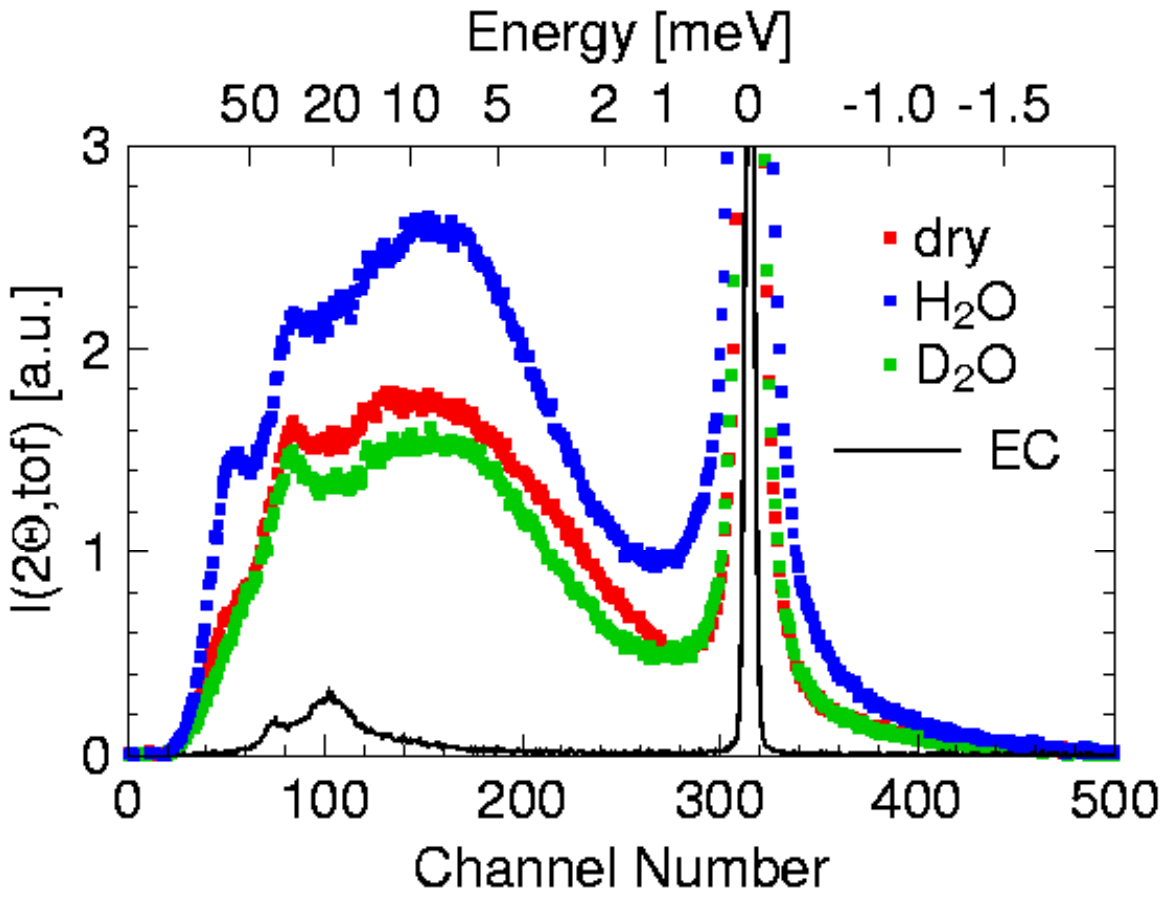

Figure 43 Q-integrated time-of-flight spectra of spider silk at 250K for different humidity conditions and empty can (EC). The energy scale has been calculated from the time-of-flight channels (upper axis on Figure 43). IN6 instrument. λ = 0.51 nm. Experiment 8-04-287. Empty can subtracted from silk signal. Q-integration from 2 nm^{-1} to 21 nm^{-1} (full instrument range). Bad detectors removed.

Time-of-Flight (TOF) spectra have been recorded on the cold-neutron spectrometer IN6 (for a detailed description, see chapter 2). The experiment was performed for different sample

temperature and humidity conditions. For the example given in Figure 43, the hydration was performed by soaking the silk for about one minute in H_2O or D_2O, then storing the sample in saturated humid atmosphere. Three spectra of different humidity conditions, same temperature, are given in Figure 43. The basic features visible on the spectra are the elastic line (zero energy transfer), the humidity dependent quasielastic broadening and inelastic signal. The width of the quasielastic broadening and the intensity of the inelastic signal change with humidity.

Diffraction information can be extracted from IN6 spectra by integrating over all time-of-flight channels. The patterns for a D_2O-humid sample at 100K and 300K are shown in Figure 44.

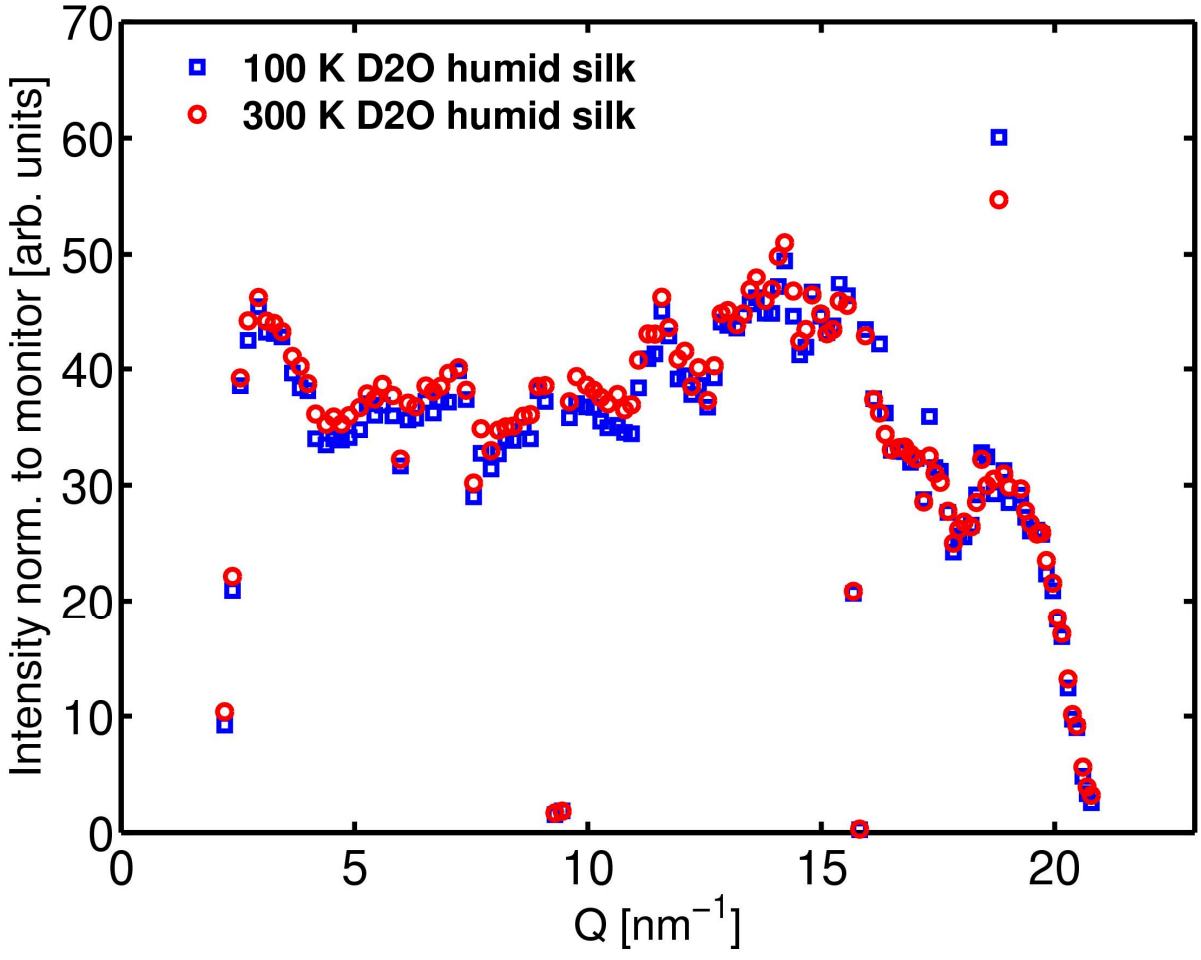

Figure 44 Diffraction information extracted from IN6 spectra for D_2O-humid sample at 100K and 300K. IN6 instrument. λ = 0.51 nm. Experiment 8-04-331. Middle detector row (tubes in scattering plane only). No correction for detector efficiency. Silk humidified by storage in atmosphere saturated with D_2O at room temperature prior to the experiment.

A few broken detectors (non-working or very noisy) are responsible for the sudden variation of isolated dots. The intensities are not corrected for detector efficiency. The patterns at 100K and 300K are similar, it is especially noted that no sharp crystalline peaks are visible.

Discussion

Feasibility: on Figure 43, the signal from the empty can is weak compared to the signal of silk. There was some gas in the empty cell, but for which almost no contribution is visible. This indicates that the way the sample cell was specifically designed is successful. The data are of sufficient quality even for the analysis of the inelastic signal. Thus, the feasibility of neutron spectroscopic experiments on aligned spider silk fibres has been for the first time established. This was not fully straightforward as first attempts with standard sample containers failed.

From Figure 44, it appears that the water freezes in an amorphous (glassy) state, as no crystalline peaks are observed. This is advantageous as the formation of crystalline ice in the silk could have destroyed the sample.

Dynamic scattering function S(Q, ω): in Figure 45, the scattering function S(Q, ω) of the sample calculated from the scattering signal (Figure 43) for the case of H_2O-humid silk is given. A significant broadening compared to the resolution is present. The broadening is increasing at higher Q-values. It becomes apparent that a Q-dependent data analysis is possible.

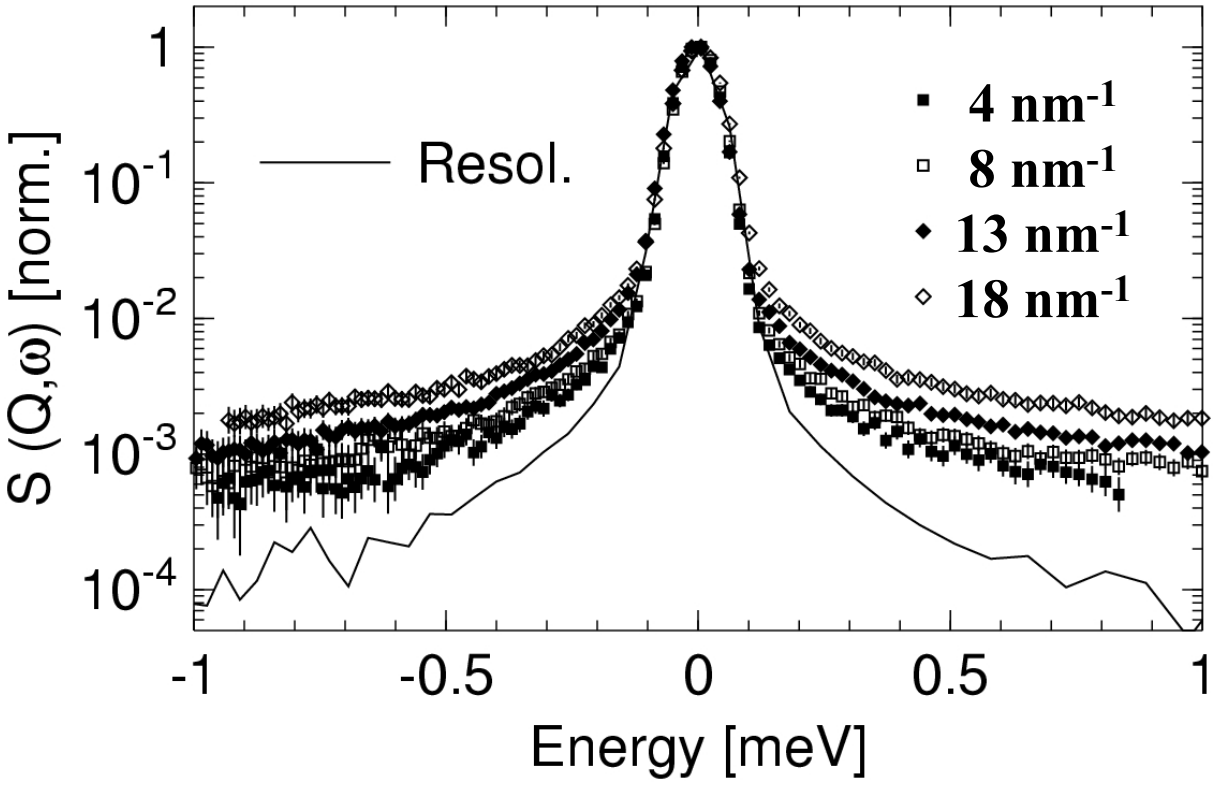

Figure 45 Dynamic scattering function derived from H_2O-humid silk spectra at 250K. The signal is integrated over $\Delta Q = 1$ nm^{-1}. IN6 instrument. $\lambda = 0.51$ nm. Experiment 8-04-287. Logarithmic intensity scale.

Quasielastic signal: for a deeper understanding of the diffusive processes giving rise to the quasielastic signal (Figure 45), a Fourier transform from frequency (energy) to time may be illustrative. Once in the time domain, the data can be corrected for the resolution by simply dividing by the Fourier transform resolution function. The resulting function is called the self-correlation function (see chapter 2) and is depicted in Figure 46 for the example of H_2O-humidified (20-30 wt.% humidity) silk at T = 290K.

The data may approximately be described by Q-dependent sloped-lines within the time-range. Such quasielastic scattering cannot be associated to a single relaxation function. What can be tentatively concluded from this figure is that the quasielastic signal of spider silk that is humid with water renders relaxation processes evident. However, it seems that the resulting relaxation processes are somewhat obscured by the resolution function of the time-of-flight spectrometer IN6. In any case it is not possible to extract a distinct single relaxation time within the energy window covered by IN6. Rather, a continuum of time scales may be present. This motivates to extend the energies scale (respectively time scale). Within the instrument suite available, it is easily possible to extend to higher energy resolution (backscattering instruments). This will be presented in a later section in this chapter.

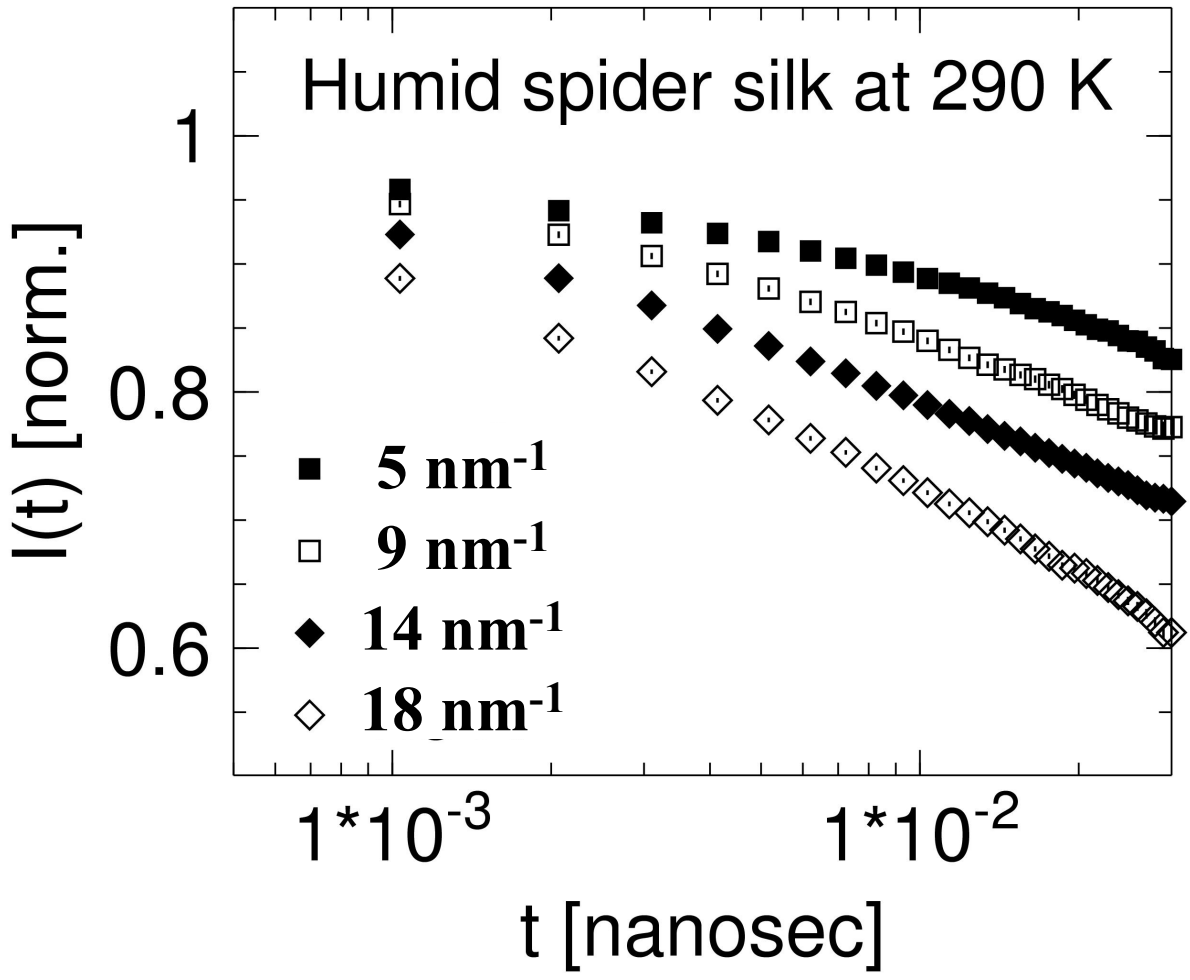

Figure 46 Self-correlation function obtained by a Fourier transform of the quasi-elastic scattering from humid (H_2O) spider dragline silk at a temperature T=290K. Data normalised in Fourier-space by dividing with the corresponding data of the resolution. The quasi-elastic scattering was measured on IN6 at an incident wavelength of 0.51 nm (Figure 45). λ = 0.51 nm. Experiment 8-04-287. Logarithmic intensity scale.

Inelastic signal: as mentioned previously, an elastic signal can be detected. Some obvious features can be identified. In the humid silk, near 50 meV energy transfer, the small peak can be assigned to water librations. Consistently, the libration peak nearly vanishes in the dry silk and also in the D_2O humid silk where the libration frequency is different.

At slightly lower energy (around 40 meV), a peak rising probably from the silk itself is visible. A further broad feature appears at even lower energy (between 1 meV to 20 meV). These contributions cannot be quantitatively analysed at the present state. It is noted that in the empty can signal, aluminium phonons are visible which are however already subtracted from the silk signal shown in Figure 43.

Quasielastic (from BS: IN16 & IN10b)

Results

Typical quasielastic spectra of spider silk obtained on the IN16 backscattering spectrometer are depicted in Figure 47. The red squares are the signal of the humid sample at low temperature (100 K), which corresponds to the resolution of the instrument. The green vertical crosses represent the signal from the dry silk and the blue circles the signal from the silk humidified with H_2O, both at 290 K. In this example, the hydration was performed by soaking the sample. As the acquisition for the dry sample was performed before, it implies that the sample was removed in between, thus having a slightly different alignment with respect to the beam.

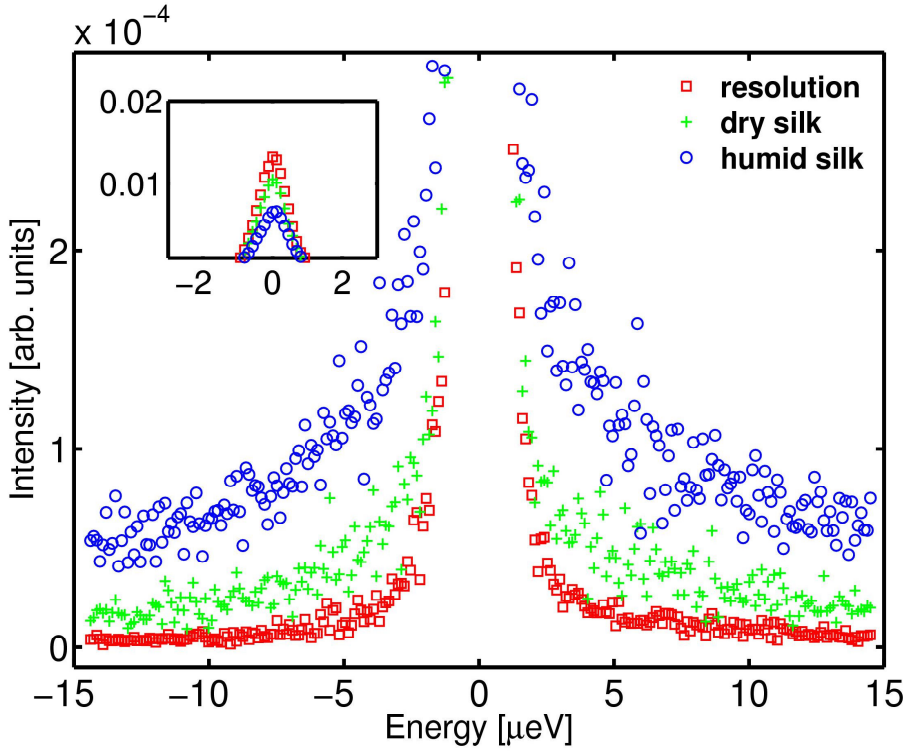

Figure 47 High energy resolution spectra obtained on IN16 for different humidity conditions. The inset axes units are the same as in the main frame. IN16 instrument. 11.6 < Q [nm^{-1}] < 14.2 ; T = 290 K ; normalised to monitor. H_2O-humid silk was soaked to achieve a maximum hydration.

The plot of the resolution deduced from the dry silk at low temperature is similar to the resolution deduced from the humid silk at low temperature (not shown). The data shown are an integration of four detectors, covering the Q space from 11.6 nm^{-1} to 14.2 nm^{-1}. The main frame is zooming on low intensities: a weak broadening to the elastic peak is visible for the dry silk, while a stronger one is visible for the humid silk. Outside the elastic scattering, the

intensity of the sample signal stays higher than the intensity of the resolution signal over the whole energy-window of the instrument. The top of the elastic peak is shown in the inset. The elastic peak intensity is weak for the humid silk, and reaches almost the resolution for the dry silk. This means that what is lost in elastic intensity goes at least partly to a quasielastic signal within the window of IN16.

Similar spectra are shown on Figure 48. They were obtained on the IN10b backscattering spectrometer, which has a lower intensity and a more coarse detection in the scattering angle (only seven detector tubes), but a wider energy window. Figure 48 also show the spectra obtained for different Q-ranges covered. The red crosses are the signal from the H_2O-humid silk at 90 K, which represents the resolution of the instrument. The blue circles are the signal from the H_2O-humid silk at 290 K, humidified, prior to the experiment, by storage in H_2O humid atmosphere. The green squares are the signal from the dry silk at 290 K, dried *in-situ* by pumping several minutes at 300 K. The plot of the resolution deduced from the dry silk at low temperature is similar to the resolution deduced from the humid silk at low temperature (not shown). The spectra are obtained by grouping respectively 2, 2 and 3 detectors, the total of the 7 detectors of the instrument covering a total Q-range of 5 nm^{-1} to 19.6 nm^{-1}. For the three spectra at different Q, the main frame is zooming to low intensities: the signal from the dry silk shows a weak broadening above the resolution, and there is a clearer broadening for humid silk. The signal converges at higher energy transfers to a constant background close to the level of the resolution. The insets take the whole intensity scale, zoomed at the low energy transfer, to show the elastic peak. The elastic intensity of the humid silk appears very slightly lower than for the dry silk, at half the value reached by the resolution. The non-symmetric shape of the peak arises from the instrument configuration.

On the IN16 instrument, it is possible to record a one-dimensional cross-section through the diffraction pattern simultaneously with the elastic or inelastic scans. The intensities recorded by the corresponding "diffraction" detector banks for two experiments with D_2O-humid silk are shown in Figure 49.

A

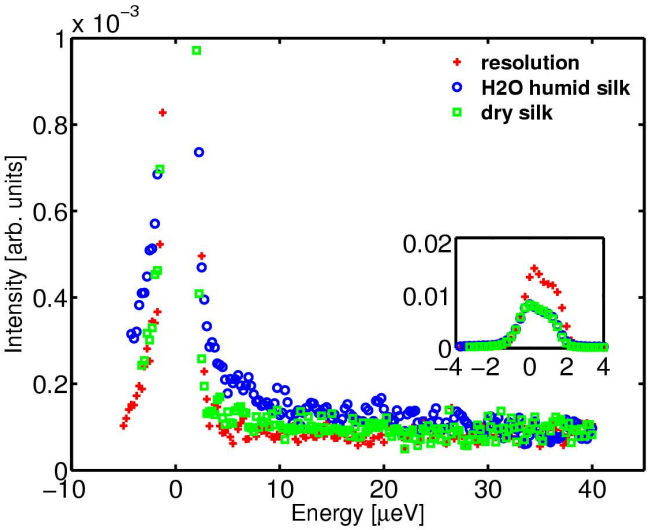

B

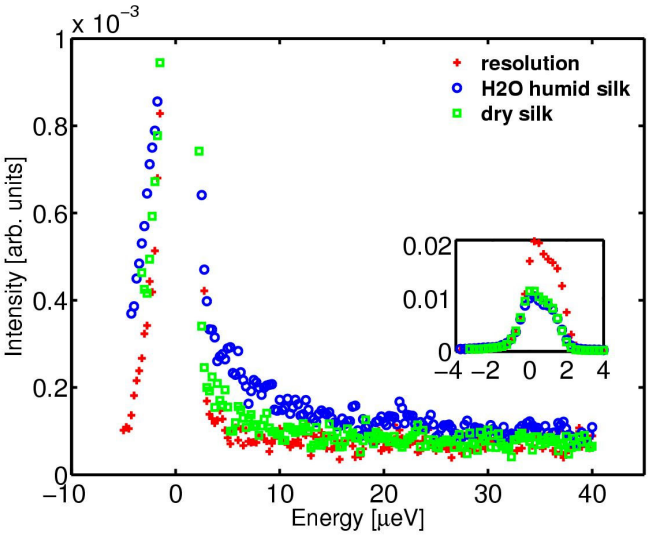

C

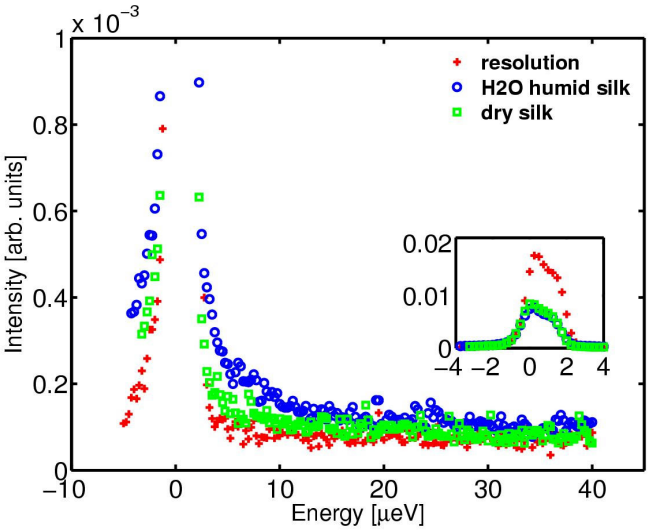

Figure 48 High energy resolution spectra obtained on IN10b for different humidity conditions (H_2O-humid, dry) for different Q range (centered at Q = 6.8 nm^{-1} (A), Q = 13.2 nm^{-1} (B) and Q = 18.3 nm^{-1} (C)). IN10b instrument. Analysed wavelength λ = 0.627 nm. T = 290 K. Humid silk obtained by storing overnight in H_2O-humid saturated atmosphere at room temperature. *In-situ* drying during several minutes pumping at 300 K.

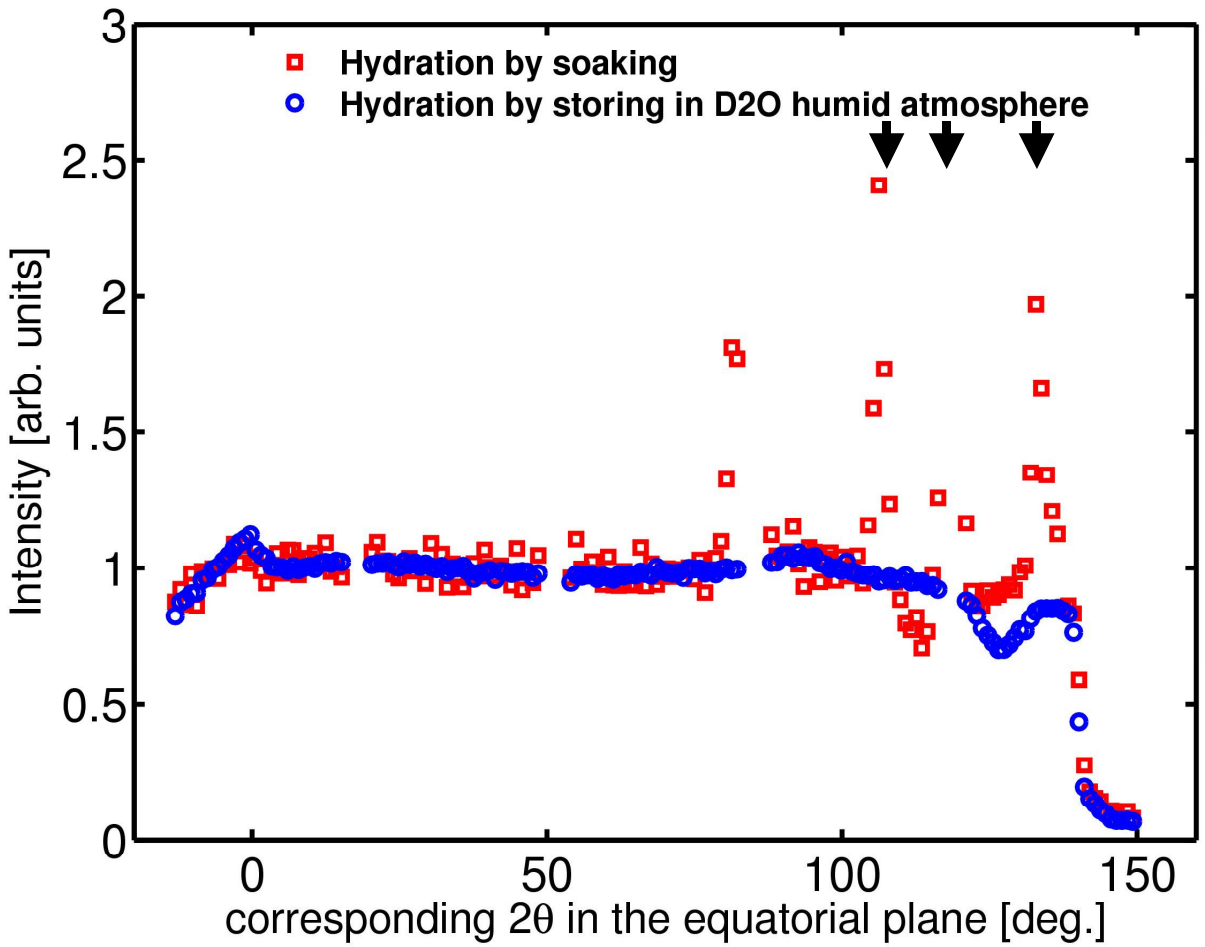

Figure 49 Intensity recorded on IN16 diffraction detectors for D_2O-humid silk at 250 K, from different hydration processes. Red points: the sample was soaked in D_2O. Blue points : the sample was stored in a D_2O humid atmosphere. IN16 instrument. λ = 0.627 nm. T = 250 K. "Elastic scan" of experiment 8-04-287 (squares) and "quasielastic scan" of experiment INTER-59 (circles). Arbitrary normalisation. The three arrows show peaks which disappear at room temperature.

The red squares correspond to the acquisition during an "elastic scan" on D_2O-humid silk, where the silk was humidified by a short soaking in D_2O. The blue circles correspond to the acquisition during a quasielastic scan on D_2O-humid silk where the silk was humidified by long storing in D_2O humid atmosphere. Both are obtained for the sample at 250 K. The first was performed with a five minutes acquisition time while the second was obtained in four hours, explaining the difference of noise level. Data from elastic and quasielastic scans are not comparable in intensity even when normalised to monitor, thus the normalisation is arbitrarily performed. The four equidistant gaps at approximately 20°, 50°, 90° and 120° are due to physical gaps between the detector banks. The little drops off around 110° to 130° are the shadow created by the aluminium frame of the sample holder, at different positions because the sample was slightly differently oriented depending on the experiment. The "peak" of red points near 80 to 90° correspond to detector tubes which were damaged for this experiment,

and repaired before the later INTER-59 experiment. The drop off around 140° to 150° is due to geometric constraints (shadowing from deflector chopper housing) inside the spectrometer. The three peaks under the arrows disappear when the temperature is higher than 270K.

Discussion

Induced mobility: on the insets of Figure 48, it appears that there is an extremely weak difference between the elastic peaks of humid or *in-situ* dried silk. One can directly relate this to the amount of scatterers as the sample was not moved in between. The amount of scatterers during the drying process decreases, while the elastic intensity increases. The increased intensity is therefore explained by a loss of inelastic signal found back in the elastic peak. This suggests that the presence of water induces some mobility. This will be further corroborated along with the discussion of Figure 52 (further in this chapter).

Quasielastic broadening: On Figure 47, a broadening is visible for dry silk, while extremely weak. This might correspond to the slow motions of the polymer chains. The broadening then seems to increase with humidity. One shall however be careful with these qualitative observations, as at the IN16 energy range, one cannot distinguish between a high background level, arising for example from the increase of the number of scatterers, or a large broadening, which would then contain meaningful information on motions. The IN10b experiment was performed in order to answer this question. As it clearly appears in Figure 48, the signal of humid silk continues to decrease beyond the energy transfer value of 15 μeV, the limit for IN16, until reaching the level of the resolution. The signal seen on the IN16 experiments therefore corresponds to real large broadening. As already discussed in the case of the time-of-flight experiments, it is clear that the water absorbed by the silk freezes in an amorphous state. The peaks observed in Figure 49, however, only appear for the experiments where the hydration was performed by soaking. Thus, they can be explained by the presence of free water at the surface of the fibre, freezing in a crystalline state. However, it is noted that the motions of free water correspond to much too high energies to be detected in the energy-window of backscattering instruments. Therefore, the fact that water is present at the surface of the fibre, which is indeed annoying to the point of view of humidity conditions and possible damage to the silk, should have no consequence on the quasielastic signal and does not explain the broadening observed. Water constrained in pores is slowed down, thus the energies of its motions are lower. A possible explanation for the broadening should then be that it comes from highly-constrained water. Another explanation of the increase of the

broadening signal might be that it is still a signal from the polymer chains, like observed for the dry silk, but enhanced by the presence of water, or a combination of both effects.

Analysis of the broadening: to discriminate between the possibilities previously mentioned and to clarify the origin of the signal, a further analysis is necessary. As an example, the Q-dependence of the signal for spider silk at 290 K observed on IN16 is shown in Figure 50. Fit results are shown together with the data, and will be discussed in a further paragraph.

The weak broadening for dry silk, as compared to the resolution, seems to be slowly increasing with Q, which is typical for diffusive motions. However, this effect might be not sufficiently significant here. By contrast, it clearly appears that the large broadening for humid silk is much stronger at small angle, and is decreasing with Q. The behaviour of decreasing broadening with Q is not expected for diffusive motions. One possible explanation might be that we observe, at small angles, slow confined water at the fast limit of the energy window. According to this assumption, the water (following a diffusive behaviour) at higher angles is 'too fast' and thus does not contribute to the detectable signal anymore. If this assumption is true, the elevated baseline for humid silk at lowest Q is not background but water (or polymers) moving faster than detectable. This phenomenon renders a quantitative fitting difficult. It is in qualitative agreement with what has been observed on IN10b, however the humidity conditions were not sufficiently controlled for a quantitative comparison.

Notwithstanding these difficulties, an attempt to fit a simple model to the IN16 is presented. The total intensity detected in an experiment is the result of the convolution of the dynamic scattering function $S(\mathbf{Q}, \omega)$ with the resolution of the instrument. To obtain $S(\mathbf{Q}, \omega)$, one therefore needs to de-convolute the signal. A de-convolution in the direct sense is normally not possible. Rather, a model is convoluted with the resolution function. The result is then fitted to the data. In the presented attempt, this is done by first building a spectrometer matrix with the resolution. This can be done either directly with the data points of the resolution, or by taking the values of a function fitted to the resolution data. In the data shown in Figure 50, the latter method is used. The spectrometer matrix is then multiplied by a model-vector (this operation is an numerical approximation of a convolution). The resulting convolution product is then fitted to the sample data by varying the parameters of the model.

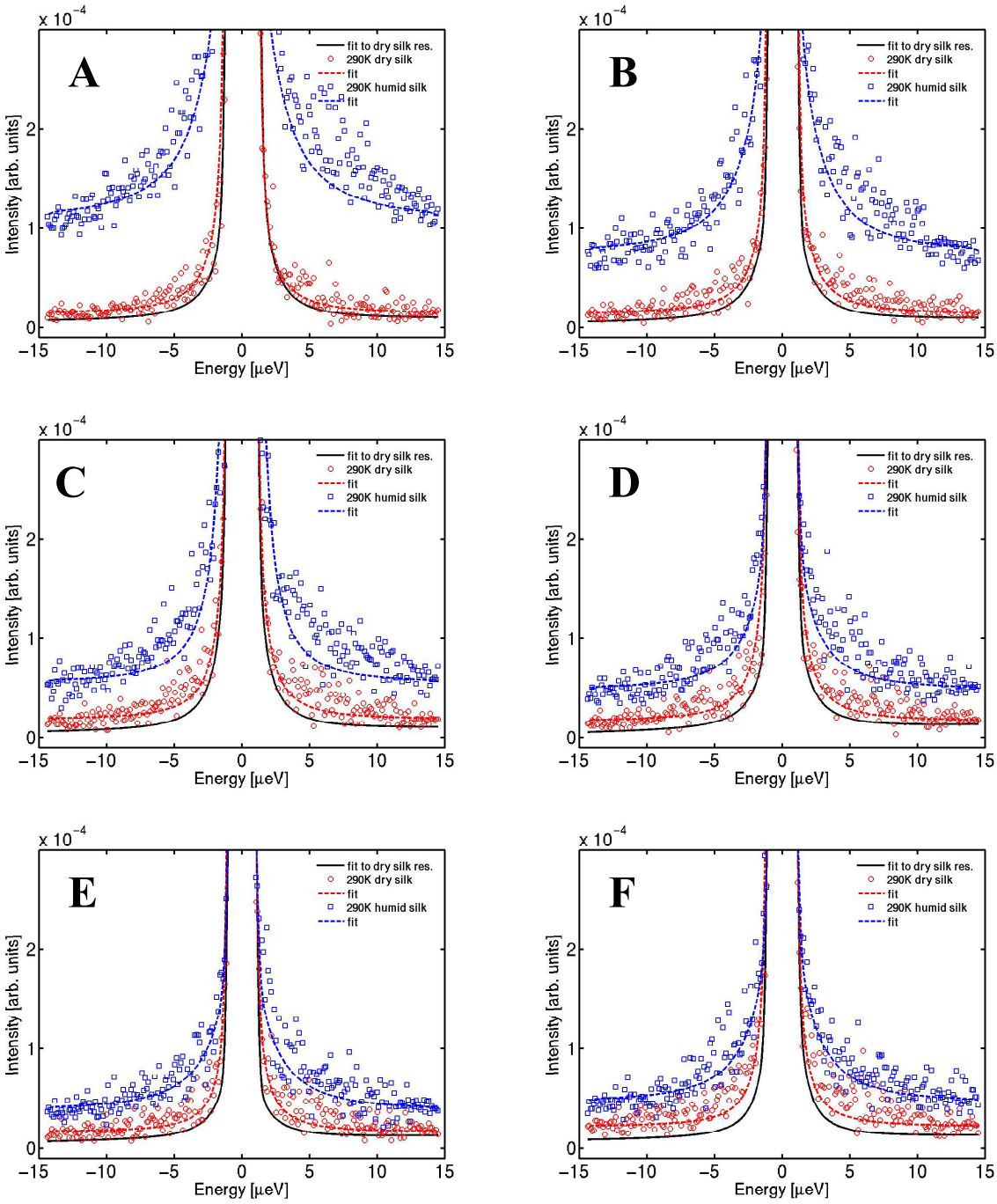

Figure 50 High energy resolution spectra obtained on IN16 for different humidity conditions at 290 K. Spectra are obtained by grouping detectors three-by-three, corresponding to Q positions of (A) 5.44 nm^{-1} ; (B) 8.63 nm^{-1} ; (C) 10.6 nm^{-1} ; (D) 15 nm^{-1} ; (E) 17 nm^{-1} and finally (F) 18.5 nm^{-1}.

The choice of a simple, even a simplistic model, was made for the first attempts. The scattering law can be separated into an elastic contribution, the Elastic Incoherent Structure Factor (EISF) which is represented by a Dirac peak (corresponding to static scatterers or slow motions below the resolution of the instrument), and the quasielastic contribution. There is various models to describe the motions of constrained water molecules. Motions are decomposed into translational and rotational contributions. Rotational motions are the fastest

and are not expected to contribute to the data of the high resolution experiments[63]. The remaining translational motions can be written as the sum of an infinite number of Lorentzians. In a typical QNS experiment, only a few Lorentzians will contribute to the quasielastic line. As it is not possible to distinguish different Lorentzians, the representation can be even more simplified into a single Lorentzian. The motions of polymer chains on the other hand are harder to take in account. Thus, for a first step, the fits are performed without taking into account any other parameter. The model presented here finally consists of two Lorentzians, a very narrow one (with a width of the order of the step size of the energy axis) for the EISF and a broad one for the quasielastic incoherent structure factor. The varying parameters are the intensity of the narrow Lorentzian, and the intensity, the width and the centre of the broad one. The fits are performed on MATLAB using a least squares method. More details on the fits are given in Annex. The results of the fits are given in Table 4.

Note that the same simplified model is applied for dried silk despite that the model initially describes motions of confined water. There is therefore no specific physical meaning. For dry silk, the comparison of the fits (dotted lines) to the data (symbols) in Figure 50 seems satisfying based on visual considerations. However, no clear Q-dependence of the broadening width (σ_1) appears in Table 4. For humid silk, the comparison of the fits to the data points in Figure 50 also seems satisfying based on visual considerations, at the exception of the group C (centred at Q = 10.6 nm^{-1}). One has to specify that among the several attempts performed with slightly modified approaches (choice of initial data, definition of the spectrometer matrix, fits on the resolution, fit algorithms and finally starting values), the illustrations shown are the best results obtained so far. However, as visible in Table 4, the width parameter of the Lorentzian representing the quasielastic contribution remains, for H_2O-humid silk, nearly constant near the starting value. This is the case for any reasonably chosen starting values (not shown). This is holds for the exception of the group at Q=10.6 nm^{-1}, where the deviation from the starting value is larger, however, this corresponds to the group C where the fit appeared to be unsatisfying on Figure 50.

	dry silk Lorentzians parameters						
	starting values	Q=5.44 nm^{-1}	Q=8.63 nm^{-1}	Q=10.6 nm^{-1}	Q=15 nm^{-1}	Q=17 nm^{-1}	Q=18.5 nm^{-1}
A_1 (a.u.)	0.001	0.0123	0.0028	0.0006	0	0.0006	0.006
σ_1 (μeV)	0.5	0.003	0.0056	0.0071	0.0002	0.4501	0.0666
E^0_1 (μeV)	0	0.226	0.2299	0.2302	0.2302	0.1987	-0.321
A_2 (a.u.)	1	0.0531	0.0534	0.0609	0.0755	0.0734	0.0567

	H_2O-humid silk Lorentzians parameters						
	starting values	Q=5.44 nm^{-1}	Q=8.63 nm^{-1}	Q=10.6 nm^{-1}	Q=15 nm^{-1}	Q=17 nm^{-1}	Q=18.5 nm^{-1}
A_1 (a.u.)	0.001	0.006	0.005	0.016	0.0026	0.0036	0.0033
σ_1 (μeV)	5	5.001	5.0006	0.4712	5.0044	5.0068	5.0027
E^0_1 (μeV)	0	0.0098	0.0074	0.0879	0.0075	0.0044	-0.016
A_2 (a.u.)	1	0.0256	0.0224	0	0.0222	0.0176	0.0139

Table 4 Parameters of the fit curves shown in Figure 50 for (A) dry silk and (B) humid silk. The model convoluted to the data consists of two Lorentzians, a broad and a narrow one: $L = \frac{A_1}{\pi}\frac{\frac{1}{2}\sigma_1}{\left(x-E_1^0\right)^2+\left(\frac{1}{2}\sigma_1\right)^2} + \frac{A_2}{\pi}\frac{\frac{1}{2}\sigma_2}{\left(x-E_2^0\right)^2+\left(\frac{1}{2}\sigma_2\right)^2}$. The width σ_2 and the position E^0_2 of the narrow Lorentzian are fixed to respectively 0.1 μeV and zero energy transfer.

Therefore a satisfying fit could not be obtained. The Q-dependence of the broadening (width of the Lorentzian) did not appear in the attempts performed so far. The reasons of the failure can be attributed mainly to (i) the fact that, as previously mentioned, the motions occur out of the detectable energy-range of the instrument and/or (ii) the chosen model may not describe correctly the motions behaviour. The answer to the first point would be to use the data from the IN10b instrument, which has a wider energy window. Unfortunately, the statistics of the data on this instrument are much weaker. The Q-resolution is limited to seven detectors as compared to the twenty detectors of IN16, on which a grouping over several detectors was already necessary to obtain a signal satisfyingly strong. Thus the Q-dependence of the signal might almost not be observed on IN10b, while qualitative observations of IN16 data suggest a strong effect. Last, the instrument resolution of IN10b is not symmetric, which significantly

complicates the fitting routine. Concerning the choice of the model, one shall note that a fit with a too complicated model would not be relevant with data of weakly scattering systems.

In conclusion for the fitting, the presented attempt consists of a first step, not leading yet to satisfying conclusions, but preparing the path for further analysis on possibly new experiments.

Elastic scans

Results

The "fixed energy window" (FEW) scans, where the intensity scattered within the energy resolution window of the spectrometers is recorded, give an overview of dynamical phenomena in a sample. They were performed on the IN16 spectrometer.

The elastic intensity (zero energy transfer) integrated over the whole instrument Q-range (from 4.3 nm^{-1} to 19nm^{-1}) from the dry silk sample, and H_2O/D_2O humidified (by soaking) silk samples, depending on temperature from 20 K to 300 K, is reported in Figure 51.A. The intensities are normalised to the maximum value at the corresponding humidity condition. At low temperature (up to 200 K), the intensity decays with a slowly increasing slope, showing qualitatively the same behaviour for all humidity conditions. The dry silk keeps this behaviour over the whole temperature range. The decay increases a first time around 225 K for H_2O humid silk and around 250 K for D_2O humid silk. A second, sudden drop of the intensity occurs around the melting temperatures of water (273 K for H_2O and 277 K for D_2O) for humidified silk samples. The data from the dry silk are shown in more detail in Figure 51B, taking four detector groups corresponding to different Q positions (at 5, 11, 16 and 19 nm^{-1}).

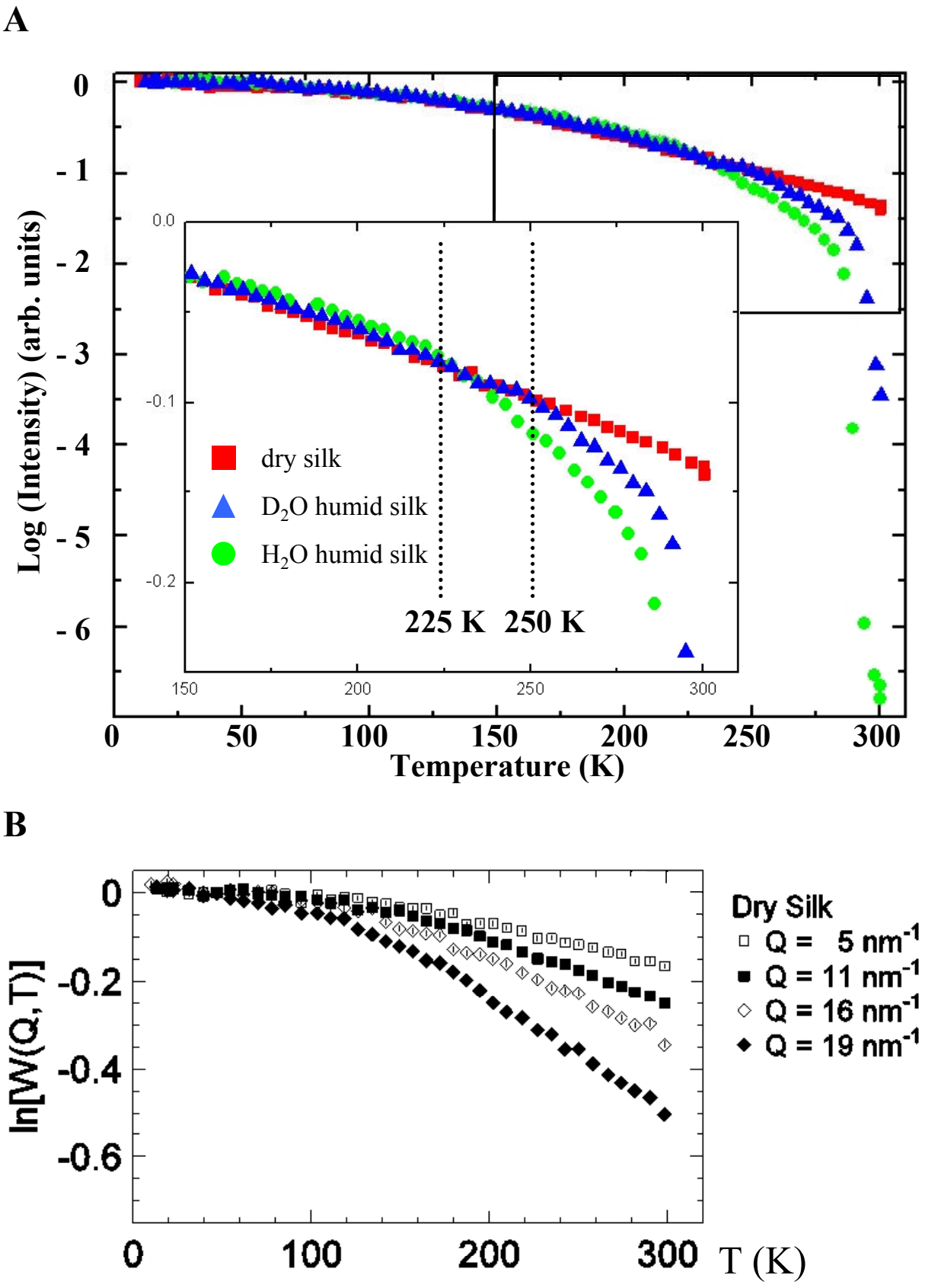

Figure 51 "fixed energy window" window scan centred at zero energy transfer, (A) Q-integrated over the full instrument range (4.3 to 19 nm^{-1}) for different humidity conditions, and (B) showing the Q-dependence for dry silk. *W* represents the elastic peak intensity. IN16 instrument. λ = 0.627 nm. Experiment 8-04-287.

A different FEW scan was performed around 290K-300K while pumping on the sample environment. The elastic intensity integrated over the whole Q-range of the instrument is shown Figure 52. The sample at the initial state is silk humidified with H_2O. During the pumping, the capillary inside the cane is heated, thus heating the sample environment. The heating power is variable during the experiment, explaining the irregular variation of temperature between each step. The elastic intensity is increasing during the pumping process.

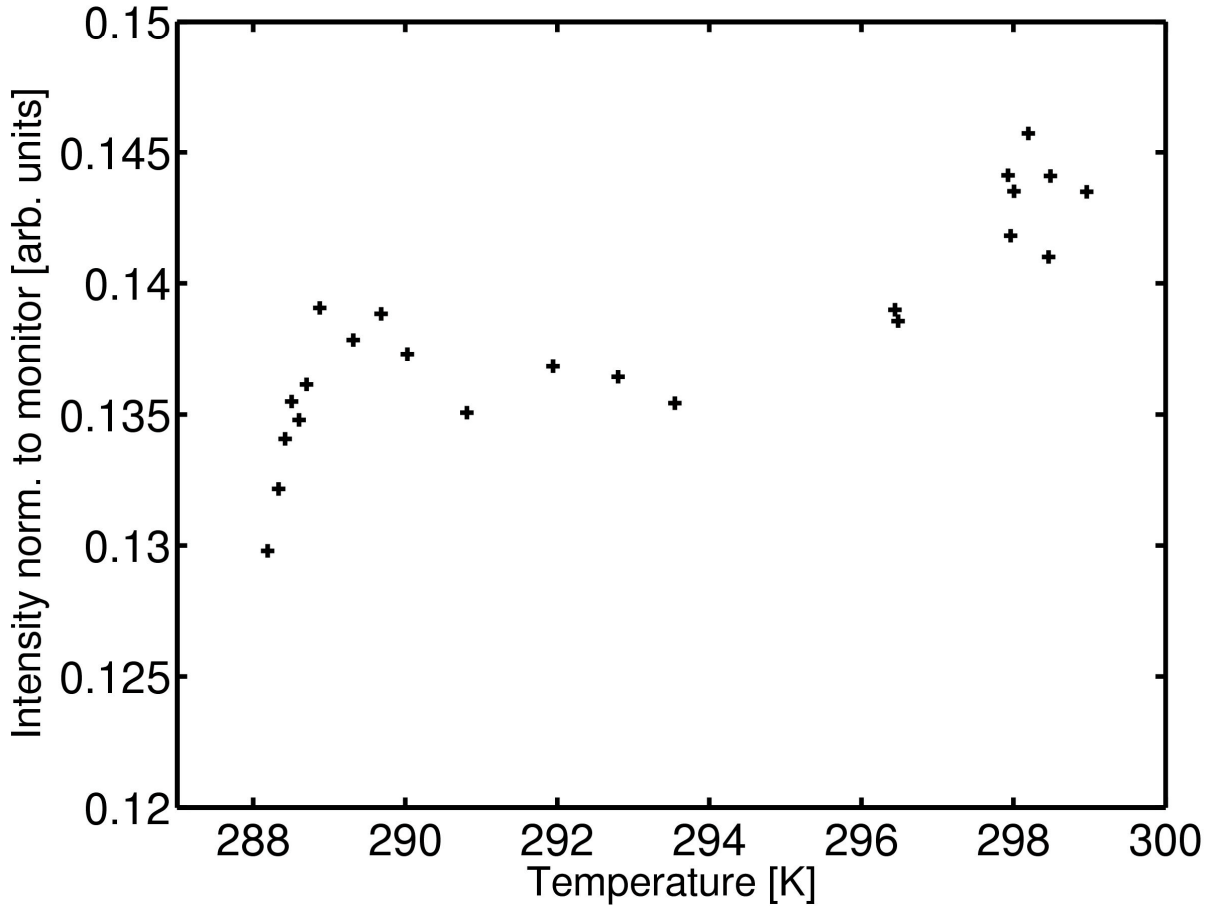

Figure 52 "fixed energy window" scan centred at zero energy transfer, Q-integrated over the full instrument range (4.3 to 19 nm^{-1}) for silk initially humidified with H_2O during its *in-situ* drying by pumping. The temperature slowly and continuously increases during the pumping. The acquisition time is of 3 minutes, and the acquisition starts about 30 seconds after the pumping. IN16 instrument. λ = 0.627 nm. Experiment 8-04-331.

Discussion

Molecular mobility: the fixed window scans are analysed to improve qualitatively the observations. Assuming a simple $W(Q,T) = \exp(-\langle u^2(T)\rangle Q^2)$ dependence of the elastic intensity, the mean-square displacement ($\langle u^2(T)\rangle$) of the scatterers can be calculated from the

Q dependence of *W(Q,T)*. The equation $I = I_0 \exp(-\langle u^2(T)\rangle Q^2) + c$ is thus fitted to the data, and plotted in Figure 53.

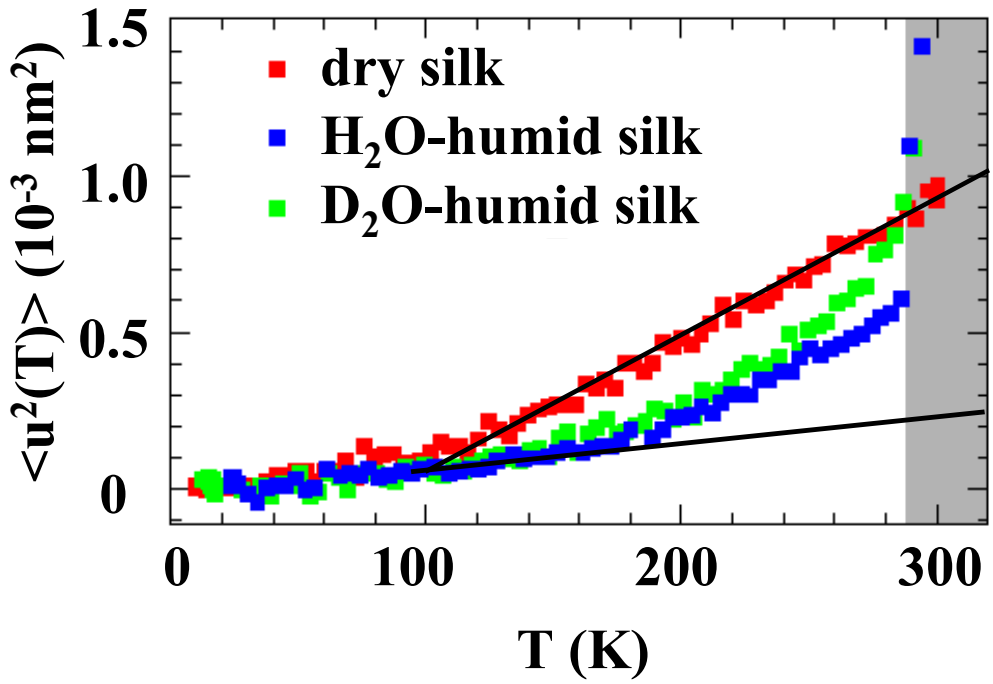

Figure 53 Mean square displacement of the scatterers $\langle u^2(T)\rangle$ calculated from the Q-dependence of the elastic scans. Full lines indicate the behavior expected for harmonic solids and matched to the data of dry silk and H_2O humidified silk. The grey shaded area stresses the temperature range in which the $\langle u^2(T)\rangle$ of humidified silk exceeds $\langle u^2(T)\rangle$ of dry silk.

In the case of the native silk, the overall temperature dependence of $\langle u^2(T)\rangle$ is reminiscent of the properties of a harmonic system. By contrast, in the humidified samples the behavior is nonharmonic above about 200K. This feature is tentatively attributed to a gradual melting of amorphous water. Since no sharp transition can be identified, this melting behavior is unlike in systems with well-defined pore sizes. It rather looks like a continuous melting process resulting from water confined in a hierarchy of pore sizes within the random network of the amorphous silk fractions. Below 200K, the response of the frozen-in state of both H_2O and D_2O humidified silk can be well compared with the behaviour of amorphous ice[64, 65]. This marks the system as harmonic and more rigid than the native silk, which is evidenced by the smaller $\langle u^2(T)\rangle$ values.

Induced mobility: it has already been discussed, based on the elastic intensity from the IN10b data shown in the inset of Figure 48, that the amount of scatterers during the drying process decreases, while the elastic intensity increases. This effect is clearly visible on Figure 52, which corroborates the previous suggestion that the presence of water induces some mobility.

On Figure 53 at room temperature, the enhanced $<u^2(T)>$ of the humidified samples may not be exclusively attributed to relaxation of water molecules within the amorphous silk matrix. This point can be clearly elaborated by subtracting the response of the dry silk from the humidified silk samples $\Delta W(Q,T) = W_{humid}(Q,T) - W_{dry}(Q,T)$. The difference spectra obtained are displayed in Figure 51.

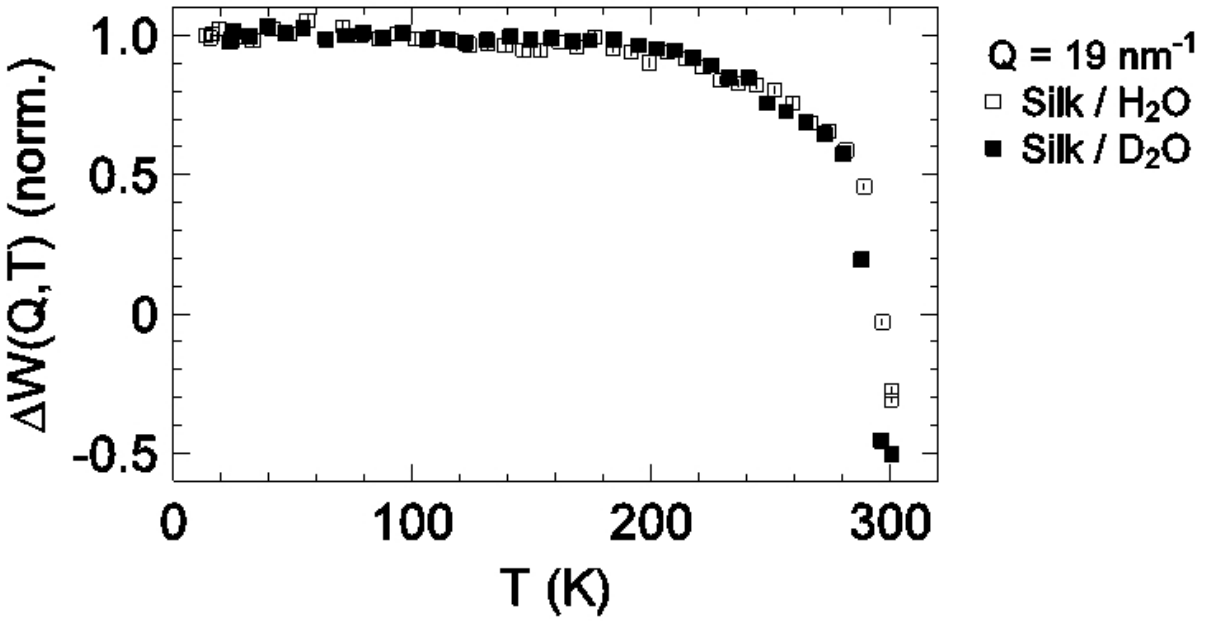

Figure 54 Difference signal of H_2O and D_2O humid silk minus native dry silk. The difference spectra are shown only at a single Q of 19 nm^{-1}. The intensities before subtraction were measured at "fixed energy window" scan centred at zero energy transfer (Figure 51).

In a simplified picture of a separated water and polymer dynamics one would expect $\Delta W(Q,T)$ to be dominated by the water response and to remain a positive property. However on Figure 51, the $\Delta W(Q,T)$ becomes appreciably negative at room temperature. This can be only the case when the humid samples comprise a remarkably higher degree of decay channels than liquid water at equal thermodynamic conditions. In other words, the mobility of polymer chains is enhanced by the presence of water.

Summarising discussion of spectroscopy experiments

What has not yet been discussed in detail is that a good knowledge of the structure has to be taken into account for a further detailed analysis of spectroscopic data. This is illustrated by Figure 55, where the IN16 detectors are schematically superimposed to the structure of spider silk obtained on D19 in reciprocal space. The area covered by the IN16 detectors along the

azimuthal direction is only schematically represented and does not correspond to reality. The boxes are however centred on the equator as the silk fibre axis was perpendicular to the scattering plane of the spectrometer. The equatorial Q-range covered by each detector is exact.

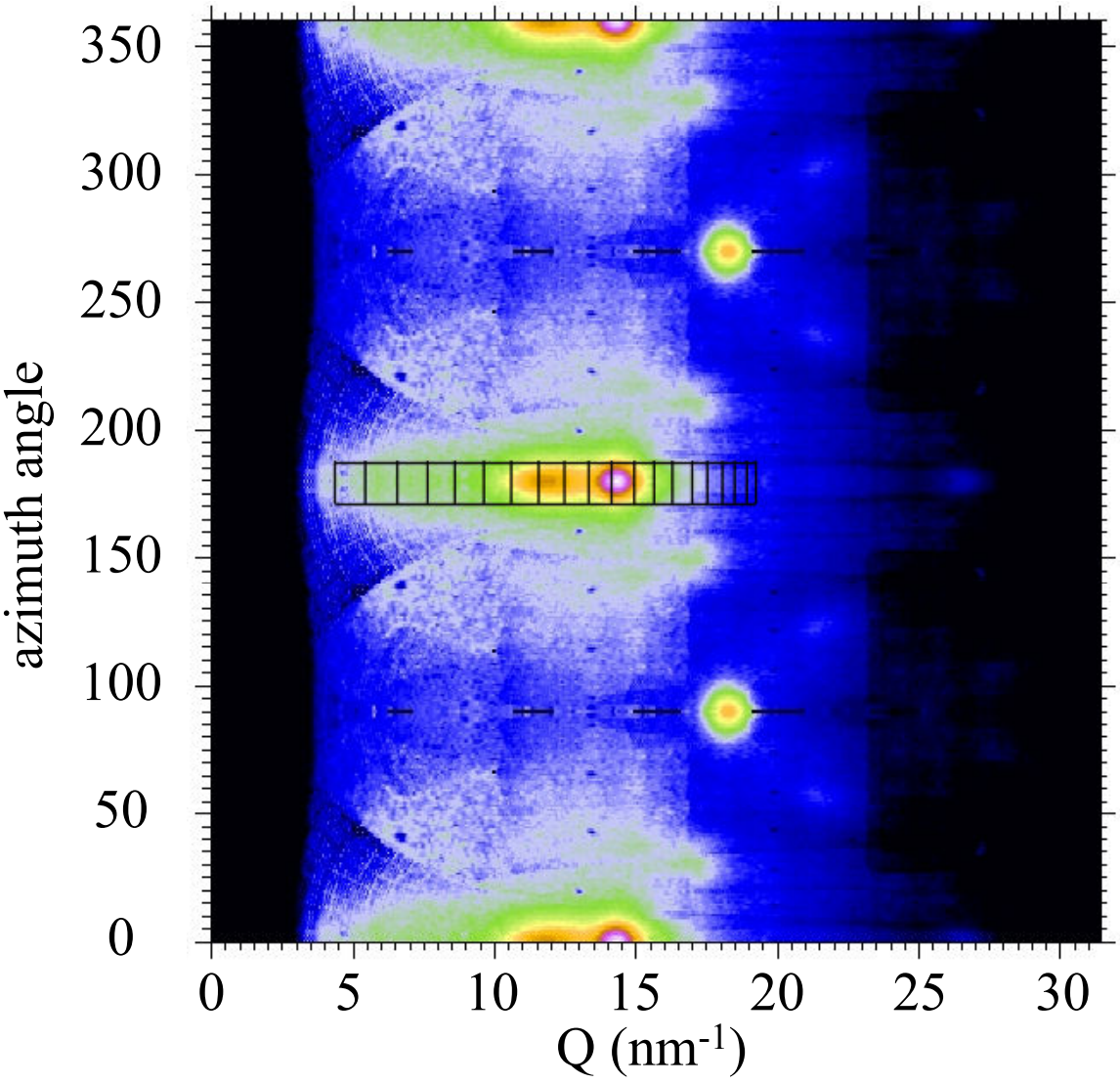

Figure 55 Cake-regrouped neutron fibre diffraction pattern of H_2O-humidified silk superimposed with the area covered by the IN16 detectors (boxes on the equator). The IN16 multidetector tubes are evenly spaced in 2θ.

It appears on Figure 55 that approximately half of the detectors cover an area superimposed with the spider silk diffraction peaks. On IN16, due the bad angular resolution linked to the important incoming beam divergence, the peaks are probably larger. The presence of coherent scattering complicates the quasielastic data analysis. Up to now, this analysis was not

successful even on the angular areas not "contaminated" with Bragg peaks, but that is to be considered for further analysis.

What can be learned from the spectroscopic experiments up to now is that

- the feasibility of neutron spectroscopic experiments on aligned spider silk fibres has been for the first time established.
- native spider silk at room temperature seems to behave like a glass.
- only some very little mobility is present for dry silk.
- when water is added :

(i) we see a hierarchy of relaxation processes (as concluded from the stretched exponential behaviour in relaxation processes, discussion on Figure 46)

(ii) the water seems to freeze to amorphous ice (except for residual water at the fibre surface when the sample is soaked and droplets not sufficiently removed afterwards) as clearly concluded from diffraction information inherent in the IN6 spectra and from the IN16 diffraction detectors. This corroborates ID13 cryostream experiment (see chapter 3, low temperature X-ray diffraction)

(iii) The amorphous ice seems to be continuously melting with rising temperature (see section on elastic scans)

(iv) possibly water enhances the mobility of polymer chains (as tentatively concluded from the elastic and quasielastic data combined).

Conclusion

Une traduction en français de cette conclusion est donnée à la suite de la version anglaise.

Spider dragline silk is a remarkable material. It is a crystalline biopolymer with outstanding mechanical properties, spun at ambient temperature and pressure conditions, and also biodegradable and recyclable. There is therefore an interest in understanding and mimicking this material. It has been in the focus of intense research using a wide variety of experimental techniques and in addition theoretical modelling. Primary structure (the sequences of its two main proteins) and secondary structure (the beta-sheet folding of the crystalline part of the proteins) are already well known. Structural models at higher scales are however still discussed. Functional models that link the microscopic structure and dynamics of spider dragline silk to its macroscopic properties, lack of information on the dynamical properties and on the influence of water at the microscopic scale, known to be important for the mechanical properties. In this project, neutron scattering techniques were used, as they are sensitive to light elements and especially hydrogen atoms, making them suitable to probe hydration-sensitive phenomena. They also allow dynamics to be probed. Previous results and new experiments using X-ray microdiffraction supported the discussion.

Experimental achievements: The feasibility of neutron scattering experiments has been established for small- and wide-angle scattering, time-of-flight spectroscopy and backscattering spectroscopy, provided that a sufficient quantity of sample is used. Humidity conditions on the sample environment at room temperature have been successfully controlled, while difficulties have been identified for the sample on cryostated environments. *In-situ* drying was nevertheless possible on cryostated environments. In any case, the hydration by H_2O or D_2O permitted to use contrast variation techniques.

Main results and interpretations: The results can be divided in three main categories, linked to three main groups of techniques.

Structural and water accessibility information at short scale (from atomic scale model to a few nanometers) were obtained by wide-angle scattering. Neutron fiber diffraction patterns were obtained for silk humidified with pure H_2O and for silk humidified with pure D_2O. According to the comparison of these experimental patterns with simulations, the crystalline fraction shows no or only little H/D exchange. Moreover, a meridional superlattice reflection was observed on the pattern of silk humidified with pure D_2O, at the position of the forbidden 001

reflection. This reflection, not observed on the pattern of silk humidified with H_2O and never observed by X-ray scattering, was attributed to oriented but non-crystalline domains, described as a smectic structure, accessible to H/D exchange in this model. An X-ray microdiffraction experiment on single fibres showed that water absorbed by the silk freezes in an amorphous state, which is a result of importance for the analysis of small-angle scattering and spectroscopic experiments.

Results from small-angle scattering provided information on the structure and water accessibility at longer scale (from a few nanometers to a few hundred of nanometers). The meridional peak and equatorial streak contributions change of intensity with the water content of the silk and with the D_2O content of the solvent. For the equatorial streak intensity, the evolution has been characterised as a consequence of water absorption mainly, while the influence of the H/D exchange on absorbed water but also on some amino acid residues is advanced for the evolution of the meridional peak intensity. The analysis has been extended to small Q-values, allowing the measurement of the dimension of the nanofibrillar objects to be refined.

The molecular mobility was probed by neutron spectroscopy. The diffraction information available at low resolution on these instruments suggested as already seen by X-ray microdiffraction that the water absorbed by the silk freezes in an amorphous state. Mobility of native spider silk showed a weak signal which could however be characterised as a harmonic, glass-like behaviour. The complexity increases when water is added. The mobility was then described by a hierarchy of relaxation processes, a continuous melting of the contained water when the temperature increases, and an enhancement of the mobility of polymer chain induced by the presence of water.

Three-phase nanofibrillar model: It is noted that most of the results can be satisfyingly explained with the approach of a three-phase model, made of crystallites, an oriented noncrystalline phase and an amorphous matrix. In this model (Figure 56, adapted from [20, 45]), the crystallites and oriented domains arrange themselves in order to form a nanofibrillar structure. The interpretation of several results as listed previously is rendered more consistent in such a model, as several experiments provide information leading to a similar conclusion. For instance the accessibility of the oriented noncrystalline domains to water is deduced from the interpretation of both WANS and SANS results within this model. In general, it provides a possible description of the influence of water on the microscopic structure and dynamics.

Such description shall be tested in functional hierarchical models to predict the impact of water on the mechanical properties.

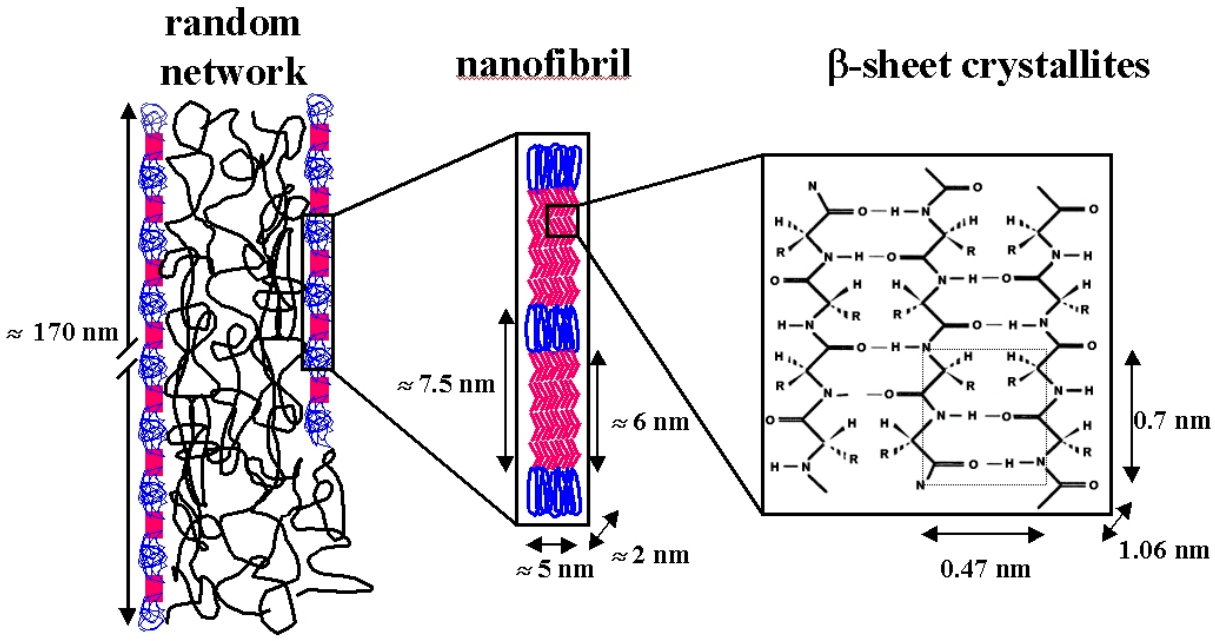

Figure 56 Three-phase model for spider dragline silk, adapted from a model originally proposed by Grubb[45] and by Riekel[20]. Crystallites (in red) of antiparallel β-sheets have a unit cell of 0.47, 1.06, 0.7 nm[17] along *a*, *b*, *c*, and are of a size of about 5x2x6 nm^3[20] along the same axes. The crystallites arrange themselves along the fiber axis with the oriented noncrystalline domains (in blue), with a repetitive motif of about 7.5 nm, forming a nanofibrillar structure. These nanofibrils, of a length of about 170 nm[57, 66], are embedded in an amorphous matrix made by a random network of polymer chains.

Modèle à trois phases représentant le fil de traîne de l'araignée, adapté d'un modèle initialement proposé par Grubb[45] *et par Riekel*[20]. *Les cristallites (en rouge) de feuillets β antiparallèles ont une maille élémentaire de 0.47, 1.06, 0.7 nm*[17] *selon a, b, c, et font une taille de 5x2x6 nm^3*[20] *selon les mêmes axes. Les cristallites s'organisent le long de l'axe de la fibre avec les domaines orientés non cristallins (en bleu), avec un motif répété d'environ 7.5 nm, créant une structure nanofibrillaire. Ces nanofibrilles, d'une longueur d'environ 170 nm*[57, 66], *sont contenues dans une matrice amorphe faite d'un réseau aléatoire de chaînes de polymère.*

Conclusion

Le fil de traîne de l'araignée est un matériau remarquable. C'est un biopolymère cristallin aux exceptionnelles propriétés mécaniques, tissé dans les conditions de température et de pression ambiantes, par ailleurs biodégradable et recyclable. Il existe en conséquence un intérêt à comprendre et imiter ce matériau. Il a été au centre d'une intense recherche utilisant une large gamme de techniques expérimentales et de modélisations théoriques. La structure primaire (les séquences de ces deux principales protéines) et la structure secondaire (le repliement en feuillets bêta de la partie cristalline des protéines) sont d'hors et déjà bien connues. Les modèles structuraux à plus grandes échelles sont cependant encore en discussion. Les modèles fonctionnels, qui relient les propriétés structurales et dynamiques microscopiques du fil de traîne de l'araignée à ses propriétés macroscopiques, manquent d'informations sur les propriétés dynamiques ainsi que sur l'influence de l'eau à l'échelle microscopique, connue pour être importantes pour les propriétés mécaniques. Au cours de ce projet, les techniques de diffusion neutronique ont été utilisées. Leur sensibilité aux petits éléments et en particulier aux atomes d'hydrogène les rend adaptées pour sonder les phénomènes dépendant de l'hydratation. Elles permettent aussi de sonder la dynamique. De précédents résultats ainsi que de nouvelles expériences utilisant la microdiffraction des rayons X ont étayé la discussion.

Réalisations expérimentales : La faisabilité d'expériences de diffusion neutronique a été établie pour la diffusion aux petits angles, la diffraction, la spectroscopie temps-de-vol et la spectroscopie à rétrodiffusion, à condition qu'une quantité suffisante d'échantillon soit utilisée. Les conditions d'humidité de l'environnement de l'échantillon à température ambiante ont été contrôlées avec succès, tandis que des difficultés ont été identifiées pour l'échantillon placé en environnement cryostaté. Le séchage *in-situ* est néanmoins demeuré possible dans les environnements cryostatés. Dans tous les cas, l'humidification par H_2O ou D_2O a permis d'utiliser les techniques de variation de contraste.

Principaux résultats et interprétations : Les résultats peuvent se classer en trois groupes principaux, reliés à trois principaux groupes de techniques.

Les informations structurales et sur l'accessibilité de l'eau à petites échelles (de l'échelle atomique à quelques nanomètres) ont été obtenues par diffraction. Des clichés de diffraction de neutrons par les fibres ont été obtenus pour la soie humidifiée par pur H_2O et pour la soie humidifiée par pur D_2O. D'après la comparaison de ces clichés expérimentaux avec des simulations, il n'y a pas ou peu d'échange H/D dans la partie cristalline. De plus, une réflexion

méridionale hors réseau a été observée sur le cliché de la soie humidifiée par pur D_2O, à la position de la réflexion interdite 001. Cette réflexion, qui n'est pas observée sur le cliché de la soie humidifiée par pur H_2O et qui n'a jamais été observée par diffusion des rayons X, a été attribuée aux domaines orientés mais non cristallins, décrits comme ayant une structure de type smectique, accessibles à l'échange H/D dans ce modèle. Une expérience de microdiffraction des rayons X sur des fibres uniques ont montré que l'eau absorbée par la soie gèle dans un état amorphe, ce qui est un résultat fondamental pour l'analyse des expériences de diffusion aux petits angles et de spectroscopie.

Les résultats de la diffusion aux petits angles ont apporté des informations sur la structure et l'accessibilité de l'eau à de plus grandes échelles (de quelques nanomètres à quelques centaines de nanomètres). Les contributions de la réflexion méridionale et de la traînée équatoriale changent d'intensité avec la quantité d'eau absorbée par la soie ainsi qu'avec le taux de D_2O contenu dans le solvant. L'évolution de l'intensité de la traînée équatoriale a été caractérisée comme découlant de l'absorption de l'eau essentiellement, tandis que c'est l'influence de l'échange H/D pour l'eau absorbée mais aussi pour certains résidus d'acides aminés qui est avancée pour expliquer l'évolution de la réflexion méridionale. L'analyse a été étendue aux petites valeurs de Q, ce qui a permit d'affiner la mesure des dimensions des objets nanofibrillaires.

La mobilité moléculaire a été sondée par spectroscopie neutronique. Les informations de diffraction, disponibles à basse résolution sur ces instruments, suggèrent comme il a déjà été évoqué avec la microdiffraction des rayons X que l'eau absorbée par la soie gèle dans un état amorphe. La mobilité dans la soie naturelle a montré un faible signal qui a pu néanmoins être identifié comme présentant un profil harmonique, similaire au verre. Le système devient plus complexe lorsque l'eau est ajoutée. La mobilité a alors été décrite par une hiérarchie de phénomènes de relaxation, une fonte progressive de l'eau absorbée quand la température augmente, ainsi qu'une augmentation de la mobilité des chaînes de polymères induites par la présence d'eau.

Modèle nanofibrillaire à trois phases : On souligne que les résultats, dans leur majorité, peuvent être expliqués dans l'approche d'un modèle à trois phases, fait de cristallites, d'une phase orientée mais non-cristalline et d'une matrice amorphe. Dans ce modèle (Figure 56 présentée dans la version anglaise de cette conclusion, adaptée de [20, 45]), les cristallites et les domaines orientés s'organisent entre eux afin de créer une structure nanofibrillaire. L'interprétation de plusieurs résultats telle qu'énoncée plus haut est rendue plus rationnelle

dans le cadre de ce modèle, plusieurs expériences différentes fournissant des informations allant dans le même sens. Par exemple, l'accessibilité de l'eau dans les domaines orientés non-cristallins est déduite de l'interprétation au sein de ce modèle des résultats provenant de diffraction neutronique mais aussi de diffusion neutronique aux petits angles. En général, il fournit une description possible de l'influence de l'eau sur les propriétés structurales et dynamiques à l'échelle microscopique. Une telle description pourrait être testée par des modèles fonctionnels afin de prédire l'impact de l'eau sur les propriétés mécaniques.

Outlook

Une traduction en français des perspectives est donnée à la suite de la version anglaise.

Neutron source:

The main limiting factor shared by all neutron scattering experiments is the brilliance of the source. This is well illustrated by all the experiments performed on spider silk, where the sample is only available in limited quantities. A higher brilliance neutron source would facilitate the realisation of all the further experiments suggested in this chapter. Moreover, neutron experiments should be extended to more kinds of spider silks, as it has already been done with X-rays.

Sample:

Obtaining larger quantities of spider silk appears to be extremely difficult from a practical point of view as silk must be collected from an increasing amount of spiders and only dragline collection has really been standardised. Handling of larger quantities of silk for a successful neutron scattering experiment becomes also increasingly difficult in terms of packing and fibre alignment.

The feasibility of isotopic replacement should, however, be considered in the future. ^{13}C labelling was for instance already performed for solid-state NMR experiments on spider dragline silk[67] for a comparable sample mass. For neutron scattering techniques, it would be more interesting to perform ^{2}H labelling.

Diffraction:

The observation and characterisation of the superlattice peak could possibly be improved, with more extensive experiments on dried silk using the improved area detector now installed at the D19 instrument. A further verification of the model that the superlattice peak corresponds to the repeating chain unit in the short-range order domain would imply that the WANS technique can probe these domains via this unique reflection. This would be an attractive alternative to the difficulties of separating the crystalline and short-range contributions in high resolution WAXS patterns. Combined with the possibility of isotopic replacement, the WANS technique appears therefore as a unique tool to complete our vision of this less well known, but of great importance, interface domain.

Spectroscopy:

In the future, it will be of importance to improve the humidity control on cryostated environments. The analysis of existing data could also be pushed further and it will be important to make the link with the structural information. It will also be necessary of exploiting different orientations of the fibres with respect to the plane of the detectors. Possibly, higher energy neutrons (thermal neutrons) would give access to a different energy scale.

Vibrations have not been analysed in this thesis, but a quantitative analysis might be possible along the line shown by Papanek et al.[68] for the analogue case of Nylon. Related studies on dynamics in biological materials have for instance also been done by Müller et al. [64, 69, 70] for the case of cellulose.

As a more distant possibility, *in-situ* stretching might be envisaged. A computer controlled tensile machine for such type of experiments has actually been developed in the group of Martin Müller (physics department, University of Kiel, Germany) but not yet applied to spider silk.

Perspectives

Source de neutrons :

Le principal facteur limitant commun à toutes les expériences de diffusion des neutrons est la brilliance de la source (définie comme l'intensité reçue par unité de temps par angle solide par section-efficace par intervalle d'énergie). Ceci est particulièrement bien illustré par toutes les expériences effectuées sur la soie d'araignée, pour lesquelles l'échantillon n'est disponible qu'en quantités limitées. Une source de neutron de plus haute brilliance faciliterait la réalisation de toutes les prochaines expériences suggérées dans ce chapitre. De plus, les expériences de neutronique pourraient être étendues à plusieurs type de soies d'araignées, comme cela a déjà été réalisé avec les rayons X.

Echantillon :

Il ressort que l'obtention de plus importantes quantités d'échantillon serait extrêmement difficile d'un point de vue pratique, étant donné que la soie doit être collectée sur un nombre croissant d'araignées et que seule la collecte du fil de traîne a été standardisée. Manipuler de plus grandes quantités de soies en vue d'une expérience réussie de diffusion des neutrons devient par ailleurs de plus en plus difficile en terme de regroupement et d'alignement des fibres.

La faisabilité du remplacement isotopique devrait néanmoins être considérée à l'avenir. Le marquage au ^{13}C a par exemple déjà été réalisé pour des expériences de RMN du solide sur le fil de traîne de l'araignée[67] sur une quantité d'échantillon comparable. Pour les techniques de diffusion neutronique, il serait plus utile d'effectuer un marquage au ^{2}H.

Diffraction :

L'observation et la caractérisation du pic hors réseau pourraient potentiellement être améliorées, à l'aide d'expériences plus poussées sur la soie sèche utilisant le détecteur couvrant une plus grande surface désormais installé sur l'instrument D19. Une nouvelle vérification du modèle supposant que le pic hors réseau correspond bien à un motif répété dans le domaine ordonné non-cristallin entraînerait que la technique de diffraction des neutrons permet de sonder ces domaines via une réflexion unique. Ceci serait une intéressante alternative aux difficultés rencontrées pour séparer les contributions cristallines et ordonnées non-cristallines sur les clichés à haute de résolution de diffraction des rayons X. Associée avec la possibilité du remplacement isotopique, la technique de diffraction des neutrons se

révèle en conséquence comme un outil unique pour compléter notre vision de ce domaine situé en interface, méconnu mais de grande importance.

Spectroscopie :
A l'avenir, il sera profitable d'améliorer le contrôle des conditions d'humidification dans les milieux cryostatés. L'analyse des données disponibles peut aussi être continuée et il sera important de faire le lien avec les informations structurelles. Il sera aussi nécessaire d'user de différentes orientations des fibres par rapport au plan des détecteurs. On peut envisager l'utilisation de neutrons de plus hautes énergies (neutrons thermiques) afin d'accéder à une gamme d'énergie différente.

Les vibrations n'ont pas été analysées dans cette thèse, mais une analyse quantitative serait réalisable suivant la procédure montrée par Papanek et al. [68] pour le cas comparable du Nylon. Des études similaires sur la dynamique de matériaux biologiques ont par exemple été effectuées par Müller et al. dans le cas de la cellulose.

En guise de perspective plus éloignée, l'étirement *in-situ* peut être envisagé. Une cellule de traction contrôlée par ordinateur pour de telles expériences a d'ailleurs été développée dans le groupe de Martin Müller (département de physique, université de Kiel, Allemagne) mais pas encore appliquée à la soie d'araignée.

Appendix I: list of neutron experiments

In the following, an exhaustive list of the neutron experiments with spider silk is given. This document is meant to provide an overview of the available data in case a further analysis is carried out. It has to be completed with the log files of the corresponding experiments, and is addressed to someone used to neutron experiments at the ILL. The format of the information, when available, is as follows:

Instrument / wavelength / sample environment / experiment number / date / run numbers / reactor cycle

- *experiments performed*

All these fields are not systematically filled.

Experiments prior to the start of the PhD project:

These experiments were performed with samples smaller than the ones available for the PhD project, with fibres slightly less well aligned.

IN16 / TEST / April 2001 (start Apr. 19, 2001) / runs 963-968 / cycle 2001-1

- 6mg test sample in flat slab at 45 deg. elastic scans
- empty can run 963 + later empty can over wider T-range: run 989
- spider silk cooling 3min./point: run 964: 1.3K -> 150K in 60 min.; run 965: 150K -> 310K in 270 min.

IN10 / TEST / June 2001 (start June 22, 2001) / runs 11598-11637

- 6mg test sample in flat slab

IN16 / 8-04-254 / February 2002 (start Feb. 19, 2002) / cycle 2002-1 / runs 3763-3840

- first dedicated sample for neutron experiments from Oxford
- sample mass of about 60mg, delivered on slide frame, transferred to a construction of 3 Al rods to suspend the fibres
- start with sample after storage in D2O atmosphere (about 4 days): runs 3771-3801
- pumping on sample (during #3802)
- soak sample in D2O (before run 3813, do not pump)
- soak sample in H2O (before run 3835)
- pump on sample (before run 3836)

IN6 / 8-04-254 / March 2002 (start March 4, 2002) / runs 550-663

- start with sample after storage in D2O atmosphere, then dry in-situ, soak in H2O
- same sample as IN16 part of 8-04-254
- sample in cylindrical container -> problems with gas background in container

D19 / TEST-678 / April-May 2002 (start May 29, 2002, 12 days) / cycle 2002-2 / runs 423895-426316

- same sample as for 8-04-254
- fibres moved more closely together compared to 8-04-254 to form more dense fibre bunch for diffraction
- one D2O and one H2O humid pattern each (D19 air flow humidity chamber), ambient temperature

IN16 / TEST-769 for HERCULES / April 2003 (Start Apr. 8, 2003) / cycle 2003-1 / silk runs after HERCULES session

- HERCULES runs 7094 - 7107
- silk runs 7108-7109
- old (i.e.60mg) silk sample sealed in ambient air

Spectroscopic experiments during the PhD project:

All spectroscopic experiments listed below have been performed on the 150mg *nephila eludis* spider silk sample, placed on an aluminium frame (3 cm high, fiber bundle 15 mm wide), received from the Zoology Department, University of Oxford, U.K. (group of Fritz Vollrath). On each IN6 and IN16, the specific spider silk sample containers have been used. The fibre axis is vertical, except on IN16 for exp. 8-04-331.

IN6 / 5.1A / cryostat / 8-04-287 / July 2003 (start Mon., July 14) / runs 7814-7893 / reactor cycle 032 (#135)

- dry sample (in vacuum)
- humid H_2O sample : soaked, taken out, cleaned from droplets with handkerchief, then stored in dessicator for up to 10h
- humid D_2O sample : soaked, taken out, cleaned from droplets with handkerchief , then stored in dessicator for up to 5h

IN16 / 6.27 A / cryofurnace / 8-04-287 / July 2003 (start Mon., July 21) / runs 8940-8993 / reactor cycle 032 (#135) (until end of cycle)

- native sample
- humid H_2O sample : soaked, taken out, cleaned from droplets with handkerchief, then stored in dessicator for up to 3h
- humid D_2O sample : soaked, taken out, cleaned from droplets with handkerchief , then stored in dessicator for up to 15h

IN16 / 6.27 A / cryofurnace / INTER-59 / November 2003 (start Mon., Nov. 17) / runs 9640 – 9675 / reactor cycle 033 (#136) (until end of cycle)

- humid D_2O sample : stored for long time (2/3 days) in dessicator, never soaked

IN10B / KCl200 / cryofurnace / 8-04-347 / June 2004 (start June 3) / runs 16900-16907 / reactor cycle 042 (#138) (until end of cycle)

- humid H_2O sample : stored in dessicator at least over night, never soaked, dried in-situ during experiment

IN16 / 6.27A / cryofurnace / 8-04-331 / March 2004 (start March 25 after HERCULES) /runs 10154-10318 / reactor cycle 041 (#137)

- experiment with different orientation, i.e. the fibres being in the horizontal scattering plane
- Start experiment (runs 10154-10178): Sample humid by storage during about 2 days in D_2O dessicator
- sample then dried in-situ (runs 10179-10188)
- then, troubles using the new sample cane

IN6 / 5.1A / cryostat / 8-04-331 / May-June 2004 (start May 30) / runs 12767 – 12859 / reactor cycle 042 (#138)

- Start experiment (runs 12767): Sample humid by storage (at least over night) in D_2O desiccator (never soaked, sure about it)
- Then dried in-situ
- Then empty can

- troubles with H_2O humidified sample: possible ice peak, although it was humidified by storage in dessicator. It is assumed (no notes about it) that the sample was first soaked for full H/D exchanged and then not properly dried with handkerchief
- series of short in-situ pumping.

Small- and Wide-Angle Neutron Scattering experiments during the PhD project:
All experiments listed below have been performed on the 150 mg *nephila eludis* spider silk sample (D19, D22), or the 20 mg sample (D11, D16, D22), both received from the Zoology Department, University of Oxford, U.K. (group of Fritz Vollrath). The 150mg sample was the same as used for the spectroscopic experiments. The sample temperature was always ambient.

D16 / 9-11-965 / July 2003 / runs 42073 + 42076 + 42333-43545 / reactor cycle 032

- The sample is in the D19 humidity chamber, without the humidity level controller or probe.
- dried sample in dry air flow
- humid H2O, D2O, and intermediate ratios samples.

D22 / out of proposal, test beamtime / October 2003 / runs 36127-36172 / reactor cycle 033

- native samples (the 20 mg one and the 150 mg one) under atmospheric conditions
- several detector distances, going from small to very small angle.

D19 / 9-11-965 / October-November 2003 / runs 574727-575744

- humid H2O 150 mg sample
- humid D2O 150 mg sample
- humidity chamber was used, the humidity is set to 80% RH

D11 / 8-02-324 / May 2004 / runs 11533-11610 / reactor cycle 042

- The sample is in the D19 humidity chamber, without the humidity level controller or probe.
- dried sample in dry air flow
- humid H2O, D2O, and intermediate ratios samples.
- Beam size at sample defined by a 5mm diameter circle aperture (the sample is thus fully illuminated)

D19 / 8-02-324 / july 2004. /runs 625054-632472 / reactor cycle 033

- humid D2O 150+20 mg samples (both fixed together)
- humidity chamber was used, humidity set to 80%

Appendix II: building the crystalline models

The aim of this section is to describe precisely how the models used for the simulations are built, so that it can be easily reproduced. Before doing so, it is highly recommended to read the original articles from Marsh et al. [16] and from Arnott et al. [17]. For a review, see Fraser et al. [23]. The programs used are MS Modeling v3.0 (Accelerys) and Cerius^2 v4.6 (Accelerys). It is reminded that help menus can always been obtained, with the Cerius^2 program, by a simple right click on any menu, button or field. It is for instance useful to identify the fields mentioned in the following appendix.

Building the Marsh model:
In the article from Marsh et al. [16], the chain axis corresponds to the *b* axis. A transformation is therefore required to get the chain axis along the *c* axis. Not only the atomic positions are changed, but also the symmetry operators, which do not correspond anymore to the definition of the $P2_12_12_1$ space group. It is possible with Cerius2, by contrast to MS Modeling, to choose the symmetry operators instead of selecting a space group. This is done in the "crystal builder" module of Cerius^2 by selecting the option "positions" for the symmetry description, and defining the following equivalent positions:
(x, y, z); (-x+1/2, y+1/2, -z); (-x, -y+1/2, z+1/2); (x+1/2, -y, z+1/2)
Note that it corresponds to the $P2_12_12_1$ space group equivalent positions where the operations on y and z have been exchanged. Defining a symmetry operator on Cerius^2 is done by writing the operator in the "add symmetry operator" field with exactly the following syntax (for instance for the second operator):
x-0.5, y+0.5, -z
The cell parameters are a = 9.44; b = 10.6; c = 6.95 (given in Angstrom, which is the default length unit on Cerius^2). The angles α, β and γ are 90° as it is an orthorhombic lattice type. Each atom has then to be added to the structure, with the positions given in Table 5 in fractional co-ordinates. With Cerius^2, the option "ABC" in the co-ordinates system field specifies the fractional coordinates system.

Table 5 Atomic fractional co-ordinates for the Marsh model (from Table 3 in [16], from which the original (X, Y, Z) are transformed into (x=X, y=-Z, z=Y)). a = 9.44; b = 10.6; c = 6.95 (Å). Equivalent positions: (x, y, z); (-x+1/2, y+1/2, -z); (-x, -y+1/2, z+1/2); (x+1/2, -y, z+1/2)

	Residue I					Residue II				
Atom	C'	O	N	αC	βC	C'	O	N	αC	βC
x	0.328	0.197	0.404	0.340	0.340	0.422	0.553	0.346	0.410	0.410
y	-0.514	-0.514	-0.478	-0.434	-0.291	-0.486	-0.486	-0.522	-0.566	-0.709
z	0.676	0.676	0.824	0.002	0.002	0.176	0.176	0.324	0.502	0.502

Once this is the done, the "build crystal" operation can be performed, and the complete structure with eight residues per unit cell is obtained. Note that the hydrogen atoms are missing. The easiest way to add the hydrogen atoms is to use the MS Modeling program. A model can be transferred from one program to another using a compatible file format, for instance the .msi file format. Once on MS Modeling, the user have to select the atoms on which hydrogen atoms have to be added, and use the "adjust hydrogen" in the "Modify" menu. Note that the operation has to be performed only on the nitrogen atom (one hydrogen atom will be added), on the *alpha*-carbon of the peptide chain (one hydrogen atom will be added) and on the *beta*-carbon of the methyl side-group (three hydrogen atoms will be added). If the "adjust hydrogen" option is used on the C', and if the C' = O bound was not defined as a

double bound using the appropriate option (available on both MS Modeling and Cerius^2), the program will add a hydrogen atom while their should be none. Once all and only the appropriate hydrogen atoms are added, the model can be exported back to Cerius, using for instance the .msi file format.

Building the Arnott model:
The construction of the Arnott model follows the instruction of the original article [17]. It is suggested to read this article carefully and to understand the statistical model used by Arnott et al. before following the instructions here given.
In the "crystal builder" module of Cerius^2, a symmetry description having the following equivalent positions is chosen:
(x, y, z); (-x, -y, z+1/2)
which corresponds to the $P2_1$ space group, "monoclinic-c" subgroup (or $P112_1$). The cell parameters (in Angstrom) are a = 4.734; b = 10.535; c = 6.89. The angles α, β and γ are 90° as it is an orthorhombic lattice type. The next operation is to add each atom. The positions are given in Table 6 in Cartesian coordinates. With Cerius^2, the option "XYZ" in the co-ordinates system field specifies the Cartesian coordinates system. The unit is the angstrom. The atomic co-ordinates of residue I are obtained from Table 3 in [17]. Residue II is deduced from Residue I by the operation (X+a/2, Y+b/2, z+ΔZ/c), where ΔZ has a value of 0.69Å and is defined in [17] as the shift along the z-axis between the molecules of two sheets. Residue III and IV correspond to the next (antiparallel) chain and is deduced from Residue I and II by the operation (X+a, -Y, -Z-2w+c), where 2w has a value of 2.67 Å and is defined in [17] as the shift between two "half-molecules".

Table 6 Atomic cartesian co-ordinates in Å for the Arnott model. Residue I corresponds to Table 3 in [17]. Residue II is deduced from Residue I by the operation (X+a/2, Y+b/2, z+ΔZ/c). Residue III and IV are deduced from Residue I and II by the operation (X+a, -Y, -Z-2w+c). a = 4.734; b = 10.535; c = 6.89; ΔZ = 0.69; 2w=2.67.

	Residue I						
Atom	C'	O	N	H (on N)	αC	H (on αC)	βC
X (Å)	-0.49	-1.7	0.33	1.3	-0.14	-1.21	0.24
Y (Å)	-0.13	0.13	0.13	-0.1	0.79	0.7	2.28
Z (Å)	3.56	3.53	2.56	2.58	1.34	1.27	1.37
	Residue II						
X (Å)	1.877	0.667	2.697	3.667	2.227	1.157	2.607
Y (Å)	5.1375	5.3975	5.3975	5.1675	6.0575	5.9675	7.5475
Z (Å)	3.6543	3.6243	2.6543	2.6743	1.4343	1.3643	1.4643
	Residue III						
X (Å)	4.24	3.03	5.06	6.03	4.59	3.52	4.97
Y (Å)	0.13	-0.13	-0.13	0.1	-0.79	-0.7	-2.28
Z (Å)	0.66	0.69	1.66	1.64	2.88	2.95	2.85
	Residue IV						
X (Å)	6.607	5.397	7.427	8.397	6.957	5.887	7.337
Y (Å)	5.3975	5.1375	5.1375	5.3675	4.4775	4.5675	2.9875
Z (Å)	0.7543	0.7843	1.7543	1.7343	2.9743	3.0443	2.9443

I did not find a module on Cerius^2 or MS Modeling to deduce automatically the Residue II, III and IV by giving the described operations. The symmetry description cannot be used, as the symmetry operators have to form closed group, which is not the case of the operations (X+a/2, Y+b/2, z+ΔZ/c) and (X+a, -Y, -Z-2w+c). Thus, the co-ordinates in Table 6 were

typed for all the atoms listed. One has to be especially careful about typing mistake during this operation. The result will anyway, even without mistakes, look like a molecule which could not exist, as each up-pointing half chain is superimposed to a down-pointing half chain (see the description of the statistical model in [17] or in chapter 2). Each atom has therefore too many neighbours, as it is also close to some of the atoms from the other half chain. By default, the program calculates bounding every time an atom is sufficiently close to another. Once the model is built, it is exported to MS modeling, on which bounds can be selected one-by-one and eventually deleted. The forbidden bounds between the half-chains of the same chain site are thus removed. Once this is performed, the missing hydrogen atoms of the methyl group can be added, following the procedure already described for the Marsh model. The model can then be exported back to Cerius^2, on which the simulations are performed.

Simulations:
Fibre diffraction patterns can be simulated from a crystalline model using Cerius^2. The module can be found in the "Analytical 1" menu card deck (by default, "Builders 1" is open), menu "crystal builder", panel "Calculate Crystal Diffraction", display as "fiber". The intensities of each reflection can be obtained with the "output preferences" panel. Using the pattern simulation menu is quite easy and straightforward, thus no detailed description is necessary. All the required parameters (crystallite size, orientation, etc.) are given in Chapter 2 - Simulation of fibre diffraction patterns.

Appendix III: using Matlab for spectroscopy analysis

Several programs already exist at the ILL for the different steps of the analysis. Some figures shown were obtained from LAMP or IDA programs. It was also chosen for this project to perform the analysis by writing the required programs using the Matlab environment. Because Matlab can handle very big matrices (datasets), it has the advantages to allow any step to be performed with the same interface, to control precisely every single operation and to be able to modify these operations easily. The difficulty rises from the total length of the operations performed and their readability. This section therefore is meant to clarify this analysis, by providing an overview and several examples.

The different sections of the appendix follow the chronological order of the analysis and are:
- Sorting raw data in a suitable file format
- Reading data with Matlab and data pre-treatment (normalisation, grouping of spectra)
- Visualisation of almost raw data
- Mathematical operations (convolution, fitting)
- Visualisation of treated data

Sorting raw data: raw data obtained from ILL file formats are not suitable for a simple reading routine. Moreover each instrument has its specific format. For a detailed description of the format for IN6, IN10 and IN16 instruments, one shall for instance refer to the second appendix of the SQW manual, available at the ILL. In the example given below, three scripts written with the awk processing language are used in order to organise data files from the IN16 instrument into column files. The scripts are given here without further explanation, as it would require an introduction to the ILL instrument file format too long here.

Extract.sh

```
#!/bin/bash
#
# Extract detectors and monitor from IN10 raw data ("punch card")
# files into separate column wise ASCII files.
# Give first and last run number without leading zero as arguments
#
for ((ll=$1;ll<=$2;ll++)); do
echo Extracting run number 0$ll
./in10dump.sh 0$ll
wc -l 0$ll.dat > lines.dat
read nolines junk < lines.dat
echo Number of lines 0$ll.dat: $nolines
./splitdet.sh 0$ll
{
for ((mm=1;mm<=$nolines;mm++)); do
read a b c
echo $c >> 0$ll.d$a
done
}<0$ll.sort
done
rm *.d*
```

splitdet.sh

```
# is called by extract.sh
awk -v ii=1 -v jj=0 -v det=0 \
'{ if ($1=="#") {ii=1; jj=0; det++} \
else {printf("%2i %5i %14.2lf\n",det,jj,$1); jj++} }' $1.dat > $1.sort
```

in16dump.sh

```
# extract detector intensities from IN16 Doppler scan raw data file
# input is filename ("numor")
awk -v ii=1 -v jj=1 -v det=0 \
'($1=="SSSSSSSSSSSSSSSSSSSSSSSSSSSSSSSSSSSSSSSSSSSSSSSSSSSSSSSSSSSSSSSSSSSSSSSSSSSSSSSS") \
 { ii+=1; det+=1; jj=NR; printf("# detector %2i\n",det); }; \
 ((NR>(jj+3)) && (NR<=(jj+28)) && (det>0)) {for (k=1;k<=10;k++) {printf("%8i\n",$k)};} \
 ((NR==(jj+29)) && (det>0)) {for (k=1;k<=6;k++) {printf("%8i\n",$k)};}' $1 > $1.dat
```

Figure 57 example of an awk script used to convert raw data files from the IN16 instrument into ASCII column files. The very long lines containing several time the "S" letter, in extract.sh and in16dump.sh, are written smaller in order to fit the page size.

To use these scripts, it is simply necessary to write them into a text file, make them executable, and run them with for instance the following command line on a Unix or Linux platform:

> ./extract.sh 10283 10288

Where "10283" is the first run number and "10288" the last run number (all of the runs in between being also treated). Note that in the example, the original files actually contain one "0" at the beginning of the file name which are added by the script. The script has to be edited accordingly to the treated data, for instance if there are two "0" instead of one in the run numbers.

Matlab program overview: In order to minimise the computing time when performing slight modifications, the program is divided in three main modules (see Figure 58), each of them taking approximately the same amount of time to execute. Several versions of each module exist and were used, allowing a few operations to be slightly changed. For instance, the resolution data can be fitted by a Gaussian, or a Lorentzian, or a sum of functions. The three main modules are called "data_treatment_050921_*x*_*y*.m" where *x* is the step (1, 2 or 3) and *y* the eventual version number of this main module.

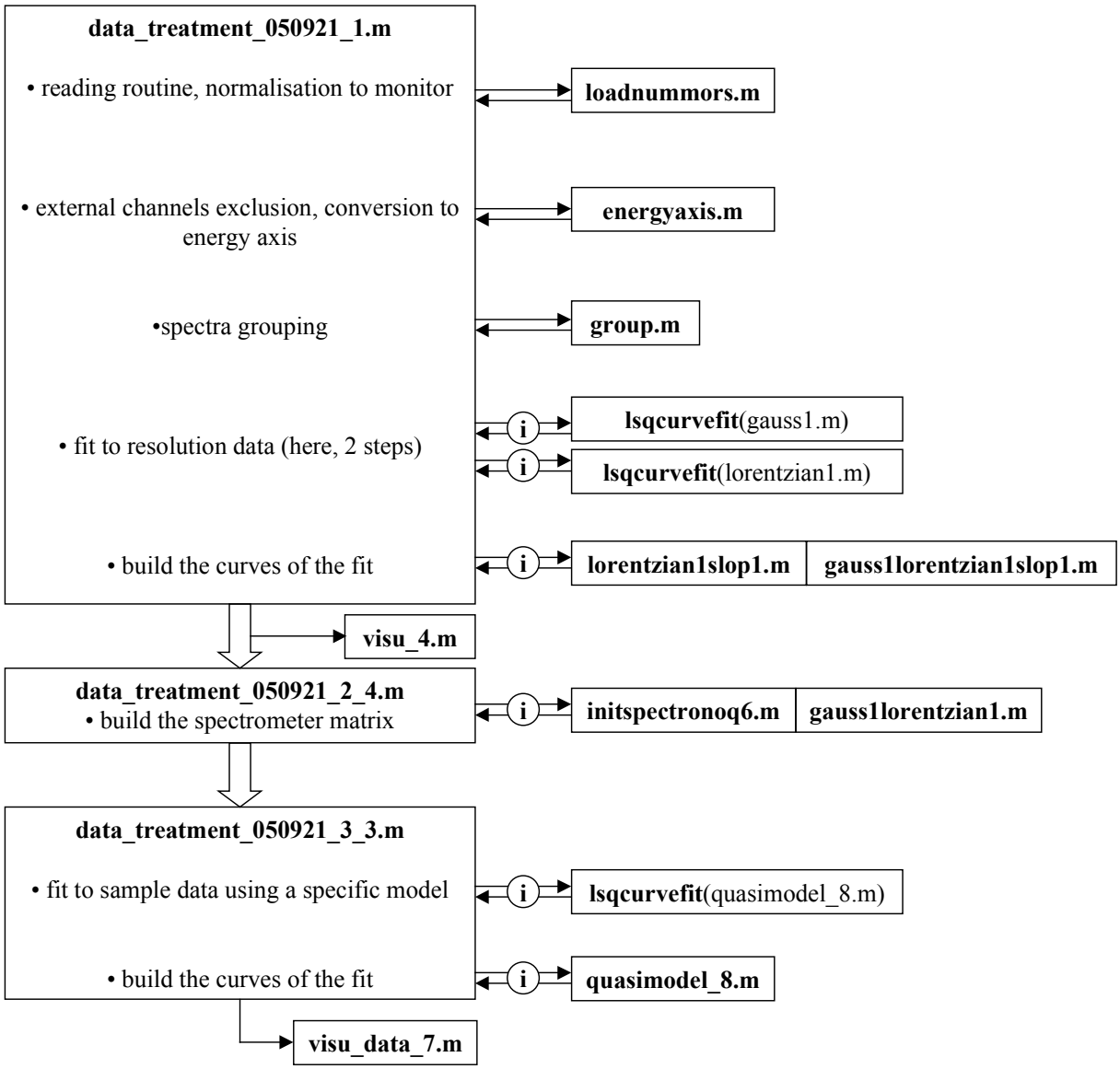

Figure 58 flowchart of the fitting program, showing the different modules used and how they are called and organised with respect to each other. The double arrow represents a single call of a secondary module, while the double arrow with the letter "i" inside represents a call of a secondary module within an iterative procedure. This chart shows the specific example of the sequence "data_treatment_050921_1.m", "data_treatment_050921_2_4.m" and "data_treatment_050921_3_3.m", while different sequences are possible depending on the model chosen to fit the data. With a different sequence, the overall structure might slightly change.

Reading routine: The first main module calls the reading routine "**loadnummors.m**". This function requires two arguments, the first and the last channel numbers (Abbr: nummors) of a sequence. Every nummor between these two values will be read and added to the returned matrix. Note that the variables created in a secondary module (such as "totalchannels", "columns" or the matrices "A", "B" and "C" here) are not conserved in the main modules. The version here shown is for IN16 instrument and performs the normalisation to monitor immediately.

loadnummors.m

```
function y = loadnummors(firstnummor,lastnummor);
%
% open, reorganise and normalise several datas to monitor
% read file produced by in16dump.sh
%
% 1-> 20 are wide angle (from lower to higher angle)
% 21 -> 22 are small angle (from lower to higher angle)
% 23 is monitor
% 24 is the 160 channels diffraction data (not kept)
%
totalchannels=256;
columns=23;
C=0;
%
% open the file after concatenation of its name
%
for nummor = firstnummor:lastnummor
   A=load(['00' num2str(nummor) '.sort']);
   j=1;
   for j=1:columns
      i=1;
      for i=1:totalchannels
         B(i,j)=A((j-1)*totalchannels+i,3);
         i=i+1;
      end;
      j=j+1;
   end;
   % normalisation to monitor
   for j=1:columns-1
      B(:,j)=B(:,j)./B(:,23);
   end;
   C = C+B/(1+lastnummor-firstnummor);
end;
%
y=C(:,1:1:columns);
```

Conversion to energy: On the IN16 instrument, there is a simple linear relation between the energy and the channels, which are dispatched homogeneously.

energyaxis.m

```
function y = energyaxis(realchannels);
%
% complicate formula to get the energy scale
%
% it assumes an original channel size of [1:256]
% it assumes -Emax to Emax range (micro-eV) (has to be symetric, else rewrite formula)
%
% just requires the channel range for which this energy range is meaningfull
%
Emax=14.5;
totalchannels=1:1:256;
y=(2*Emax*(totalchannels-(realchannels(1)-1))/length(realchannels))-Emax;
```

The channels are for IN16 dispatched homogeneously, which renders the conversion easier than for data from IN10b or IN6. On IN10b, different runs can have different energy steps. On IN6 data, energy steps are not distributed regularly, thus an interpolation is necessary in order to obtain a regular grid. The fitting and convolution routines described here require such a regular grid. Moreover, this step of converting the X-axis to energy axis is also suitable to

remove the "bad" channels (determining bad or broken channels is simply done by visualising the raw data). This is done directly in the first main module (to be described later) but does influence the conversion step. The chosen "real channels" range is therefore a required argument sent to the function "**energyaxis.m**" here shown (for IN16 data).

Grouping routine: Grouping several spectra together is useful to increase the statistic before a fitting routine, to facilitate the visualisation of the data and to exclude one or several spectra. The routine "**group.m**" requires three arguments: the matrix containing the data (using the format provided by **loadnummors.m**), an integer giving the number of groups, and a vector which will define the spectra to be grouped. "**group.m**" allows groups of any size and composed of any number of spectra to be formed, provided that the eventually skipped spectra correspond to a group separation. For instance, the routine can produce a matrix of two groups made of the two spectra 1 and 2 and of the three spectra 4, 5 and 6 (excluding spectra 3, the notation of the vector being [1 2 4 6]). It cannot, however, make a matrix with a group made of the two spectra 1 and 3 (excluding spectra 2 in a single group). If such a grouping is necessary, the routine simply has to be rewritten. The format of the vector is as follows: [3 4 7 7 8 11] would produce a matrix of three groups, containing spectra 3 to 4 in group 1, spectrum 7 in group 2, and spectra 8 to 11 in group 3.

Fitting routine: The fitting routine was performed using the in-built Matlab function **lsqcurvefit**, based on the least difference fitting method. The required parameters are a model function, the starting values, vectors describing the X- and Y-coordinates. The boundary conditions are required depending on the algorithm used and optional function specific parameters such as the maximum number of iterations or the definition of the algorithm to be used can be specified. For details, see the Matlab help on this function. Examples are provided in next parts.

group.m

```
function y = group(data,nbgroup,spectra)
%
% spectras will be the list of the first and last number of spectra
% for each group. It has a variable size, dependant of nbgroup >= 1
%
% example :
% b=[3 4 7 7 8 11];
% A3=group(A2,3,b);
%
newspectras=ones(size(data,1),1);
for i=1:nbgroup;
   first=spectra(2*i-1);
   last=spectra(2*i);
   if(first==last);
      newspectras=horzcat(newspectras,data(:,first));
   else;

newspectras=horzcat(newspectras,(sum(data(:,first:last)')./(1+last-
first))');
   end;
end;
newspectras(:,1)=[];
y=newspectras;
```

Simple model function: The user can choose any self-written model function to which the data has to be fitted. Several short modules are written for this purpose, making it easy to switch for instance from a fit to a Gaussian to a fit to a Gaussion plus flat background. Obviously

each model function requires specific parameters, and the user has to keep in mind in which order they are listed in the corresponding module. The usual procedure during this project was to use normalised function (Gaussians or Lorentzians) characterised by three parameters in the following order: intensity, sigma, x_0 position at maximum. Background (flat or slope) required one or two supplementary parameters usually provided at the end. The example of "**lorentzian1slop1.m**", one module among others used in the first main module, is here shown. This module corresponds to the sum of a Lorentzian and a slope background.

lorentzian1slop1.m

```
function y = lorentzian1slop1(b,x)
% lorentzian + slop background
%
% b(1,2,3) are parameters for lorentzian
% intensity, sigma, x0
% the slop background is b(4)*x + b(5)
%
y = b(4)*x + b(5) + ((b(1)*b(2)/(2*pi)) ./ ((x-b(3)).^2 + (b(2)/2).^2));
```

These short modules are also used when building the tables of values corresponding to the function fitted to the data, necessary for visualisation.

First main module: The first tasks of the first main module are illustrated in the flowchart (Figure 58) with the example of "**data_treatment_050921_1.m**". IN16 data are read, normalised, reorganised and regrouped, using the modules previously described. The analysis of data corresponds especially in a deconvolution of the data and the resolution of the instrument. However the measurements of the resolution are slightly noisy and that noise might highly influence convolution or deconvolution processes. It therefore might be better to estimate a resolution function fitted to the measured resolution. That is the objective of the fit performed at this stage. Several fitting functions had been used. It is noted that a simple function (Gaussian or Lorentzian) might provide a fit apparently satisfying. The quality of the fit in the important region of the quasielastic broadening is, however, not reflected in the estimation of residuals used by fitting routines. It appears that a weak, broader contribution is necessary to fit this area. However, when the fit is performed with a function made of two contributions (a broad and a narrow one), it appears that the initially broad contribution will be used by the algorithm to fit the noise in the highly intense elastic peak. Thus, "**data_treatment_050921_1.m**" uses an approach in two steps (two main loops, the loop being performed over the different groups of spectra). First of all a Gaussian is fitted to the limited area of the elastic peak. Then, a Lorentzian is fitted to the residual part, using only the points in the broadening area. The efficiency of the operation is controlled mainly by visualisation. For this purpose, it is necessary to build the tables of values corresponding to the fitted functions, and to the different contributions of these fitted functions. Short modules, similar to the ones used as simple model functions, are used at this stage. For illustration, in the following module "**data_treatment_050921_1.m**", "lorentzianA1" is build using the "**lorentzian1.m**" module, and is the vector corresponding to the Lorentzian contribution fitted to the data within the matrix "A1", containing the resolution for the dry silk. The variable "lorentzianA1" is during the loop procedure extended to a matrix containing the six vectors, corresponding to the six groups of spectra.

data_treatment_050921_1.m

```
% realistic approach to convolution/fitting
% we separate this into several steps, making testing shorter
% first part is the fit of the resolution
%
clear all;
```

```
close all;
%
% define variables used
realchannels=3:1:254;
% open the 100 K dry silk data
%
A01=loadnummors(8944,8948);
%
% 290 K dry silk
A02=loadnummors(8955,8958);
%
% open the 20 K H2O humid silk data
A03=loadnummors(8965,8968);
%
% 290 K H2O humid silk
A04=loadnummors(8975,8978);
%
% create correct energy scale for choosen channels (see macro energyaxis for details)
EN=energyaxis(realchannels);
%
% remove unused channels
%
A01(255:256,:)=[];
A02(255:256,:)=[];
A03(255:256,:)=[];
A04(255:256,:)=[];
EN(255:256)=[];
A01(1:2,:)=[];
A02(1:2,:)=[];
A03(1:2,:)=[];
A04(1:2,:)=[];
EN(1:2)=[];
%
% GROUPING
%
%nbgroups=4;
%spectra=[1 4 8 11 12 15 16 19];
%
nbgroups=6;
spectra=[1 3 4 6 8 10 11 13 14 16 17 19];
%
A1=group(A01,nbgroups,spectra);
A2=group(A02,nbgroups,spectra);
A3=group(A03,nbgroups,spectra);
A4=group(A04,nbgroups,spectra);
% nbgroups = 19;
% A1=A01;A2=A02;A3=A03;A4=A04;

% FITTING
% RESOLUTION
% first step : the gaussian alone.
%
% fitting routine

% We use the Medium-Scale Algorithm (LargeScale set to off), better to stay
% at local minimum if we start with realistic starting conditions.
options=optimset(optimset,'LargeScale','off','MaxIter',1000,'MaxFunEvals',500,'display','off');

% Fitting just the gaussian and create the functions

for i=1:nbgroups;
   % For now, we have always the same starting values, but this might be
```

```
    % changed
    StartGauss1(:,i) = [0.01,0.5,0];
    StartGauss3(:,i) = [0.01,0.5,0];

    % Here is the fitting routine itself
    param1A1(:,i) = lsqcurvefit(@gauss1, StartGauss1(:,i), EN', A1(:,i), [], [], options);
    param1A3(:,i) = lsqcurvefit(@gauss1, StartGauss3(:,i), EN', A3(:,i), [], [], options);

    % Once the fit is performed, we build the function with the parameters obtained.
    gaussA1(:,i) = (gauss1(param1A1(:,i),EN))';
    gaussA3(:,i) = (gauss1(param1A3(:,i),EN))';
end;

% second step : add a slope background and a lorentzian broadening.
% We will fit these only to the DIFFERENCE of signal - gaussian
% over a relevant area (not including the elastic peak)
%
% All of this is done to allow the lorentzian to fit the broadening instead
% of the fluctuations at elastic position.

% Relevant area is : 1 to LB and RB to 252; (Left Broadening and Right, in channel number)
LB = 114;
RB = 139;

broadEN = [EN(1:LB) EN(RB:252)];

for i=1:nbgroups;
    diffA1(:,i) = A1(:,i) - gaussA1(:,i);
    diffA3(:,i) = A3(:,i) - gaussA3(:,i);
    broaddiffA1(:,i) = vertcat(diffA1(1:LB,i),diffA1(RB:252,i));
    broaddiffA3(:,i) = vertcat(diffA3(1:LB,i),diffA3(RB:252,i));

    StartLS1(:,i) = [0.001,5,0, 0,1e-7];
    StartLS3(:,i) = [0.001,5,0, 0,1e-7];

    param2A1(:,i) = lsqcurvefit(@lorentzian1slop1, StartLS1(:,i), broadEN', broaddiffA1(:,i), [], [], options);
    param2A3(:,i) = lsqcurvefit(@lorentzian1slop1, StartLS3(:,i), broadEN', broaddiffA3(:,i), [], [], options);

    lorentzianA1(:,i) = (lorentzian1(param2A1(1:3,i),EN))';
    lorentzianA3(:,i) = (lorentzian1(param2A3(1:3,i),EN))';

    paramA1(:,i) = vertcat(param1A1(:,i),param2A1(:,i));
    paramA3(:,i) = vertcat(param1A3(:,i),param2A3(:,i));

    fitA1(:,i) = (gauss1lorentzian1slop1(paramA1(:,i),EN))';
    fitA3(:,i) = (gauss1lorentzian1slop1(paramA3(:,i),EN))';
end;

% Now, run a visu macro or data_treatment_050921_2.m
```

Second main module: The purpose of this section is to prepare the convolution products. The simplest way to perform a numerical approximation of a convolution product between a model function and the resolution function (an integral over the infinite x-axis range) is to multiply the vector corresponding to the model function by the so-called spectrometer matrix. Two ways of building this spectrometer were tested during this project. One can use directly the resolution data points, possibly after some pre-treatment is performed, such as removing a flat background for instance. The other possibility is to use the values of the resolution function fitted to the data, thus using an analytical description of the resolution function. "**data_treatment_050921_2_4.m**" illustrate this.

data_treatment_050921_2_4.m

```
% see part one for explanation
%
% A1 is 100K dry silk, A2 is 290K dry silk, A3 is 20K H2O humid silk, A4 is
% 290K H2O humid silk.
%
% Now that fit to resolution is done, we build the spectrometer matrix
% On this step, we use initspectro #6 : removing the slop bg when building the spec. matrix

clear mm1 mm3

for i=1:nbgroups;
    % now building the spectrometer matrix
    % This way, the parameters of the fit for the corresponding data set
    % (cold sample) are entered. The initspectronoq function will use a
    % specific function (depending on the number, use the same function
    % as used for the fit of the resolution !) and enter the results in the
    % spectrometer matrix.

    mm1(:,:,i) = initspectronoq6(EN, paramA1(1:6,i));
    mm3(:,:,i) = initspectronoq6(EN, paramA3(1:6,i));
end;
```

initspectronoq_6.m

```
function y = initspectronoq6(x, rp)
% Back to "old" method, removing the constant from the spec. matrix
%
% INITSPECTRO x q rp.
% Initialize spectrometer matrix
% x energy axis
% rp gaussian+lorentzian+slope Resolution Parameters
%
% Spectrometer matrix:
np=length(x);
mm=[np,np];
% Calculate spectrometer matrix:
  for i=1:np
   xi=x(i);
   for j=1:np
    xj=x(j);
    xij=xi-xj;
% PAY ATTENTION TO THIS SIGN
% we do xi-xj
% then the convolution will be performed by multiplying the result of this function by the data vector :
% convolution = y*data
%
% the other possibility, y'*data, would give the mirrored function f(-x)
% for our almost symmetric data, fitting data(x) with the corresponding
% f(-x) gives an almost correct result... Thus the mistake is hard to detect.
%
% note that the transposition of y may occur very easely depending how you call
% this function
%
    mm(i,j)=gauss1lorentzian1(rp,xij);
   end
  end
% return the matrix:
y=mm;
```

The specific "**data_treatment_050921_2_4.m**" module calls the "**initspectronoq_6.m**" which is meant to actually built the spectrometer matrix with this specific resolution function. It requires the energy axis on which the matrix has to be built, and the parameters from the fit. In this example, the resolution function corresponds to a narrow Gaussian for the elastic peak, a broad Lorentzian for the quasielastic area, and a weak slope background. This slope background has to be not used when building the spectrometer matrix. Indeed, this method of approximating a convolution product is efficient if the two functions have values very close to zero on the edge of the used area.

Third main module: The "deconvolution" procedure actually consists in fitting the convolution product of the resolution and of a model function with variable parameters to the data. As one of the functions is changing during the fit, the convolution product as to be recalculated every time. There are therefore as many convolution products (actually multiplication of a vector by a matrix) as there are iteration steps in each fit. This might seem like an extremely long calculation, however Matlab is efficient at handling such operations, thus the computation time is finally quite short. At this step is chosen which model will be used and with which parameters. The function called by the fitting routine performs this multiplication. It requires the variable model parameters which will be evolving with the fit. It also uses fixed parameters such as the spectrometer matrix and some arguments allowing the model to be changed slightly without changing the corresponding module every time. In the case of the third main module "**data_treatment_050921_3_3.m**", the model is quite simple and is calculated by "**quasimodel_8.m**". First a very narrow Lorentzian is used to estimate the delta function corresponding to the Elastic Incoherent Structure Factor (EISF). The peak position and the peak width are "fixed" parameters, which the fitting routine will not change, while the user can play with them in order to refine the model. The intensity of the "delta" function is a parameter refined by the fitting routine. Secondly a Lorentzian is added to this "delta" function and shall represent the quasielastic signal, thus all its parameters are refined by the fitting routine.

quasimodel_8.m

```
function y = quasimodel_8(b,x,mm,p,const)
%
% fitting done with a fixed spectrometer matrix for this group
%
% resolution is modeled gaussian+lorentzian+const
% data is modeled very narrow lorentzian (delta function of elastic line)
%  + lorentzian
% b(1,3) will be data lorentzian 1 paramters
% b(4) will be delta function intensity (sharp lorentzian)
%
% p.w and p.p will be delta function width and position (fixed)
%
% const.model will be the mean data value at highest and lowest energies
% const.resb will be the value at 0 of the slop bg from resolution
%
% parameters being 1.intensity, 2.line width and 3. x0 position

model = ((abs(b(4))*p.w/(2*pi)) ./ ((x-p.p).^2 + (p.w/2).^2)) ...
     + ((abs(b(1))*b(2)/(2*pi)) ./ ((x-b(3)).^2 + (b(2)/2).^2));

y = model*mm + const.model; % + const.resb;
```

The "convolution product" is performed with this model function and the spectrometer matrix (fixed parameter) previously calculated. The final function fitted to the data just requires a flat background to be added (but only once the convolution product is performed). This flat

contribution should ideally be a free parameter of the fitting routine, however, it appeared in the case of IN16 data that the very broad quasielastic signal was fitted mainly by this parameter, thus it as been fixed to the mean value at the extremes of the energy axis.

data_treatment_050921_3_3.m

```
% see part one for explanation
%
% A1 is 100K dry silk, A2 is 290K dry silk, A3 is 20K H2O humid silk, A4 is
% 290K H2O humid silk.
%
% Now that we have the spectrometer matrix, we perform the fit to the
% convoluted function
%
% on this version (#2), we use the function conv of matlab

clear resnom2 resnorm4 const2 const4 p2 p4 StartLDC2 StartLDC4 param3A2 ...
   param3A4 fitA2 fitA4 lorentzian1A2 lorentzian1A4 lorentzian2A2 lorentzian2A4

% We use the Medium-Scale Algorithm (LargeScale set to off), better to stay
% at local minimum if we start with realistic starting conditions.
options=optimset(optimset,'LargeScale','off','MaxIter',2000,'MaxFunEvals',1000,'display','on');

for i=1:nbgroups;
   % We now have to fit the sample data with a function using the
   % following parameters :
   % - the spectrometer matrix (resolution without slop bg)
   % - the model parameters
   % For each model, we will need a different function (pour l'instant)
   % This function return the product of model*mm (ie the model convoluted by the resolution)

   % This model is a "delta" function made with a very narrow lorentzian
   % + the lorentzian hopefully containing the relevant information.
   % + constant background added to the result of the convolution

   % COMMENT :
   % If this constant bg is set free, whatever the starting value, it has
   % high chance to be overestimated.

   % fixed parameters for the delta function and constant bg

   p2.w = 0.1;
   p2.p = 0;
   const2.model = 0.5 * (mean(A2(1:5,i)) + mean(A2(247:252,i)));
   const2.resb = paramA1(8,i);

   p4 = p2;
   const4.model = 0.5 * (mean(A4(1:5,i)) + mean(A4(247:252,i)));
   const4.resb = paramA3(8,i);

% keeping track ...


   StartLDC2(:,i) = [0.001,0.5,0 ...
            1];
   StartLDC4(:,i) = [0.001,5,0 ...
            1];

%    StartLDC2(5,i) = 0.5 * (mean(A2(1:5,i)) + mean(A2(247:252,i)));
%    StartLDC4(5,i) = 0.5 * (mean(A4(1:5,i)) + mean(A4(247:252,i)));

   i
```

```
%    param3A2(:,i) = lsqcurvefit(@(b,x)quasimodel_8(b,x,mm1(:,:,i),p2,const2(i)), ...
%   StartLDC2(:,i), EN, A2(:,i)', [], [], options);
%    param3A4(:,i) =
%    lsqcurvefit(@(b,x)quasimodel_8(b,x,mm3(:,:,i),p4,const4(i)), ...
%   StartLDC4(:,i), EN, A4(:,i)', [], [], options);

    [param3A2(:,i), resnorm2(i)] = lsqcurvefit(@(b,x)quasimodel_8(b,x,mm1(:,:,i), p2, const2), ...
        StartLDC2(:,i), EN, A2(:,i)', [], [], options);
    [param3A4(:,i), resnorm4(i)] = lsqcurvefit(@(b,x)quasimodel_8(b,x,mm3(:,:,i), p4, const4), ...
        StartLDC4(:,i), EN, A4(:,i)', [], [], options);

% we anyway use only the absolute value in quasimodel_8
    param3A2(1,i) = abs(param3A2(1,i));
    param3A4(1,i) = abs(param3A4(1,i));
    param3A2(4,i) = abs(param3A2(4,i));
    param3A4(4,i) = abs(param3A4(4,i));

    fitA2(:,i) = (quasimodel_8(param3A2(:,i), EN, mm1(:,:,i), p2, const2))';
    fitA4(:,i) = (quasimodel_8(param3A4(:,i), EN, mm3(:,:,i), p4, const4))';

    % next is function used for visualisation

    lorentzian1A2 = lorentzian1(param3A2(1:3,i),EN);
    lorentzian1A4 = lorentzian1(param3A4(1:3,i),EN);
end;
```

Visualisation: In such a long process, visualisation of the data at different steps is extremely helpful. Thus the visualisation module "**visu_4.m**" used at the intermediate state where the fit to the resolution is performed is given here. No legend is added to the figure as such a module is constantly edited in order to observe different functions. The latest commented lines provide an example of how the parameter values can be easily listed.

visu_4.m

```
% Visualisation of resolution gaussian
%
for i=1:nbgroups;
    figure(i);
    plot(EN,A1(:,i),'o',EN,fitA1(:,i),'-
',EN,lorentzianA1(:,i),'x',EN,gaussA1(:,i),'.');
    axis([-15 15 -1e-5 1e-3]);
end;
%tmp=param2A1;
%tmp(7:8,:)=1000*param2A1(7:8,:);
%tmp(4,:)=1000*param2A1(4,:);
%tmp'
```

The module "**visu_data_7.m**" for visualising the final fit of this continuous example is also here provided. It basically is the same thing as "**visu_4.m**" but also provide an example of how Matlab can be used for preparing pictures.
With this is given in this appendix a complete example of a spectroscopic data analysis as it was performed during this project. A warning should be added to the eventual user who would have access to the other version of the modules: One shall expect to have difficulties using a different sequence of main modules than the example here given. A safe approach would be to use these other modules as illustrations/suggestions of the other way the problems can be tackled, and in case these ways are needed, to rewrite everything that is not absolutely

clearly understood. Be aware that there were known bugs that were not corrected, especially in the early versions.

visu_data_7.m

```
% visu of data from data_treatment_050921_1.m and data_treatment_050921_2.m
% for fit result of convolution of resolution and model
%
% A1 is 100K dry silk, A2 is 290K dry silk, A3 is 20K H2O humid silk, A4 is
% 290K H2O humid silk.
%

close all;

% i select the group to show.
% Choose either the loop or fixed value by commenting.

%i=1;
for i=1:nbgroups;

figure(i);

H = plot(EN,fitA1(:,i),'-', ...
    EN,A2(:,i),'o', ...
    EN,fitA2(:,i),'--', ...
    EN,A4(:,i),'s', ...
    EN,fitA4(:,i),'--');

% fix axis range
axis([-15 15 -1e-5 3e-4]);

% labels title and properties
xlabel('Energy [\mueV]', 'FontSize', 18);
ylabel('Intensity [arb. units]', 'FontSize', 18);

% set the size of axis text (and more, gca = get current axes handles)
set(gca,'FontSize',20,'LineWidth',2);

%line thickness and colors
set(H(1),'LineWidth',2,'Color','k');
set(H(2),'LineWidth',1,'Color','r');
set(H(3),'LineWidth',2,'Color','r');
set(H(4),'LineWidth',1,'Color','b');
set(H(5),'LineWidth',2,'Color','b');

% legend configuration (has to be done after set(gca...))
L=legend('fit to dry silk res.','290K dry silk','fit','290K humid silk','fit','Location','NorthEast');
legend boxoff;
set(L,'FontSize',12,'FontWeight','bold');

% inset to see the top

axes('Position',[0.22,0.65,0.20,0.20]);
Hinset = plot(EN,fitA1(:,i),'-', ...
    EN,A2(:,i),'o', ...
    EN,fitA2(:,i),'--', ...
    EN,A4(:,i),'s', ...
    EN,fitA4(:,i),'--');
axis([-3 3 1e-3 20e-3]);

set(gca,'FontSize',18,'LineWidth',2);
```

```
set(Hinset(1),'LineWidth',2,'Color','k');
set(Hinset(2),'LineWidth',1,'Color','r');
set(Hinset(3),'LineWidth',2,'Color','r');
set(Hinset(4),'LineWidth',1,'Color','b');
set(Hinset(5),'LineWidth',2,'Color','b');

% save each figure. comment it if you use this macro just for visualisation
% use the print(...) function interface
% filename = ['figure_in16_insets_' int2str(i)];
% print('-depsc',filename)

end; %put or remove a comment sign in front of end if the loop on i is done or not

% exporting the final graph
% print -dformat filename

%print -depsc figure_in16_poster.eps
%print -djpeg figure_in16_poster.jpg

% % then use convert command on terminal :
% % convert -density 320x320 insitu_drying_10237-10242.eps insitu_drying_10237-10242.jpg
```

References:

1. Selden, P.A., W.A. Shear, and P.M. Bonamo, *A Spider and Other Arachnids from the Devonian of New-York, and Reinterpretations of Devonian Araneae.* Palaeontology, 1991. **34**: p. 241-281.
2. Coddington, J.A. and H.W. Levi, *Systematics and Evolution of Spiders.* Ann. Rev. Ecol. Syst., 1991. **22**: p. 565.
3. Foelix, R., *Biology of Spiders*. 1996: Oxford University Press.
4. Vollrath, F., *Spider webs and silk.* Sci. Am., 1992. **266**(3): p. 70-76.
5. Vollrath, F. and D.P. Knight, *Liquid crystalline spinning of spider silk.* Nature, 2001. **410**: p. 541-548.
6. Wilson, R.S., *The control of dragline spinning in the garden spider.* The Quarterly Journal of Microscopical Science, 1962. **103**(Oxford): p. 557-571.
7. Gosline, J.M., M.E. Demont, and M.W. Denny, *The Structure and Properties of Spider Silk.* Endeavour, 1986. **10**(1): p. 37-43.
8. Gosline, J.M., et al., *The mechanical design of spider silks: from fibroin sequence to mechanical function.* J. of Exp. Biol., 1999. **202**: p. 3295-3303.
9. Termonia, Y., *Molecular modelling of spider silk elasticity.* Macromolecules, 1994. **27**: p. 7378 - 7381.
10. Tillinghast, E.K., S.F. Chase, and M.A. Townley, *Water extraction by the major ampullate duct during silk formation in the spider, Argiope aurantia Lucas.* Journal of Insect Physiology, 1984. **30**(7): p. 591-596.
11. Riekel, C., et al., *X-Ray Diffraction on Spider Silk during Controlled Extrusion under a Synchrotron Radiation X-Ray Beam.* Biomacromolecules, 2000. **1**: p. 622-626.
12. Work, R.W., *Dimensions, Birefringences and force-elongation behaviour of major and minor ampullate silk fibres from orb web spinning spiders - The effects of wetting on these properties.* Text Res J, 1977. **47**: p. 650-662.
13. Xu, M. and R.V. Lewis, *Structure of a protein superfiber: Spider dragline silk.* Proc. Natl. Acad. Sci., 1990. **87**: p. 7120-7124.
14. Hinman, M.B. and R.V. Lewis, *Isolation of a clone encoding a second dragline silk fibroin.* J. of Biol. Chemistry., 1992. **267**: p. 19320-19324.
15. Hinman, M.B., J.A. Jones, and R.V. Lewis, *Synthetic spider silk: a modular fiber.* TIBTECH, 2000. **18**: p. 374-379.
16. Marsh, R.E., R.B. Corey, and L. Pauling, *The Structure of Tussah Silk Fibroin (with a Note on the Structure of Beta-Poly-L-Alanine).* Acta Crystallographica, 1955. **8**(11): p. 710-715.
17. Arnott, S., S.D. Dover, and A. Elliott, *Structure of beta-poly-L-alanine: refined atomic co-ordinates for an anti-parallel beta-pleated sheet.* Journal of molecular biology, 1967. **30**: p. 201-208.
18. Bram, A., et al., *X-ray diffraction from single fibres of spider silk.* J. Appl. Cryst., 1997. **30**: p. 390-392.
19. Parkhe, A.D., et al., *Structural Studies of Spider Silk Proteins in the Fiber.* Journal of Molecular Recognition, 1997. **10**: p. 1-6.
20. Riekel, C., et al., *Aspects of X-ray diffraction on single spider fibers.* International Journal of Biological Macromolecules, 1999. **24**(2-3): p. 179-186.
21. Riekel, C. and F. Vollrath, *Spider silk fibre extrusion: combined wide- and small-angle X-ray microdiffraction experiments.* Int. J. Biol. Macrom., 2001. **29**(3): p. 203-210.
22. Craig, C.L., *Capture by Design*. 2002: Oxford University Press (in press).
23. Fraser, R.D.B. and T.P. Macrae, *Conformations of Fibrous Proteins*. 1973, New York: Academic Press.

24. Hayashi, C.Y., N.H. Shipley, and R.V. Lewis, *Hypothesis that correlate the sequence, structure, and mechanical properties of spider silk proteins.* Int. J. of Biol. Macrom., 1999. **24**: p. 271-275.
25. Porter, D., F. Vollrath, and Z. Shao, *Predicting the mechanical properties of spider silk as a model nanostructured polymer.* European Physical Journal E, 2005. **16**(2): p. 199-206.
26. Gersappe, D., *Molecular mechanisms of failure in polymer nanocomposites.* Physical Review Letters, 2002. **89**(5).
27. Squires, G.L., *Introduction to the theory of thermal neutron scattering*. 1978: cambridge university press.
28. Bée, M., *La diffusion quasiélastique des neutrons ; introduction et principes généraux*, in *Diffusion quasiélastique des neutrons*, M. Bée, Editor. 2000, EDP SCIENCES. p. 1-14.
29. J. Als-Nielsen, D.M., *Elements of Modern X-Rays Physics*. 2001, New York: John Wiley & Sons Ltd.
30. Schweika, W., *Scattering Experiments*, in *Physics meets biology: from soft matter to cell biology ; lecture notes of the 35th Spring School*, G. Gompper, Editor. 2004, Institute of Solid State Research: Jülich.
31. *Theory, instruments and methods*. NEUTRON AND SYNCHROTRON RADIATION FOR CONDENSED MATTER STUDIES, ed. J.L.H. J. Baruchel, M.S. Lehmann, J. R. Regnard, C. Schlenker. Vol. 1: EDP sciences - Springer-Verlag.
32. Gourrier, A., *Etudes combinées de microdéformation par indentation et de microdiffraction des rayons-X: applications dans le cas de polymères*. 2004, Université Joseph Fourier-Grenoble I: Grenoble.
33. Pynn, R., *Neutron Scattering—A Primer*. 1990, Los Alamos Science. p. 1-31.
34. *The ILL Yellow Book*. 2001.
35. J. Baruchel, J.L.H., M.S. Lehmann, J. R. Regnard, C. Schlenker, *Neutron and synchrotron radiation for condensed matter studies*. Vol. 1,2,3. 1993: EDP sciences - Springer-Verlag.
36. *web page:* http://www.esrf.fr.
37. Bacon, G.E., *Neutron diffraction*, Oxford: Clarendon Press.
38. Work, R.W. and P.D. Emerson, *An apparatus and technique for the forcible silking of spiders.* J Arachnol, 1982. **10**: p. 1-10.
39. Madsen, B. and F. Vollrath, *Mechanics and morphology of silk drawn from anaesthetised spiders.* Naturwissenschaften, 2000. **87**: p. 148-153.
40. Riekel, C., *New avenues in x-ray microbeam experiments.* Reports on Progress in Physics, 2000. **63**(3): p. 233.
41. Fraser, R.D.B., et al., *Digital Processing of Fiber Diffraction Patterns.* Journal of Applied Crystallography, 1976. **9**(APR1): p. 81-94.
42. Shotton, M.W., et al., *New developments in instrumentation for X-ray and neutron fibre diffraction experiments.* Journal of Applied Crystallography, 1998. **31**: p. 758-766.
43. Frick, B. and M. Gonzalez, *Five years operation of the second generation backscattering spectrometer IN16 - a retrospective, recent developments and plans.* Physica B-Condensed Matter, 2001. **301**(1-2): p. 8-19.
44. Marsh, R.E., R.B. Corey, and L. Pauling, *An Investigation of the Structure of Silk Fibroin.* Biochimica Et Biophysica Acta, 1955. **16**(1): p. 1-34.
45. Grubb, D.T. and L.W. Jelinski, *Fiber Morphology of Spider Silk: The Effects of Tensile Deformation.* Macromolecules, 1997. **30**(10): p. 2860-2867.

46. Thiel, B.L. and C. Viney, *Spider major ampullate silk (drag line): smart composite processing based on imperfect crystals.* Journal of Microscopy, 1997. **185**: p. 179 - 187.
47. Craig, C.L., *Spiderwebs and Silk: Tracing Evolution From Molecules to Genes to Phenotypes*. 2003: Oxford University Press.
48. Thiel, B.L., D.D. Kunkel, and C. Viney, *Physical and Chemical Microstructure of Spider Dragline - a Study by Analytical Transmission Electron-Microscopy.* Biopolymers, 1994. **34**(8): p. 1089-1097.
49. Simmons, A.H., C.A. Michal, and L.W. Jelinski, *Molecular Orientation and Two-Component Nature of the Crystalline Fraction of Spider Dragline Silk.* Science, 1996. **271**: p. 84-87.
50. Burghammer, M., M. Müller, and C. Riekel, eds. *X-ray synchrotron radiation microdiffraction on fibrous biopolymers like cellulose and in particular spider silks*. Recent Research Developments in Macromolecules, ed. S.G. Pandalai. Vol. 7. 2003, Research Signpost: Trivandrum, India. 103-125.
51. Valluzzi, R. and H.-J. Jin, *X-ray Evidence for a "Super"-Secondary Structure in Silk Fibers.* Biomacromolecules, 2004. **5**(3): p. 696-703.
52. Riekel, C. and F. Vollrath, *Spider silk fibre extrusion: combined wide- and small-angle X-ray microdiffraction experiments*, in *Int. J. Biol. Macrom.* 2001. p. 203-210.
53. Work, R.W. and N. Morosoff, *A physico-chemical study of the supercontraction of spider major ampullate silk fibers.*, in *Textile research journal*. 1982. p. 349-356.
54. Grubb, D.T. and G. Ji, *Molecular chain orientation in supercontracted and re-extended spider silk*, in *Int. J. Biol. Macrom.* 1999. p. 203-210.
55. Parkhe, A.D., et al., *Structural Studies of Spider Silk Proteins in the Fiber*, in *Journal of Molecular Recognition*. 1997. p. 1-6.
56. Work, R. and N. Morosoff, *A Physico-Chemical Study of the Supercontraction of Spider Major Ampullate Silk Fibers.* Textile Research Journal, 1982: p. 349-356.
57. Yang, Z., D.T. Grubb, and L.W. Jelinski, *Small-Angle X-ray Scattering of Spider Dragline Silk.* Macromolecules, 1997. **30**: p. 8254 - 8261.
58. Riekel, C., et al., *Influence of CO2 on the micro-structural properties of spider dragline silk: X-ray microdiffraction results.* Naturwissenschaften, 2004. **91**(1): p. 30-33.
59. Vainshtein, B.K., *Diffraction of X-rays by Chain Molecules*. 1966, Amsterdam: Elsevier.
60. Jacrot, B., Reports on Progress in Physics, 1976. **39**: p. 911-953.
61. Müller, M., et al., *Direct observation of microfibril arrangement in a single native cellulose fiber by microbeam small-angle X-ray scattering.* Macromolecules, 1998. **31**(12): p. 3953-3957.
62. Klug, H.P. and L.E. Alexander, *X-ray Diffraction Procedures for Polycrystalline and Amorphous Materials*. 2nd ed. 1974, New York: Wiley-Interscience.
63. Mitra, S., et al., *Dynamics of water in confined space (porous alumina): QENS study.* Journal of Physics-Condensed Matter, 2001. **13**(37): p. 8455-8465.
64. Czihak, C., et al., *Ice formation in amorphous cellulose.* Physica B, 2000. **276**: p. 286-287.
65. Liu, Y., et al., *Inelastic X-ray scattering studies of phonons in liquid crystalline DNA.* Physical Chemistry Chemical Physics, 2004. **6**(7): p. 1499-1505.
66. Sapede, D., et al., *Nanofibrillar structure and molecular mobility in spider dragline silk.* Macromolecules, 2005. **38**(20): p. 8447-8453.
67. Beek, J.v., et al., *The molecular structure of spider dragline silk: Folding and orientation of the protein backbone.* Proceedings of the National Academy of Sciences, 2002. **99**(16): p. 10266-10271.

68. Papanek, P., J.E. Fischer, and N.S. Murthy, *Molecular vibrations in nylon 6 studied by inelastic neutron scattering.* Macromolecules, 1996. **29**(6): p. 2253-2259.
69. Czihak, C., et al., *Relaxational motion and ice formation of water adsorbed to cellulose.* Journal De Physique Iv, 2000. **10**(P7): p. 199-202.
70. Müller, M., et al., *All disordered regions of native cellulose show common low-frequency dynamics.* Macromolecules, 2000. **33**(5): p. 1834-1840.

Contributions to the understanding of the hierarchical structure and dynamics of spider dragline silk

Abstract:
Spider dragline silk is a remarkable material, a biopolymer with outstanding mechanical properties. Spider silk has been in the focus of intense research using a wide variety of experimental techniques and in addition theoretical modelling. However, its macroscopic properties are still not well linked to its microscopic structure and dynamics. Synchrotron radiation small- and wide-angle scattering experiments have in recent years particularly contributed to the development of microscopic structural models.
In this thesis work, neutron scattering techniques have been used for the first time for the study of spider silk. The high scattering contribution of hydrogen and the scattering length difference of hydrogen and deuterium have allowed a fresh look at structural and dynamical properties of spider silks. Thus the results support a hierarchical, three-phase model of nanofibrils composed of crystalline and short-range order domains embedded in an amorphous matrix. Complementary synchrotron scattering experiments suggest that water absorbed by the amorphous matrix forms an amorphous ice at low temperatures. Wide-angle neutron scattering (WANS) experiments showed a meridional superlattice peak -not observed by X-ray (WAXS) experiments-, which is assigned to a smectic beta-sheet structure in the short-range order domains. The exchange of H_2O against D_2O in small-angle neutron scattering (SANS) experiments allowed changing the neutron scattering length density contrast in the nanofibrils and the contrast of the nanofibrils against the amorphous matrix. The molecular mobility was probed by inelastic and quasielastic neutron scattering techniques. A hierarchy of relaxation processes seems to describe hydrated silk, while native silk behaves like a glass at room temperature.

Résumé :
Le fil de traîne de l'araignée est un matériau remarquable, un biopolymère aux exceptionnelles propriétés mécaniques. La soie d'araignée a été au centre d'une intense recherche utilisant une large gamme de techniques expérimentales et de modélisations théoriques. Néanmoins, ses propriétés macroscopiques n'ont pas encore été correctement reliées à sa structure et sa dynamique microscopiques.
Dans ce travail de thèse, les techniques de diffusion neutronique ont été pour la première fois utilisées pour l'étude de la soie d'araignée. La forte contribution de l'hydrogène en diffusion des neutrons ainsi que la différence des longueurs de diffusion de l'hydrogène et du deutérium ont permis de porter un regard nouveau sur les propriétés structurales et dynamiques des soies d'araignée. Ainsi les résultats appuient un modèle hiérarchique à trois phases de nanofibrilles composées de domaines cristallins et d'ordre à courte portée, contenues dans une matrice amorphe. Des expériences complémentaires de diffusion du rayonnement synchrotron suggèrent que l'eau absorbée par la matrice amorphe forme une glace amorphe à basses températures. Des expériences de diffraction de neutrons (abréviation anglaise : WANS) ont montré un pic méridional hors réseau -non observé par les expériences en rayons X (abréviation anglaise : WAXS)- attribué à une structure smectique de feuillets beta dans les domaines d'ordre à courte portée. L'échange de H_2O contre D_2O pour les expériences de diffusion de neutrons aux petits angles (abréviation anglaise : SANS) a permis d'observer la variation de contraste à l'intérieur des nanofibrilles et entre les nanofibrilles et la matrice. La mobilité moléculaire a été sondée par des techniques de diffusion inélastique et quasiélastique des neutrons. Il semble qu'une hiérarchie de phénomènes de relaxations décrive la soie hydratée, tandis que la soie native a un comportement vitreux à température ambiante.